Investigation of Active Site Structure and Formation on Boron-Based Oxidative Dehydrogenation Catalysts

By

Melissa C. Cendejas

A dissertation submitted in partial fulfillment of

the requirements for the degree of

Doctor of Philosophy

(Chemistry)

at the

UNIVERSITY OF WISCONSIN-MADISON

2021

Date of final oral examination: 8/13/2021

This dissertation is approved by the following members of the Final Oral Committee:
Ive Hermans, Chemistry
John Berry, Chemsitry
Kyoung-Shin Choi, Chemistry
Aaron J. Rossini, Chemistry (Iowa State University)

Contents

Dedications

Completing a PhD is a long and challenging journey that cannot be undertaken alone. I am forever grateful to all who have assisted me. Words fail to convey the full force of my emotions, but I must attempt anyway.

To the Hermans group – I couldn't have asked for a better bunch of people to do science with. Alyssa and Sarah, you were amazing mentors and a huge reason I joined the group. Will and Theo, I have loved working closely with you and appreciate our conversations. Lesli, I am so grateful for your presence and excited to continue to work with you. Shao-Chun, in the lab or on the softball field, you are dependable and insightful, and I am happy we've been on this journey together. To the rest of the group, I am thankful that we get to do science together and am excited to see everyone continue to grow. Ive, thank you for everything. You have helped me become a strong critical thinker and researcher and have shown me how to advocate for myself and my ideas.

To my collaborators – my science would be much weaker and my experience much poorer without you. Aaron and Rick, I simply cannot fully express how much I value you. Thank you for introducing me to solid state NMR; it has been a genuine joy to work with you. Simon, Adam, and Dimosthenis, I truly did not know I could learn so much in such a short time. The love you all have for science is infectious and it has been a privilege to do science with you all.

To the Chemistry department staff who have enabled my research, I cannot overstate your importance. Cathy, you empowered me to grow and test my NMR knowledge. I've loved learning from you and wouldn't want to spend hours trying to get an experiment to work with anyone else. Tracy, taking your glassblowing class was one of the best things I did in grad school. Aside from the beautiful work that you do, you are one of my favorite people to talk to. Thank you for always taking the time to chat. Kristi, Sue, Arrietta, and Jeff, I would not be here without the work you do keep everything running.

To my volleyball team – I have loved spending Tuesday evenings with you for the past three years. You have helped keep me sane and I cherish our growing friendship.

To Coach Herman and Williams College Softball – you taught me so much about how to live life. Coach, I am deeply grateful for all the work I did with you and the tools I have at my disposal because of the softball program. T and Ric, I love you and value our friendship. I can't wait to drink some more beers with you.

To Kelsey, Reid, Jake, Jorge, and Peter, your friendship means the world to me. I love you and look forward to our next reunion.

To my Chemistry friends – this has been such a special time. Wow. I have grown so much because of you. Thank you for forcing me to get a bike and for supplying endless laughs and wonderful conversations. Matt and Andj, you two have been my rocks and I can't imagine my life without you. See you all on our friend compound in a few years.

To my extended family – the warmth I feel from your love and support could heat my apartment throughout a Wisconsin winter. Thank you for asking about my research and not immediately dozing off when I start using scientific jargon.

To my heavenly mother, my guardian angel, who has been watching over me and guiding me from afar my entire life. I love you.

To my immediate family – you were my first and best teachers. Your constant support and love form the strong root system that allows me to grow and expand. I love you with all my being. To my Mom – my loudest and fiercest cheerleader (I hear cowbells and you yelling "Baby giiiiirl!" in my head whenever I need a little push) – who taught my sisters and me to be strong and independent women. To my Dad – my first coach and the voice in my head cautioning me and reminding me to always be prepared. To my oldest sister, Danielle – you were my first role model. You showed me how to be brave, follow my dreams, and trust my voice. To my brother, Phillip, who was the first to push me to be better and who helped me develop my sense of humor. You have also given us Brooke and Ryan, who are perfect bundles of light and love. To my sister Nicole, who constantly inspires me with her creativity, love, and dedication. Your students are incredibly lucky to have you. To my sister Deanna, who has been one of the biggest influences in my life. You have shown me how to live truthfully and I am so proud of you. And finally, to our single bathroom, which taught me many lessons about conflict resolution and the virtues of having a strong bladder.

CHAPTER 1

What You Need to Know Before Reading This Thesis (Introduction)

Chapter 1: What You Need to Know Before Reading This Thesis (Introduction)

As stated in the title, the work presented here investigates the active site on boron-based catalysts for the oxidative dehydrogenation (ODH) of propane, which may seem like a mess of words, as do the titles of most scientific papers. The purpose of this chapter is to orient you, the reader, to the larger context of my work, to introduce you to the vocabulary, and briefly touch on concepts needed to understand the titles of the subsequent chapters. This is by no means an exhaustive review but is meant to serve more as a field guide.

1.1 Heterogeneous Catalysis

A catalyst is a material that lowers the energy needed for a chemical reaction to occur, often by allowing a new reaction pathway (Figure 1.1). Catalysts of all forms enable life on this planet, from biological catalysts, or enzymes, which are responsible for the reactions that support plant and animal life, to industrial catalysts, which transform fossil fuels to the fuels and materials that enable modern society. The majority of industrial catalysts are heterogeneous – meaning the catalyst is in a different physical phase than the reactants. Typically, the catalyst is a solid and the reactants are gas or liquid. This work focuses on heterogeneous catalysts that can transform propane into propylene, an industrially important chemical transformation.

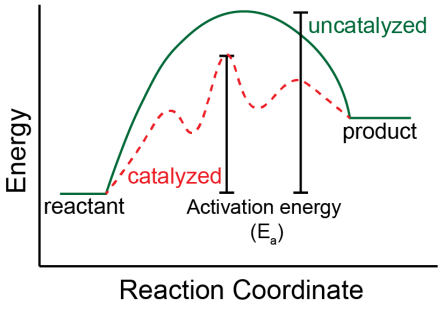

Figure 1.1 Diagram showing the energy of a reaction along the reaction coordinate of an uncatalyzed (green) and catalyzed (green) reaction. The black lines denote the active energies for each pathway.

1.2 On-Purpose Propylene Production

Light olefins – ethylene (C_2H_4) and propylene (C_3H_6) – are chemical building blocks that have enabled our modern world. These olefins are turned into a wide variety of molecules that find use in household cleaners, cosmetics, and pharmaceuticals. The largest use of ethylene and propylene is their polymerization into polyethylene and polypropylene, two of the most abundant

plastics. The global production capacity in 2017 was 170 million tonnes (Mt) and 130 Mt annually for ethylene and propylene, respectively.[1-2] The demand for these light olefins – particularly propylene – is projected to continue to rise. Ethylene and propylene are traditionally produced via the steam cracking of the naphtha fraction of crude oil.[3] Recently, there has been a shift to natural gas liquids as the feed for cracking, the main product of which is ethylene, with sparing amounts of propylene and higher olefins. The decreased propylene production from traditional sources (Figure 1.2) and rising demand has highlighted the need for on-purpose propylene production technologies to fill this supply and demand gap.[4]

Direct propane dehydrogenation (PDH, orange label in Figure 1.2) is one such method

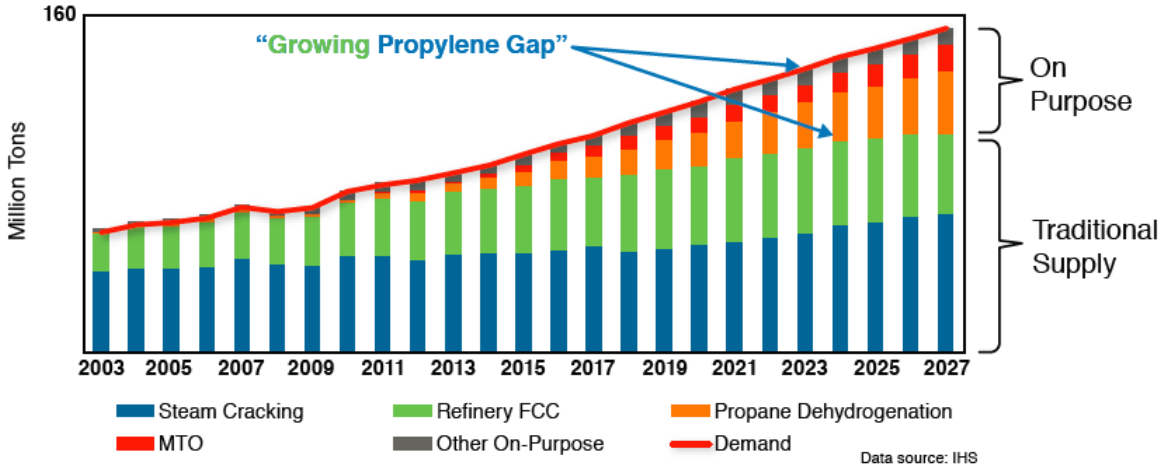

Figure 1.2 The global production capacity of propylene form current and projected sources (bar graph) and the projected propylene demand (red line, ref. 4).

that converts propane to propylene and H2 (Reaction 1.1) with high selectivity (90% propylene selectivity at 30% conversion).

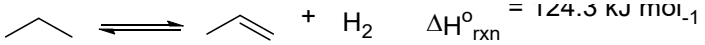

(Reaction 1.1)

However, ODH is equilibrium-limited and endothermic, requiring sub-ambient pressures (<1 bar) and high reaction temperatures (500-650 ºC) to deliver high conversions.[5] The reaction conditions lead to rapid catalyst deactivation by carbon deposition (coke), requiring complex regeneration

schemes to regain activity. PDH has been industrially implemented and is practiced as the Catofin process (Lummus), which employs a supported chromium catalyst (Cr/Al_2O_3) catalyst, and the Oleflex process (UOP), which employs a supported platinum catalyst (Pt/Al_2O_3).[5]

1.2.1 Oxidative Dehydrogenation (ODH)

Oxidative dehydrogenation (ODH, Reaction 1.2) of propane has been explored on a lab scaled as a lower-energy alternative propylene production method. ODH has the advantages of being non-equilibrium limited and exothermic, thus requiring lower operating temperatures (<550 C).

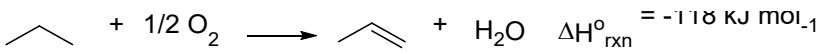

(Reaction 2.1)

Additionally, the presence of oxygen in the gas feed prevents the formation of coke, lengthening the catalyst lifetime and preventing expensive regeneration schemes. However, the main hurdle preventing the implementation of ODH technology is the low product selectivity caused by the facile over-oxidation of alkenes to CO and CO_2 (CO_x). Despite propane ODH being an active research field for 5 decades, there has yet to be a catalyst selective and productive enough for industrial application (catalyst productivity is a measurement of the amount of product generate per mass of catalyst per unit time).

For decades, the state-of-the-art ODH catalysts have been supported vanadium oxides.[6-7] The mechanism and active site structure have therefore been thoroughly characterized.[8] The Mars-van Krevelen (MvK) mechanism is typically used to describe the kinetics of ODH catalyzed by vanadium oxides, in which the reoxidation of the active metal center is done through lattice oxygen rather than molecular O_2. The MvK mechanism is characterized by a first-order dependence with respect to alkane concentration and a zero-order dependence with respect to O_2 concentration.

1.3. Catalyst Synthesis

It is important to note that heterogeneous catalysis occurs at the surface of a material, where reactant molecules can interact with active sites. Catalyst active sites come in many forms and shapes and in many cases, the catalytic performance of one form varies from a different form of the same material. We therefore have a great interest in understanding and controlling active site structure.

Knowledge of how synthesis parameters affect speciation and activity helps improve synthesis to make better catalysts. In this thesis, I will focus on supported catalyst materials, where the active phase is only on the surface. A typical supported catalyst consists of a metal oxide, a metal nanoparticle, or single atom supported on a metal oxide support such as silica (SiO_2), alumina (Al_2O_3), or titanium oxide (TiO_2).

There are different ways to get an active material onto a support. Two methods presented in this work are incipient wetness impregnation (IWI) and grafting. For both, an appropriate precursor molecule or compound and solvent (if needed) must be chosen. In IWI, the precursor is dissolved in an appropriate solvent to create a solution with the desired weight loading of the active material. The solution is then added to the support dropwise and with through mixing. The volume of the synthesis solution is enough to just wet the surface but not enough to make a slurry. The sample is then thermally treated to remove any organics and generate the catalyst material. Typically, the final weight loading is determined by the amount of precursor in the synthesis solution.

Compared to IWI, grafting is a more controlled synthesis method. In a typical grafting experiment, the support material is thermally pretreated to control the amount of hydroxyl groups that serve as anchoring sites for the precursor.[9] Under inert conditions, the precursor molecule is transferred – either in solution with a non-coordinating solvent or neat in the gas phase – onto the support where it reacts with hydroxyls to anchor to the surface. After a reaction period, there is a post-treatment step where unreacted precursor is removed. This post-treatment step limits the

number of active species to whatever reacted with the surface. As a result, grafting synthesis typically results in isolated single sites.

1.4. Spectroscopy

Spectroscopy is the study of how light interacts with matter. We (chemists, engineers) use spectroscopy to generate molecular and atomistic pictures of materials. When a photon hits a sample, energy is absorbed, inducing an energetic transition, the exact identity of which depends on the energy of the incident photon. A material's response to the photon is recorded and used to construct a spectrum. The two main spectroscopies discussed in this thesis are magic angle spinning nuclear magnetic resonance (MAS SSNMR) and X-ray spectroscopy.

1.4.1 Solid State Nuclear Magnetic Resonance Spectroscopy (SSNMR)

NMR spectroscopy involves the use of microwaves to induce changes to the spin state of a nucleus of a specific element. NMR on liquids is most commonly practice; however, our focus here will be on solid state NMR. In an NMR experiment, a sample is exposed to an external magnetic field (B_0), causing the nuclear spins (quantum number *I*) in a sample to align, and

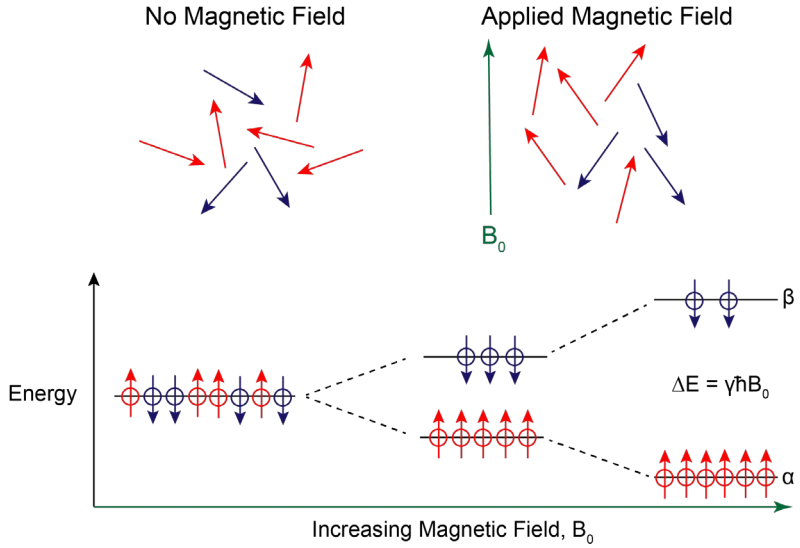

Figure 1.3 Simplified illustration of the alignment of spins and splitting of spin state when exposed to an external magnetic field.

causing a splitting in the energy levels of the spin states. The population difference between the two states gives rise to the NMR signal. The chemical shift is sensitive to the electron density surrounding the nucleus of interest. When there is a non-spherical electron distribution around the nucleus, the chemical shift is dependent on the orientation of the molecule with respect to the external field, leading to chemical shift anisotropy. Over the time scale of an NMR measurement of liquids, molecular tumbling averages out any chemical shift anisotropy that is present in the sample. In solid samples, this averaging is not possible, leading to severely broadened signals. To narrow, SSNMR spectra and overcome chemical shift anisotropy, solid sample are spun at high frequencies about the "magic angle" (θ = 54.7° relative to B_0), giving rise to magic angle spinning (MAS) SSNMR. When a sample is spun quickly at the magic angle, the three major components of the anisotropic interaction are averaged (Figure 1.4).

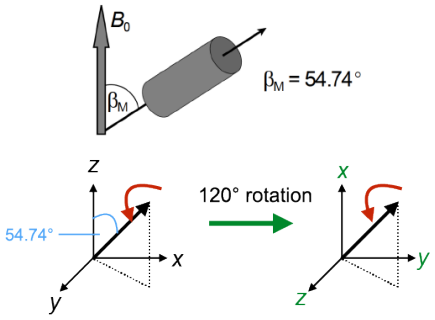

Figure 1.4 Illustration of the magic angle and the averaging that happens during spinning.

The main nucleus of focus in this thesis is boron-11 (^{11}B). Boron-11 is a spin I = 3/2 half-integer quadrupolar nucleus. The asymmetric charge distribution in a quadrupolar nucleus leads to strong coupling interactions with the surrounding electric field gradient (EFG). ^{11}B electric field gradient (EFG) tensors, quadrupolar coupling constant (C_Q) and asymmetry parameter (η), and isotropic chemical shifts (δ_{iso}) provide information about the local chemical environment (bonded atoms and symmetry) surrounding the boron nucleus.[10] C_Q is sensitive to the symmetry and the nucleus, with trigonal planar boron species giving rise to C_Q values between 2.5 and 3 MHz.

In the studies described in this thesis, we employ a standard suite of MAS SSNMR experiments. The names of the experiments and interactions probed are given in Table 1.1

Table 1.1. SSNMR experiments and the interactions or species probed.

Experiment	Species or Interaction
Direct excitation or spin echo	All species in a sample
^{11}B-^{1}H dipolar refocused insensitive nuclei enhanced polarization transfer (D-RINEPT)	^{11}B species proximate to ^{1}H species (long and short range)
^{11}B{^{1}H dephased}	^{11}B species distant from ^{1}H species
^{11}B double quantum-single quantum homonuclear correlation	^{11}B – ^{11}B connectivity
^{1}H double quantum-single quantum homonuclear correlation	^{1}H – ^{1}H connectivity (long and short range)
Multiple quantum magic angle spinning (MQMAS)	Resolution of quadrupolar spectra

1.4.2 X-Ray Spectroscopy

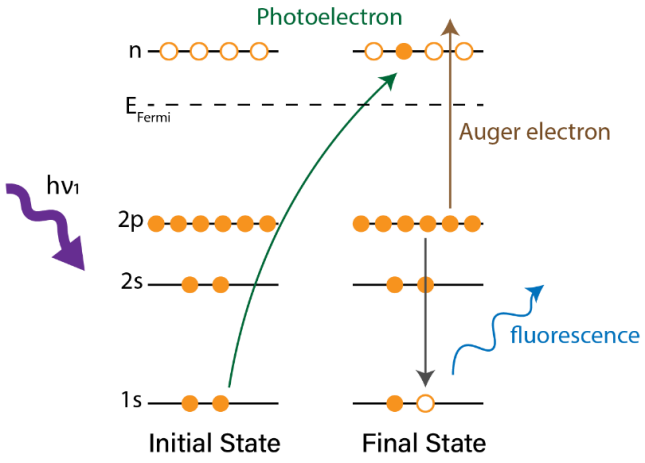

Figure 1.5 Diagram showing the interaction between an incident X-ray and a core electron (left) and the different relaxation pathways that can be observed.

X-ray spectroscopy involves the use of x-rays to excite element-specific electronic transitions (Figure 1.5). The exact type of x-ray spectroscopy performed depends mostly on what is being detected. X-rays can eject photoelectrons from a material (green arrow in Figure 1.5). The energy of the photoelectron is detected in X-ray photoelectron spectroscopy (XPS). XPS can be used to identify components of a material, to determine chemical state, and to determine the relative composition of a material.

X-ray absorption spectroscopy (XAS), as the name suggests, measure the absorption of an x-ray of a specific energy range. XAS can be measured in either transmission or fluorescence yield. When light elements are analyzed, soft X-rays (<1 keV) and vacuum environments are needed. Soft XAS can be measured in fluorescence or total electron yield (TEY) mode. XAS gives information about the oxidation state, geometry, and coordination environment of the element of interest.

1.5 References

(1) LyondellBasell, 2017 Data Book. **2017**

(2) Rightor, E. G.; Tway, C. L., Global energy & emissions reduction potential of chemical process improvements. *Catalysis Today* **2015,** *258* (Part 2), 226-229. https://doi.org/10.1016/j.cattod.2015.02.023.

(3) Ren, T.; Patel, M.; Blok, K., Olefins from conventional and heavy feedstocks: Energy use in steam cracking and alternative processes. *Energy* **2006,** *31* (4), 425-451. https://doi.org/10.1016/j.energy.2005.04.001.

(4) HoneywellUOP, Filling the Propylene Gap – Shaping the Future with On-Purpose Technologies. **2019**.

(5) Sattler, J. J. H. B.; Ruiz-Martinez, J.; Santillan-Jimenez, E.; Weckhuysen, B. M., Catalytic Dehydrogenation of Light Alkanes on Metals and Metal Oxides. *Chemical Reviews* **2014,** *114* (20), 10613-10653. 10.1021/cr5002436.

(6) Grant, J. T.; Carrero, C. A.; Goeltl, F.; Venegas, J.; Mueller, P.; Burt, S. P.; Specht, S. E.; McDermott, W. P.; Chieregato, A.; Hermans, I., Selective Oxidative Dehydrogenation of Propane to Propene using Boron Nitride Catalysts. *Science* **2016,** *354* (6319), 1570-1573. 10.1126/science.aaf7885.

(7) Grant, J. T.; Love, A. M.; Carrero, C. A.; Huang, F.; Panger, J.; Verel, R.; Hermans, I., Improved Supported Metal Oxides for the Oxidative Dehydrogenation of Propane. *Topics in Catalysis* **2016,** *59* (17), 1545-1553. 10.1007/s11244-016-0671-2.

(8) Carrero, C. A.; Schloegl, R.; Wachs, I. E.; Schomaecker, R., Critical Literature Review of the Kinetics for the Oxidative Dehydrogenation of Propane over Well-Defined Supported Vanadium Oxide Catalysts. *ACS Catalysis* **2014,** *4* (10), 3357-3380. 10.1021/cs5003417.

(9) Copéret, C.; Comas-Vives, A.; Conley, M. P.; Estes, D. P.; Fedorov, A.; Mougel, V.; Nagae, H.; Núñez-Zarur, F.; Zhizhko, P. A., Surface Organometallic and Coordination Chemistry toward Single-Site Heterogeneous Catalysts: Strategies, Methods, Structures, and Activities. *Chemical Reviews* **2016,** *116* (2), 323-421. 10.1021/acs.chemrev.5b00373.

(10) Kentgens, A. P. M., A practical guide to solid-state NMR of half-integer quadrupolar nuclei with some applications to disordered systems. *Geoderma* **1997,** *80* (3), 271-306. https://doi.org/10.1016/S0016-7061(97)00056-6.

CHAPTER 2

Boron-Catalyzed Oxidative Dehydrogenation of Propane

This chapter is adapted in part from the following publications:

Love, A. M.; **Cendejas, M. C.;** Thomas, B.; McDermott, W. P.; Uchupalanun, P.; Kruszynski, C.; Burt, S. P.; Agbi, T.; Rossini, A. J.; Hermans, I., Synthesis and Characterization of Silica-Supported Boron Oxide Catalysts for the Oxidative Dehydrogenation of Propane. *The Journal of Physical Chemistry C* **2019,** *123* (44), 27000-27011.

Altvater, N. R.; Dorn, R. W.; **Cendejas, M. C.;** McDermott, W. P.; Thomas, B.; Rossini, A. J.; Hermans, I., B-Mww Zeolite: The Case against Single-Site Catalysis. *Angewandte Chemie International Edition* **2020,** *59* (16), 6546-6550.

Dorn, R. W.; **Cendejas, M. C.;** Chen, K.; Hung, I.; Altvater, N. R.; McDermott, W. P.; Gan, Z.; Hermans, I.; Rossini, A. J., Structure Determination of Boron-Based Oxidative Dehydrogenation Heterogeneous Catalysts with Ultrahigh Field 35.2 T 11B Solid-State NMR Spectroscopy. *ACS Catalysis* **2020,** *10* (23), 13852-13866.

Chapter 2: Boron-Catalyzed Oxidative Dehydrogenation of Propane

In 2016, our group published the discovery that hexagonal boron nitride (hBN) is an active and selective catalyst for the oxidative dehydrogenation (ODH) of propane to propylene, showing higher selectivity than the previous state-of-the-art vanadium catalyst (85 % selectivity for hBN vs. 75% selectivity for V/SiO_2 at 5% conversion, Figure 2.1).[1] Additionally, the main side-product in the ODH of propane is ethylene, another important olefin, rather than the CO and CO_2 that is seen with vanadium catalysts. This finding was surprising both because of the high product selectivity and because hBN is typically a very stable material that is highly resistant to oxidation.

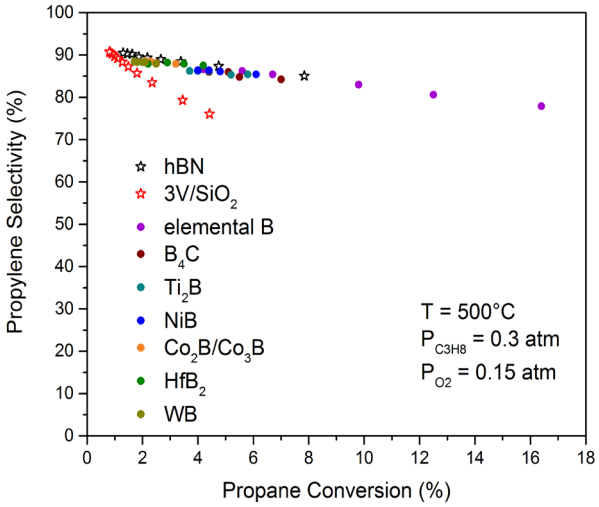

Figure 2.1. Propylene selectivity as function of propane conversion for different bulk boron materials. V/SiO_2 is shown for comparison.

Soon after the initial report, we found that a variety of boron-based materials are just as selective as hBN, as is seen in the conversion versus selectivity plot in Figure 2.1.[2] The similar selectivity trends indicated that the catalysts share an active site. X-ray Photoelectron spectroscopy (XPS) measurements of each boron material before and after catalysis show a shift in the B 1s region to higher binding energies, indicating that surface boron species were oxidized. The XPS results suggest that the oxidized boron is important to the reaction.

Many studies investigating the mechanism and catalyst surface on boron-based materials have been published since 2016. As such, our understanding of this catalytic system is quickly evolving. Our current knowledge base of the active catalytic surface and mechanism is detailed below.

2.1. Understanding the Catalytic Surface

As mentioned above, XPS measurements show that used catalysts contain oxidized boron. To gain a molecular-level understanding of this oxide on hBN, we collaborated with the Rossini group at Iowa State University to use magic angle spinning solid state nuclear magnetic resonance (MAS SSNMR) spectroscopy to investigate the boron structure.[3]

One dimensional ^{11}B spin echo spectra of hBN before (fresh) and after (spent) catalysis are shown in Figure 2.2. The experimental spectra (solid black lines) are analytically simulated (dashed lines) to deconvolute overlapping signals and to determine the isotropic shift (δ_{iso}) and quadrupolar coupling parameters (C_Q and η_Q). More details on ^{11}B MAS SSNMR are given in Chapter 1. The spectrum for the fresh sample is dominated by a signal at δ_{iso} = 30.4 ppm with a C_Q of 2.9 MHz, typical for trigonal boron with three coordinating nitrogen atoms (BN_3). There is a small contribution from a peak with δ_{iso} = 20 ppm, corresponding to BO_3-type species. In the spent samples, there is a large increase in the BO_3 signal. BN_3 species have a much longer longitudinal relaxation time constant (T_1) than the BO_3 species. The inset in Figure 2.2b shows that when short recycle delays are used in the spin echo, only BO_3 species are observed and long recycle delays are needed to obtain a quantitative spin echo spectrum.

To deconvolute the broad oxide feature, we used Multiple Quantum Magic Angle Spinning (MQMAS) NMR. This multidimensional experiment results in a 2D spectrum where the horizontal

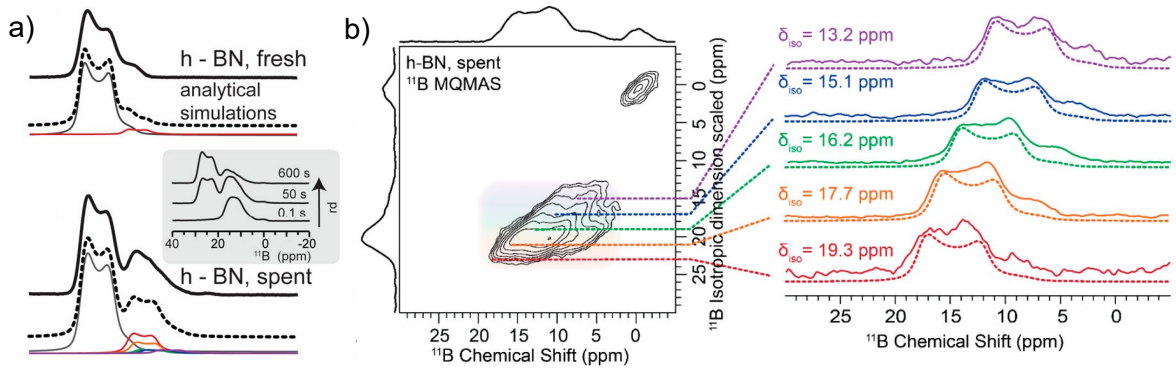

Figure 2.2. ^{11}B spin echo spectra for a) fresh h-BN and spent h-BN and b) ^{11}B MQMAS spectrum and projections for spent h-BN (ref. 3).

axis shows a typical quadrupolar spectrum while the vertical axis shows a high-resolution isotropic ^{11}B dimension free from quadrupolar broadening. Horizontal projections along the vertical axis show a large distribution of peaks with isotropic shifts from 20 to 11 ppm with a C_Q of 2.7 MHz. These results indicate that the boron oxide phase is comprised of a distribution of boron species with varying degrees of hydroxylation. This amorphous phase has the formula $B_2(OH)_{2x}O_{3-x}$ ($x \leq 3$).

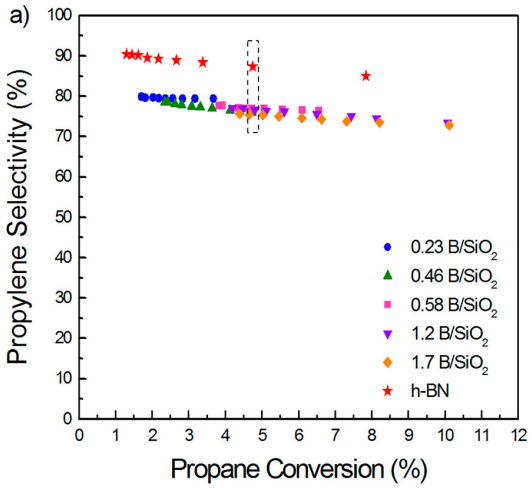

Figure 2.3. Propylene selectivity as a function of propane conversion for B/SiO_2 materials. hBN is shown for comparison (ref. 4).

To verify the catalytic activity of the oxidized boron phase, we immobilized boron oxide on amorphous silica (B/SiO_2).[4] We generated a series of B/SiO_2 materials with different boron weight loadings (0.25 – 1.7 wt.% B) using incipient wetness impregnation (IWI) of triisopropyl borate ($B(O^iPr)_3$ in isopropanol (^{i}PrOH). Catalytic testing under propane ODH conditions (500 °C, 6:3:11 C_3H_8:O_2:N_2) shows that the B/SiO_2 materials are indeed active and selective for propylene (Figure 2.3). Compared to hBN, B/SiO_2 is ca. 10% less selective. This loss of selectivity is attributed to the SiO_2 support, as the presence of SiO_2 in a physical mixture with hBN also results in decreased selectivity.

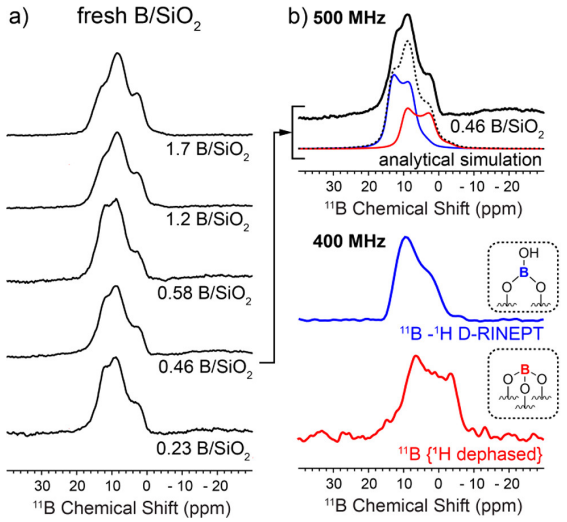

Figure 2.4. a)^{11}B spin echo spectra for all B/SiO_2 materials before reaction and b) deconvolution of an individual spin echo spectrum using the ^{11}B-^1H correlation experiments shown in blue and red (ref. 4).

SSNMR shows that similar boron species are formed on all B/SiO_2 samples, as

all samples exhibit a similar lineshape in the spin echo spectra (Figure 2.4a). ^{11}B-^{1}H correlation experiments show that there are two general types of boron species – hydroxylated and non-hydroxylated. The signal from the ^{11}B-^{1}H dipolar refocused insensitive nuclei enhanced polarization tranfser (D-RINEPT) experiment (blue trace in Figure 2.4b), which shows ^{11}B species proximate to ^{1}H species, and appears at the higher δ_{iso} side of the spin echo. Conversely, the signal from the ^{11}B{^{1}H dephased} spectrum (red trace in Figure 2.4b) appears at the low isotropic shift side of the spin echo and shows ^{11}B species that are not proximate to ^{1}H. Elemental analysis after reaction showed a loss of boron content, with a larger percent loss occurring on the higher loading samples. We note that the reaction temperature (500 °C) is above the melting points of boron oxide compounds (*e.g.,* m.p. of B_2O_3 is 450 °C). ^{11}B homonuclear correlation spectra show an increase in signal compared to the fresh material, indicating that the boron restructured during the reaction to form larger agglomerates.

Our goal with this series of materials was to generate varying degrees of boron agglomeration – from isolated to polymeric to nanoparticulate – as is done with supported metal oxides.[5-6] Instead, we found that similar boron species were formed on all samples and that all samples showed similar catalytic activity regardless of initial boron loading. However, these materials do exhibit induction periods that are dependent on initial weight loading. The observed boron loss likely occurs during the induction period as unstable boron species are leached from the surface to reveal the stable active phase.

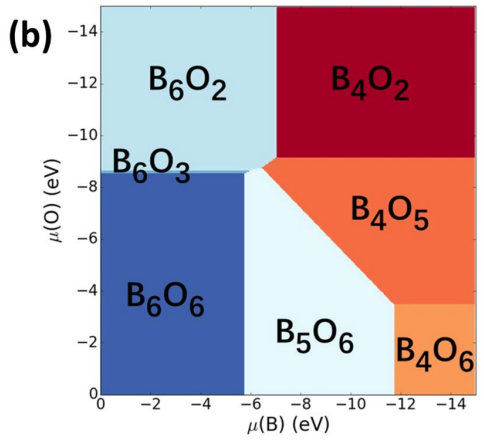

Figure 2.5. Phase diagram of boron oxide base of the ensemble-based averaging of all thermally accessible minima calculated at 793 K (from ref. 7).

This apparent dynamic behavior is in line with the predicted phase diagram for oxidized boron at elevated temperatures in an oxidizing atmosphere

(Figure 2.5).[7] The phase diagram was calculated based on the ensemble averaging of all thermally accessible local minima. The results show that under ODH reaction conditions, many different stoichiometries of B and O – and many different structures within a given stoichiometry – can easily be sampled by the surface. This means that the surface is highly dynamic under reaction conditions and that the thermally relaxed surface observed with *ex situ* characterization methods is likely distinct from the working catalyst surface. We are therefore unable to capture the true active site using *ex situ* methods; however, we can couple catalyst synthesis with *ex situ* analysis before and after catalysis to learn about what needs to be present on the surface for activity.

To this end, we hydrothermally synthesized an MWW zeolite with boron substituted into the framework (B-MWW).[8] The 1D ^{11}B MAS SSNMR spectrum for B-MWW (Figure 2.6) can be simulated using three peaks at $\delta_{iso}(^{11}B)$ = 11 ppm (red fit), $\delta_{iso}(^{11}B)$ = 12 ppm (green fit), and $\delta_{iso}(^{11}B)$ = 15 ppm (blue fit). Based on $\delta_{iso}(^{11}B)$, the red and green peaks correspond to boron species fully substituted into the zeolite framework as $B(OSi)_3$. These isolated $B(OSi)_3$ species make up *ca.* 90% of the integrated intensity. The signal at $\delta_{iso}(^{11}B)$ = 15 ppm (blue fit) accounts for the remaining 10% of the signal intensity and corresponds to a hydroxylated framework boron with two bonds to framework silica and a terminal hydroxide, $B(OSi)_2(OH)$.

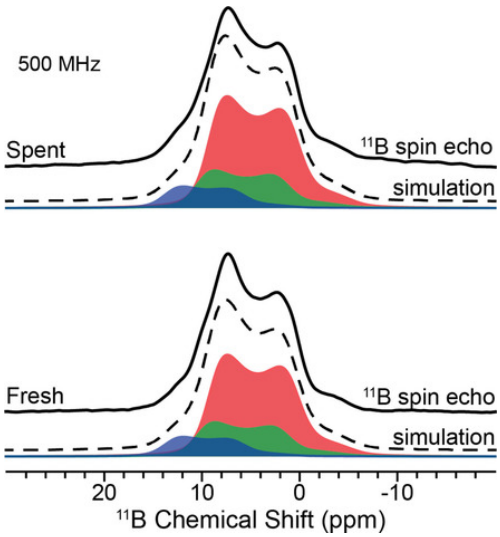

Figure 2.6. 1D ^{11}B MAS SSNMR sepctra of fresh (lower) and spent (upper) B-MWW. The solid lines correspond to the experimental spectra and the dashed lines correspond to the analytical simulations (ref. 8).

^{11}B-^{1}H correlation experiments were used to better understand the boron speciation. 2D ^{11}B→^{1}H D-RINEPT spectra recorded with short (0.64 ms, blue) and long (2.56 ms, red) recoupling times (Figure 2.7). At the short recoupling time, the only correlation observed is between the ^{11}B

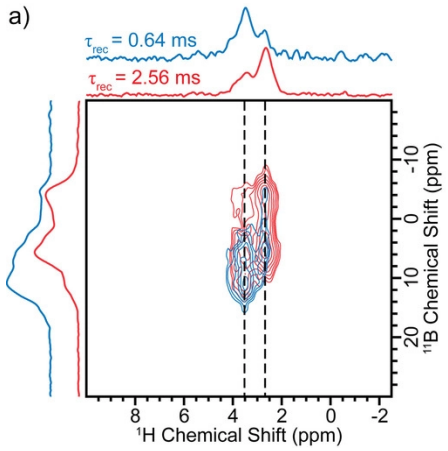

Figure 2.7 2D $^{11}B \rightarrow {}^{1}H$ D-RINEPT spectra of B-MWW acquire with 0.64 ms (blue) and 2.54 ms (red) of total heteronuclear dipolar recoupling (ref. 8).

signal at δ_{iso} = 15 ppm and the ^{1}H signal at 3.5 ppm. When the longer recoupling time is used, an additional correlation signal is observed between the boron species at lower δ_{iso} and the proton signal at 2.7 ppm. Internuclear distances can be estimated by recording dipolar recoupling buildup curves. Based on this analysis, the two different ^{11}B-^{1}H interactions are estimated to have distances of 2 Å and 3 Å. The proposed structure for these interactions in B-MWW are illustrated in Figure 2.8. The 2 Å interaction is associated with a boron hydroxyl group, while the 3 Å interaction corresponds to a hydrogen-bonding interaction with a nearby silanol defect. This material showed no activity for propane ODH, indicating that an isolated BO_3 unit is not catalytically active, and that boron agglomeration is likely necessary.

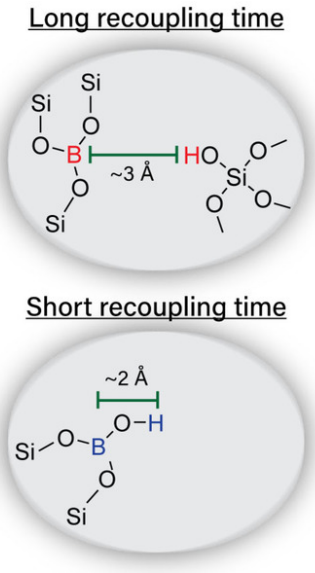

Figure 2.8 Simplified illustration of the two different ^{1}H-^{11}B interactions observed in the 2D $^{11}B \rightarrow {}^{1}H$ D-RINEPT spectra (ref. 8).

While our previous studies have been successful in differentiating boron species based on proximity to protons, we have been limited in the ability to elucidate differences in long- and short-range boron-boron connectivity. This limitation stems from the intense signal overlap that occurs at typical external magnetic fields (B_0). ^{11}B is a spin I = 3/2 half-integer quadrupolar nucleus that gives rise to SSNMR spectra that are broadened by the second order quadrupolar interaction (QI), The broadening of central-transition (CT) NMR signals by the second-order QI is proportional to the square of C_Q. C_Q is related to the symmetry at the nucleus, with trigonal planar boron sites having C_Q values between 2.5 and 3

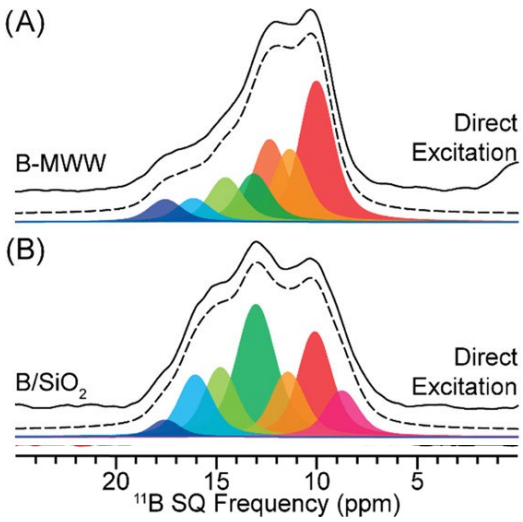

Figure 2.9 1D ^{11}B spectra of (a) B-MWW and (b) B/SiO_2 acquired at B_0 = 35 T (ref. 9).

MHz, while for tetrahedral sites, C_Q is generally less than 1 MHz. Fortunately, the broadening of the CT NMR signals by the second-order QI is inversely proportional to magnetic field strength (B_0). Therefore, increasing B_0 decreases the second-order QI and results in narrower ^{11}B NMR signals.

Further elucidation of the boron molecular structure and connectivity on B/SiO_2 and B-MWW was performed by ultra-high field (35 T) MAS SSNMR.[9] At 35 T, 1D ^{11}B signals are near isotropic in nature, resulting in high resolution spectra and allowing for straightforward identification of all species in a sample. Most importantly, the sensitivity offered at 35 T is enough to record 2D ^{11}B double quantum-single quantum (DQ-SQ) homonuclear correlation NMR spectra and line narrowing in both dimensions provides the resolution to unambiguously determine the structure on boron-

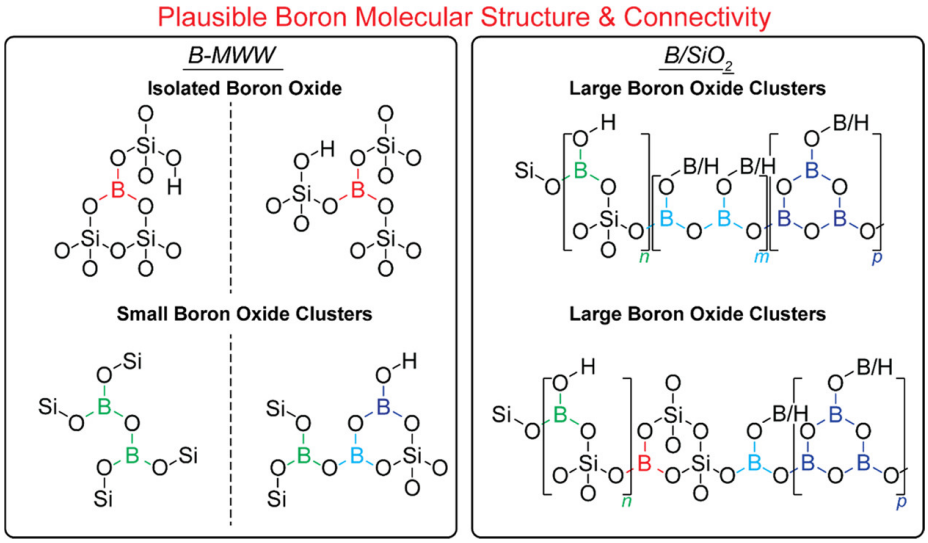

Figure 2.10 Plausible boron structural motifs present in B-MWW and B/SIO2. The colors of the individual boron atoms correspond to the peaks in Figures 2.9 and 2.11 (ref. 9).

based materials. 1D ^{11}B spectra of B/SIO_2 and B-MWW are shown in Figure 2.9. Analytical simulations (dashed lines) are shown below the experimental spectra (solid lines). The individual peaks are color coded and correspond to the proposed structures in Figure 2.10. The deconvoluted spectra in Figure 2.9 show that in the B-MWW material, the largest proportion of species appear at lower frequency, corresponding to isolated boron oxide species (Figure 2.10), confirming our previous results.

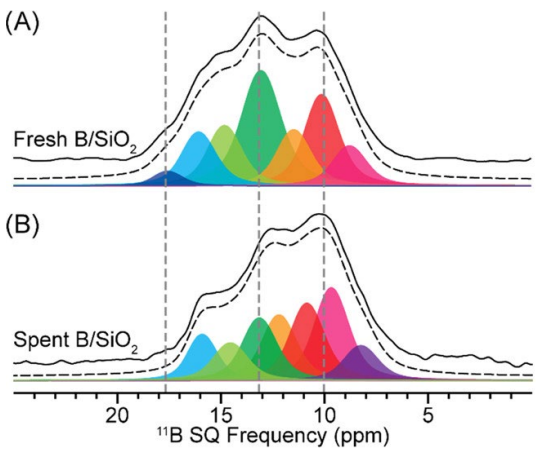

Figure 2.11 1D ^{11}B spectra of (A) fresh and (B) spent B/SiO_2 acquired at B_0 = 35 T (ref. 9).

A comparison of the 1D ^{11}B direct excitation spectra acquired at 35 T (Figure 2.11) clearly shows the changes in speciation that occurred during the ODH reaction. The higher frequency boron species, corresponding to large boroxol rings (dark blue species in Figure 2.10), have been removed during the reaction. Overall, a more even distribution of species is left on the surface after reaction. Interestingly, B/SiO_2 exhibits an induction period, where the initial propane conversion is *ca.* double the steady state conversion. The boroxol rings are likely leached from the surface during the induction period as the surface restructures to reveal the stable active phase. Therefore, these NMR results suggest that the boroxol ring species present on the fresh material are more active but less stable than the species that remain on the surface, accounting for the loss of conversion during the induction period.

In summary, all these studies of the catalytic surface have confirmed that an amorphous mixed boron oxide hydroxide phase is responsible for catalytic activity. The exact structure of the active site can likely not be observed using *ex situ* characterization, but MAS SSNMR combined with materials synthesis can help establish to correlations between activity and structure.

2.2. Kinetics and Mechanism

ODH over boron-based catalysts proceeds via a gas-phase radical pathway, initiated by the surface.[10-12] The reaction has an apparent second order dependence with respect to alkane and a fractional order dependence with respect to oxygen.[13-14] The product distribution is affected by the O_2 concentration in the gas phase, with C-C cracking products favored at low concentration and ODH products favored at high, as is seen in the plot of product formation rate as a function of oxygen partial pressure (Figure 2.12).[13] In support of the hypothesized radical mechanism, methyl radicals were observed by synchrotron vacuum ultraviolet photoionization mass spectrometry (SVUV-PIMS) during propane ODH over hBN.[15] Additionally, a recent microkinetic modelling study found that the high selectivity to propylene and ethylene is consistent with a gas-phase conversion mechanism.[12]

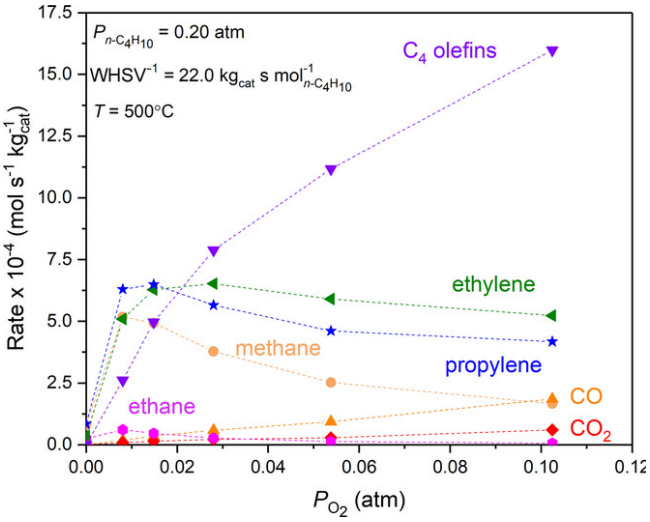

Figure 2.12 Product formation rate as a function of the partial pressure of O_2 in the ODH of *n*-butane (ref 13).

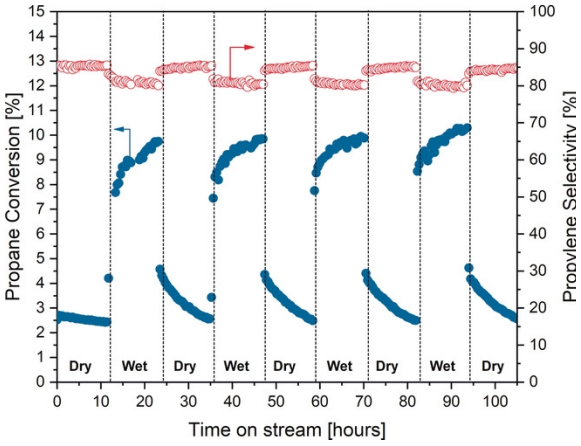

Figure 2.13 Propane conversion (blue symbols, left axis) and propylene selectivity (red symbols, right axis) as a function of time-on-stream during 12 h cycles of "wet" or "dry" ODH feed. Prior to cycling, the catalyst had undergone ODH under wet conditions for 24 h, and subsequently ODH under dry conditions for 24 h. T=525 °C, F_{total}=40 mL_{STP} min^{-1}. Dry feed: 30 % C_3H_8, 15 % O_2, 55 % N_2. Wet feed: 30 % C_3H_8, 15 % O_2, 45 % N_2, 10 % H_2O (ref. 11).

Previous studies of other radical-generating catalysts showed water to have an effect on reactivity. Indeed, when steam is cofed into the reactor, there is a large increase in the

reaction rate.[11] This enhancement effect is reversible, as seen in Figure 2.13. When steam is added, there is an immediate step change of ~10%, followed by a more gradual change of 2 % over the course of the 12 h cycle. The large step change is attributed to a change in the radical population, while the more gradual change is attributed to the surface, although the effects of steam on the catalyst surface have not yet been experimentally investigated.

2.3. Current Active Site Hypothesis

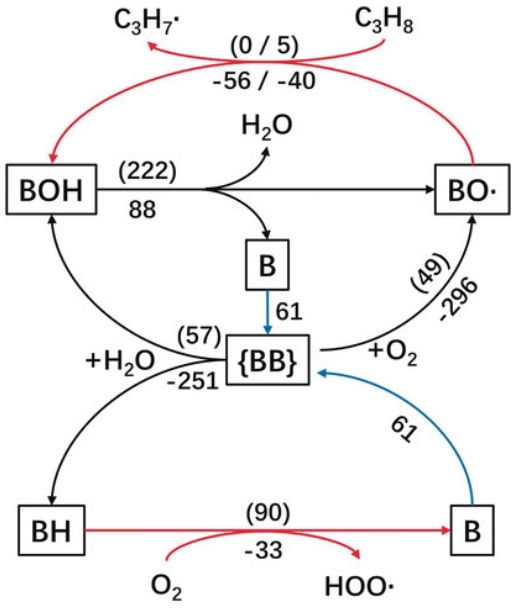

Figure 2.14 Proposed reaction mechanism showing key surface reactions. The energetics (in kJ mol^{-1}) of each step are labeled along the corresponding arrows, with numbers inside and outside the parentheses standing for reaction barrier and ΔG, respectively (ref. 11).

Our current active site hypothesis, based on a combined computational and experimental study, is that a metastable oxygen-deficient {BB} species can activate O_2 to form BO• sites (Figure 2.14).[11] These surface radical species can abstract hydrogen from propane to form a B-OH species and an alkyl radical that continues on to react with other gas-phase radicals. BO• can also react with water, forming B-OH and B-H. The B-H species can react with O2 to generate radical species and an undersaturated boron site. Any reaction of BO• results in the formation of B-OH, which is relatively unreactive. We have proposed a regeneration step in which water assists in the dehydration of the surface (Figure 2.15). The proposed step has the highest calculated energy barrier of all steps in Figure 2.14 (222 kJ mol^{-1}), suggesting that active site regeneration is kinetically slow.

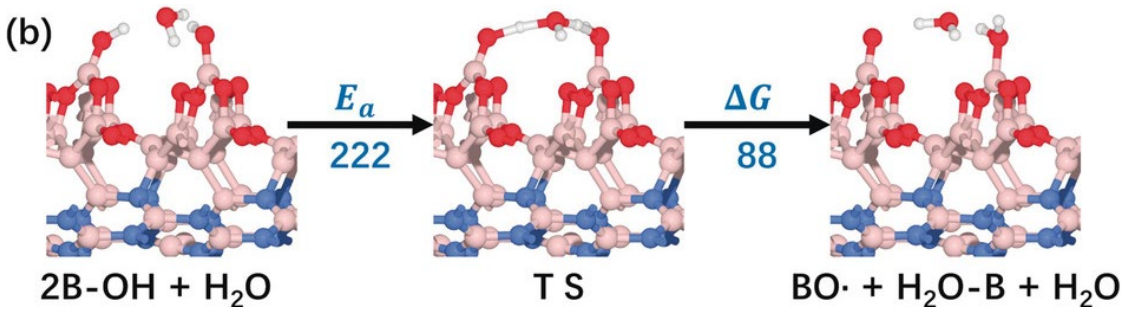

Figure 2.15 Structural model showing the water-catalyzed surface dehydration step that regenerates the active site (ref. 11)

2.4. My Approach to Studying This System

To summarize the main takeaways from the previous studies:

1. ODH proceeds via a radical mechanism initiated by the boron surface.
2. An oxidized boron phase is responsible for catalytic activity.
3. The active boron oxide phase is molten and dynamic under reaction conditions.
4. We hypothesize that a metastable oxygen-deficient {BB} site is responsible for activity.
5. We hypothesize that active site regeneration by dehydrating B-OH groups is kinetically slow.

The remaining questions that motivate the studies in this thesis are:

1. What are the surface requirements for activity?
2. How does the active phase form?

To answer these questions, I use two different approaches:

Approach 1: Make a controlled surface with different levels of boron agglomeration to probe the effect of agglomeration on activity (Chapter 3)

Approach 2: Use *in situ/operando* x-ray spectroscopy to watch the formation of the active boron oxide phase during the catalyst induction period (Chapters 4 and 5)

2.5 References

(1) Grant, J. T.; Carrero, C. A.; Goeltl, F.; Venegas, J.; Mueller, P.; Burt, S. P.; Specht, S. E.; McDermott, W. P.; Chieregato, A.; Hermans, I., Selective Oxidative Dehydrogenation of Propane to Propene Using Boron Nitride Catalysts. *Science (Washington, DC, U. S.)* **2016,** *354* (6319), 1570-1573. 10.1126/science.aaf7885.

(2) Grant, J. T.; McDermott, W. P.; Venegas, J. M.; Burt, S. P.; Micka, J.; Phivilay, S. P.; Carrero, C. A.; Hermans, I., Boron and Boron-Containing Catalysts for the Oxidative Dehydrogenation of Propane. *ChemCatChem* **2017,** *9* (19), 3623-3626. 10.1002/cctc.201701140.

(3) Love, A. M.; Thomas, B.; Specht, S. E.; Hanrahan, M. P.; Venegas, J. M.; Burt, S. P.; Grant, J. T.; Cendejas, M. C.; McDermott, W. P.; Rossini, A. J., et al., Probing the Transformation of Boron Nitride Catalysts under Oxidative Dehydrogenation Conditions. *J. Am. Chem. Soc.* **2019,** *141* (1), 182-190. 10.1021/jacs.8b08165.

(4) Love, A. M.; Cendejas, M. C.; Thomas, B.; McDermott, W. P.; Uchupalanun, P.; Kruszynski, C.; Burt, S. P.; Agbi, T.; Rossini, A. J.; Hermans, I., Synthesis and Characterization of Silica-Supported Boron Oxide Catalysts for the Oxidative Dehydrogenation of Propane. *J. Phys. Chem. C* **2019,** *123* (44), 27000-27011. 10.1021/acs.jpcc.9b07429.

(5) Grant, J. T.; Love, A. M.; Carrero, C. A.; Huang, F.; Panger, J.; Verel, R.; Hermans, I., Improved Supported Metal Oxides for the Oxidative Dehydrogenation of Propane. *Topics in Catalysis* **2016,** *59* (17), 1545-1553. 10.1007/s11244-016-0671-2.

(6) Love, A. M.; Carrero, C. A.; Chieregato, A.; Grant, J. T.; Conrad, S.; Verel, R.; Hermans, I., Elucidation of Anchoring and Restructuring Steps During Synthesis of Silica-Supported Vanadium Oxide Catalysts. *Chemistry of Materials* **2016,** *28* (15), 5495-5504. 10.1021/acs.chemmater.6b02118.

(7) Zhang, Z.; Jimenez-Izal, E.; Hermans, I.; Alexandrova, A. N., Dynamic Phase Diagram of Catalytic Surface of Hexagonal Boron Nitride under Conditions of Oxidative Dehydrogenation of Propane. *J. Phys. Chem. Lett.* **2019,** *10* (1), 20-25. 10.1021/acs.jpclett.8b03373.

(8) Altvater, N. R.; Dorn, R. W.; Cendejas, M. C.; McDermott, W. P.; Thomas, B.; Rossini, A. J.; Hermans, I., B-Mww Zeolite: The Case against Single-Site Catalysis. *Angew. Chem., Int. Ed.* **2020,** *59* (16), 6546-6550. 10.1002/anie.201914696.

(9) Dorn, R. W.; Cendejas, M. C.; Chen, K.; Hung, I.; Altvater, N. R.; McDermott, W. P.; Gan, Z.; Hermans, I.; Rossini, A. J., Structure Determination of Boron-Based Oxidative Dehydrogenation Heterogeneous Catalysts with Ultrahigh Field 35.2 T 11B Solid-State NMR Spectroscopy. *ACS Catal.* **2020,** *10* (23), 13852-13866. 10.1021/acscatal.0c03762.

(10) Venegas, J. M.; Hermans, I., The Influence of Reactor Parameters on the Boron Nitride-Catalyzed Oxidative Dehydrogenation of Propane. *Org. Process Res. Dev.* **2018,** *22* (12), 1644-1652. 10.1021/acs.oprd.8b00301.

(11) Venegas, J. M.; Zhang, Z.; Agbi, T. O.; McDermott, W. P.; Alexandrova, A.; Hermans, I., Why Boron Nitride Is Such a Selective Catalyst for the Oxidative Dehydrogenation of Propane. *Angew. Chem., Int. Ed.* **2020,** *59* (38), 16527-16535. 10.1002/anie.202003695.

(12) Kraus, P.; Lindstedt, R. P., It's a Gas: Oxidative Dehydrogenation of Propane over Boron Nitride Catalysts. *J. Phys. Chem. C* **2021,** *125* (10), 5623-5634. 10.1021/acs.jpcc.1c00165.

(13) McDermott, W. P.; Venegas, J.; Hermans, I., Selective Oxidative Cracking of N-Butane to Light Olefins over Hexagonal Boron Nitride with Limited Formation of Cox. *ChemSusChem* **2020,** *13* (1), 152-158. 10.1002/cssc.201901663.

(14) Venegas, J. M.; Grant, J. T.; McDermott, W. P.; Burt, S. P.; Micka, J.; Carrero, C. A.; Hermans, I., Selective Oxidation of N-Butane and Isobutane Catalyzed by Boron Nitride. *ChemCatChem* **2017,** *9* (12), 2118-2127. 10.1002/cctc.201601686.

(15) Zhang, X.; You, R.; Wei, Z.; Jiang, X.; Yang, J.; Pan, Y.; Wu, P.; Jia, Q.; Bao, Z.; Bai, L., et al., Radical Chemistry and Reaction Mechanisms of Propane Oxidative Dehydrogenation over

Hexagonal Boron Nitride Catalysts. *Angew. Chem., Int. Ed.* **2020,** *59* (21), 8042-8046. 10.1002/anie.202002440.

CHAPTER 3

Controlled Grafting Synthesis of Silica-Supported Boron for Oxidative Dehydrogenation Catalysis

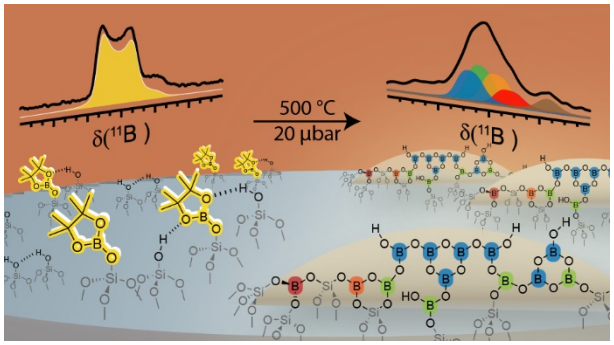

This chapter has been published under the following: Cendejas, M. C.; Dorn, R. W.; McDermott, W. P.; Lebrón-Rodríguez, E. A.; Mark, L. O.; Rossini, A. J.; Hermans, I., Controlled Grafting Synthesis of Silica-Supported Boron for Oxidative Dehydrogenation Catalysis. *The Journal of Physical Chemistry C* **2021,** *125* (23), 12636-12649. 10.1021/acs.jpcc.1c01899.

Supporting Information for Chapter 3 is presented in Appendix A.

Chapter 3: Controlled Grafting Synthesis of Silica-Supported Boron for Oxidative Dehydrogenation Catalysis

3.1 Introduction

Boron-based materials are promising catalysts for the selective oxidative dehydrogenation (ODH) of light alkanes to olefins.[1-6] The production of light olefins is an important industrial reaction that currently requires high energy consumption.[7] Improvements in catalysts that produce light olefins can result in large energy savings for the chemical industry.[8] In the ODH of propane to propylene, boron-based materials, such as hexagonal boron nitride (hBN), metal borides, and elemental boron, show higher selectivity to propylene (e.g., 80% selectivity at 8% conversion) than the previous state-of-the-art supported vanadium oxide catalysts (e.g., 60% selectivity at 8% conversion for V/SiO_2).[1] Importantly, the main side-product of propane ODH over boron-based materials is ethylene, another important olefin, rather than CO and CO_2 that is seen for supported metal oxides. The origin and mechanism of this exceptional behavior has been the subject of many recent studies.[9-17]

ODH over boron-based catalysts is proposed to proceed via a radical mechanism.[9-10, 14, 18] The product distribution is mainly determined by the gas phase radical chemistry, with selectivity being controlled by the O_2 partial pressure.[3, 14] The role of the surface is to initiate the reaction by forming radicals that propagate in the gas phase, leading to the exceptional selectivity.[10] A mixed boron oxide/hydroxide phase, $B_2(OH)_{2x}O_{3-x}$ (x = 0-3), has been identified by ^{11}B solid-state NMR spectroscopy, along with electron microscopy, X-ray photoelectron and soft x-ray absorption spectroscopy, as necessary for catalytic activity.[15-16, 19-21] This boron oxide/hydroxide layer is predicted by theory to be highly dynamic at elevated temperature under an oxidizing atmosphere.[22] Under such conditions, the oxidized boron layer can access many stoichiometries of boron and oxygen and can form several structures within a given stoichiometry. A recent combined catalysis and theory study identified a metastable, unsaturated {BB} unit as a potential

active site whose reactivity can explain the peculiar kinetic behavior observed for B-based ODH catalysts.[10]

The unsaturated {BB} metastable active site hypothesis means that *ex situ* characterization cannot directly observe active species due to their short lifetime. Instead, *ex situ* characterization of catalysts before and after reaction is utilized to understand what type of boron species supported on the surface of silica are required to generate ODH active sites. For example, boron isomorphously substituted into a zeolite framework via hydrothermal synthesis (B-MWW) gives rise to stable BO_3-type species, with the major species being isolated **B**$(OSi)_3$ in the zeolite framework.[17] Notably, B-MWW is inactive for propane ODH and does not restructure under reaction conditions. When boron is post-synthetically immobilized on the B-MWW surface *via* incipient wetness impregnation, producing agglomerated boron oxide/hydroxide, the material becomes active for propane ODH.[17] These results indicate that isolated BO_3 species are not active and that boron agglomeration is likely necessary for active site formation. This conclusion is in line with the theory-predicted boron-rich metastable active site and has led us to investigate the extent of boron agglomeration necessary for catalytic activity. Therefore, molecular-level control over the boron speciation is essential to better understand the extent of boron agglomeration required for catalytic activity, thus facilitating the rational design and development of next-generation ODH catalysts.

In our group's previous work with silica-supported boron oxide (B/SiO_2), we synthesized a series of B/SiO_2 materials with different weight loadings of boron via incipient wetness impregnation (B/SiO_2-IWI) using a triisopropyl borate solution.[19] The motivation behind this synthesis was to generate different surface coverages of boron oxide, thereby generating different species ranging from isolated to polymeric to nanoparticulate, as is commonly done with supported metal oxides.[23-24] Instead, we found that boron speciation – and propylene selectivity – was independent of boron weight loading. While we could observe that the supported boron oxide/hydroxide layer restructured during catalysis *via* ^{11}B solid-state NMR spectroscopy, the

distribution of species and their dynamics under reaction conditions for the series of B/SiO_2-IWI catalysts made assigning reactivity to any individual structure intangible.

Grafting chemistry is often employed in catalyst synthesis to control the density and speciation of (transition metal) active sites. Such studies, coupled with detailed catalytic and spectroscopic characterization, have led to mechanistic insights for a variety of reactions such as olefin polymerization and hydrogenolysis.[25-26] Grafted materials can also be used to investigate the formation of active species; insights from such studies often inform the rational synthesis of improved catalytic materials.[27-28] In this study, we describe the controlled grafting synthesis of a boron precursor on amorphous silica. Each grafted material is thermally treated to remove the thermolytic precursor[29-30] and evaluated as a propane ODH catalyst. The structures of the as-grafted, thermally treated, and catalytically tested materials were determined by solid-state NMR and IR spectroscopies.

3.2 Materials and Methods

3.2.1 Material Synthesis

Bpin/SiO_2 materials were synthesized via grafting chemistry. Silica powder (Aerosil 300 from Evonik, specific surface area *ca.* 300 m^2g^{-1}) was dehydrated overnight at 200, 700, or 900 °C under vacuum (20 μbar) and stored in a N_2 glovebox (≤ 1 ppm O_2 and H_2O) to prevent rehydration. These support materials are denoted as $SiO_{2(T)}$, where T refers to the dehydration temperature.

Pinacolborane (HBpin, Millipore-Sigma, distilled once before use) was deposited in the gas phase onto 500 mg pretreated silica cooled to -196 °C (5 equiv. based on initial silanol content) at *ca.* 20 μbar static vacuum (process illustrated in Figure S1). The transfer period (*ca*. 20 min) was followed by a reaction period at room temperature (30 min) and a mild thermal post-treatment at 50 °C and 20 μbar dynamic vacuum (1 h) to remove unreacted precursor. The materials at this stage are called Bpin/$SiO_{2(T)}$ and stored in a N_2 glovebox. Thermal treatment of

the Bpin/$SiO_{2(T)}$ materials was done at 20 μbar dynamic vacuum and 500 °C (5 °C min^{-1}) for 10 hours. The materials at this stage are denoted in the figures as Bpin/$SiO_{2(T)}$-^{500v} and **ST** (**T** = **2**, **7**, or **9**, referring to the initial support dehydration temperature) in the text.

N,*N*-Bis(trimethylsilyl)methylamine, or $(TMS)_2NMe$, (Millipore-Sigma, distilled twice before use) was used for the silylation of $SiO_{2(700)}$ (denoted as TMS-$SiO_{2(700)}$). The silylating agent was exposed to the dried silica under 20 μbar vacuum in the same way as HBpin (using 5 equiv based on initial silanol content) and thermally post-treated at 250 °C. Afterward, HBpin was deposited onto the silylated material to obtain Bpin/TMS-$SiO_{2(700)}$ (5 equiv based on initial silanol content).

3.2.2 Catalytic Testing

Bpin/$SiO_{2(T)}$-^{500v} catalysts were compressed using a pellet press (Pike Technologies; pressure program: 5 tons of force for 90 s and 7 tons of force for 60 s) and sieved to collect particles of 300–600 μm diameter to limit any potential mass transfer effects.[18] About 25–50 mg of Bpin/$SiO_{2(T)}$-^{500v} was diluted in quartz chips in a 1:2 ratio and loaded into a quartz reactor tube (8 mm i.d.) and supported on a bed of quartz wool in the middle of the tube. Additional quartz wool was used to pack the inside of the quartz tube lightly past the catalyst bed to reduce dead volume. Flow rates of C_3H_8 (instrument grade, Matheson), O_2 (UHP, Airgas), and N_2 (UHP, Airgas) were controlled by using three mass flow controllers (Bronkhorst) and calibrated to each individual gas to allow total flow rates of 40–200 mL min^{-1}. The H_2O produced from the reaction was condensed using a thermoelectrically cooled condenser held at −5 °C. The dried reactor effluent was monitored by using an online μGC (Inficon micro GC fusion gas analyzer) equipped with three GC modules and three microthermal conductivity detectors (μTCD). O_2, N_2, CH_4, and CO were analyzed by using a Rt-molsieve 5A column, CO_2 was analyzed by using an Rt-U-bond column, and all hydrocarbons apart from CH_4 were analyzed using an Rt-alumina bond/Na_2SO_4 column.

In each catalytic test, the reactor was heated to the reaction temperature of 500 °C under O_2 and N_2 flow. The temperature was controlled by using a thermocouple inserted into the middle

of the catalyst bed. After the temperature was stabilized, the C_3H_8 feed was introduced and GC measurements were begun. As there is an induction period before catalytic activity is stabilized, each catalyst was treated for 24 h under a feed of 6:3:11 C_3H_8:O_2:N_2 at 40 mL min^{-1}. After this treatment, the gas flow rate was adjusted to give $WHSV^{-1}$ values ranging from 0.6 to 6.3 kg_{cat} s mol_{C3H8}^{-1} (ca. 40–200 mL min^{-1}), and further GC measurements were performed. Reported experiments showed the carbon balance closed within ±3%.

3.2.2 Materials Characterization

IR Spectroscopy. IR spectra were recorded on a self-supporting wafer using a Bruker Alpha spectrometer in transmission mode (resolution of 2 cm^{-1}). Intensities were normalized to the Si–O–Si overtones of the silica framework. Analysis was performed inside a glovebox (<1 ppm of H_2O and O_2).

ICP-MS. Boron elemental analysis was performed with ICP-MS (Agilent 5110 ICP-MS). Prior to measurement, ~20 mg of sample was digested using 200 uL of 48 wt% HF (Sigma-Aldrich), after which the solution was diluted to 10 mL with DI water and diluted again to a 1:10 ratio for analysis. HF is extremely dangerous and should be handled with caution.

NMR Spectroscopy (UW Madison). One-dimensional direct excitation ^{11}B spin echo (Bpin/$SiO_{2(T)}$ materials) and dipolar double-quantum-single-quantum homonuclear correlation (Bpin/$SiO_{2(T)}$-^{500v} materials) spectra were recorded at the University of Wisconsin – Madison on a 11.7 T ($v_0(^1H)$ = 500 MHz) Bruker standard bore NMR spectrometer equipped with an Avance III console and a 4 mm magic-angle spinning (MAS) HXY NMR probe. All samples were packed into 4 mm zirconia NMR rotors in an N_2 filled glovebox and spun with N_2 gas to avoid any hydration of the silica surface. Chemical shifts were calibrated on each sample with ^1H chemical shifts referenced to neat tetramethylsilane (TMS) with adamantane as a secondary chemical shift reference ($\delta(^1H)$ = 1.82 ppm). ^{11}B shifts were referenced using previously reported IUPAC recommended relative

NMR frequencies.[31] All spectra were processed using the Bruker Topspin 3.6.1 NMR software. Analytical simulations of the ^{11}B NMR spectra were performed using the solid lineshape analysis (sola) module implemented in Bruker Topspin 3.6.1.

All experimental details (magnetic field strength, number of scans, recycle delay, t_1 TD points, t_1 dwell (Δt_1), dipolar recoupling duration and total experimental times) are given in Table S1. 1D direct excitation ^{11}B NMR spectra were recorded with a rotor synchronized spin echo NMR pulse sequence. ^{11}B CT-selective π/2 and π pulse lengths were 8.2 and 16.4 μs in duration, corresponding to a *ca.* 15.2 kHz RF field and *ca.* 30.4 kHz central-transition (CT) nutation frequency. ^{11}B dipolar DQ-SQ homonuclear correlation NMR experiments were recorded with the $R2_2^1$ homonuclear dipolar recoupling sequence.[32-33] A CT selective π pulse was applied during t_1 evolution to ensure only correlations from two ^{11}B spins are observed.[32-33] Rotor-assisted population transfer (RAPT) was applied ± 500 kHz off resonance to the ^{11}B spins prior to all DQ-SQ NMR experiment to enhance the ^{11}B CT population.[34-36]

NMR Spectroscopy (Iowa State University). Solid-state NMR spectra were recorded at B_0 = 14.1 T ($\nu_0(^1H)$ = 600 MHz) or 9.4 T ($\nu_0(^1H)$ = 400 MHz). The 14.1 T Bruker wide-bore NMR spectrometer was equipped with a Bruker Avance II console and a 2.5 mm magic angle spinning (MAS) HXY NMR probe configured in double resonance mode. The 9.4 T Bruker wide-bore NMR spectrometer was equipped with a Bruker Avance III HD console, a 3.2 mm MAS HXY dynamic nuclear polarization (DNP) NMR probe configured in double resonance mode and a Bruker DNP liquid N_2 cooled low temperature MAS unit to reach sample temperatures of *ca.* 100 K. All samples were packed into the appropriate size NMR rotor (zirconia 2.5 mm rotor or sapphire 3.2 mm rotor with a silicon plug) in an N_2 filled glovebox and spun with N_2 gas to avoid hydration. Chemical shifts were calibrated by using neat tetramethylsilane (TMS) with adamantane as a secondary chemical shift reference ($\delta(^1H)$ = 1.82 ppm). The 9.4 T chemical shifts were calibrated at 100 K by using the ^{1}H NMR signal of frozen 1,1,2,2-tetrachloroethane (TCE) as a secondary chemical

shift reference ($\delta(^1H)$ = 6.2 ppm). ^{11}B and ^{29}Si shifts were referenced using previously reported IUPAC recommended relative NMR frequencies.[31] All spectra were processed using the Bruker Topspin 3.6.1 NMR software. Analytical simulations of the ^{11}B NMR spectra were performed using the solid lineshape analysis (sola) module as implemented in Bruker Topspin 3.6.1.

All experimental details (magnetic field strength, MAS frequency, number of scans, recycle delay, t_1 TD points, t_1 dwell (Δt_1), dipolar recoupling duration and total experimental times) are given in Table S1. A 1D ^{11}B rotor synchronized spin echo spectrum was recorded at B_0 = 9.4 T with 10 kHz MAS and a sample temperature of *ca.* 100 K. The ^{11}B central-transition (CT) selective π/2 and π pulse lengths were 10 and 20 μs in duration, corresponding to a 12.5 kHz radio frequency (RF) field and 25 kHz CT nutation frequency. 100 kHz ^1H RF field of SPINAL-64 heteronuclear decoupling was performed throughout the entire spin echo sequence and acquisition of ^{11}B.[37]

All solid-state NMR experimental details discussed below are with respect to spectra recorded on the 14.1 T NMR spectrometer. ^1H π/2 and π pulse lengths were 2.5 and 5.0 μs in duration, corresponding to a 100 kHz RF field. ^{11}B CT-selective π/2 and π pulse lengths were 15 and 30 μs in duration, corresponding to an 8.3 kHz RF field and 16.7 kHz CT nutation frequency. ^1H dipolar double-quantum-single-quantum (DQ-SQ) homonuclear correlation NMR experiments were recorded with the previously described back-to-back (BABA) NMR pulse sequence.[38-39] The π/2 pulse length in the homonuclear recoupling block was 2.5 μs in duration, corresponding to a 100 kHz RF field. Each homonuclear recoupling block was 40 μs in duration (1 rotor cycle). ^1H-^{11}B heteronuclear correlation (HETCOR) NMR experiments were performed with either (Bpin/$SiO_{2(200)}$, all of the fresh and spent Bpin/$SiO_{2(T)}$-500v catalysts) $^{11}B \rightarrow {}^1H$ dipolar refocused INEPT (D-RINEPT)[40-41] or (Bpin/$SiO_{2(700)}$ and Bpin/$SiO_{2(900)}$) ^1H-^{11}B t_1-noise eliminated dipolar HMQC-3 (TONE DHMQC-3)[42] NMR pulse sequences. 1D $^{11}B \rightarrow {}^1H$ D-RINEPT and $^1H\{^{11}B\}$ TONE D-HMQC-3 experiments were performed on all samples to identify which experiment was more sensitivity (i.e., yielded largest signal intensity per unit of time). The pulse sequence with the

greatest sensitivity was chosen to record 2D HETCOR spectra. All ^{1}H-^{11}B HETCOR NMR experiments were recorded with the symmetry-based $SR4_1^2$ heteronuclear dipolar recoupling sequence applied to the ^{1}H spins to re-introduce ^{1}H-^{11}B dipolar couplings (50 kHz RF field at 25 kHz MAS).[43] Rotor-assisted population transfer (RAPT) was applied $\pm$ 550 or 650 kHz off resonance to the ^{11}B spins prior to all D-RINEPT experiments and during ^{1}H dipolar recoupling in TONE DHMQC-3 experiments to enhance the ^{11}B CT population.[34-36] ^{1}H{^{11}B} TONE DHMQC-3 experiments were acquired with a 360 (9 rotor periods) or 480 (12 rotor periods) µs 100 kHz ^{1}H RF field Lee-Goldberg (LG) spin-lock pulse (offset: 70.7 kHz – effective RF field: 122.4 kHz) to remove uncorrelated ^{1}H magnetization.[42] ^{1}H-detected ^{1}H-^{29}Si cross-polarization (CP) HETCOR experiments were performed with previously published NMR pulse sequences: ^{1}H→^{29}Si forward CP, ^{29}Si Z-filter, ^{1}H saturation at the HORROR condition (~ 400 ms in duration: 12.5 kHz RF field @ 25 kHz MAS) and ^{29}Si→^{1}H back CP for ^{1}H-detection.[44-45] Forward and backward ^{1}H→^{29}Si CP was achieved with simultaneous spin-lock pulses applied to the ^{1}H (with a 90-100 % ramp) and ^{29}Si spins with RF fields of *ca.* 60 and 32 kHz, respectively (25 kHz MAS). A schematic illustration of all pulse sequences is shown in Figure S2.

3.3. Results and Discussion

3.3.1. The effect of support dehydration temperature on HBpin grafting.

The controlled dispersion of boron on silica has mainly been studied for the synthesis of doped electronic materials.[46-47] The boron molecules used in these prior grafting studies react with the surface via organoboron or borane functionalities to generate single sites (structures shown in Figure S3). However, these compounds often require synthesis or have a long lead times from commercial sources. Here, we use pinacolborane (HBpin) to controllably graft boron onto the surface of silica. The choice of HBpin for grafting is based on the phenanthrene dioxoborane precursor used by Mathey *et al*. (Figure S3A), which appeared to generate controlled boron sites when grafted to SiO_2 dehydrated at 500 °C.[46] The B-H bond of HBpin can readily react

with silanol groups and the steric bulk of the pinacol ring should prevent close spacing of anchored precursors and the self-reaction between two precursor molecules. Additionally, HBpin is commercially available and relatively inexpensive because of its abundant use in organic reactions.

Prior to grafting, amorphous SiO_2 was first dehydrated at different temperatures to control the silanol density, denoted as $SiO_{2(T)}$, where T = 200, 700, or 900 °C. All materials were handled in a N_2-atmosphere glovebox to minimize rehydration of the treated silica surface. HBpin was transferred in the gas phase under reduced pressures (20 μbar) into a cooled Schlenk flask containing the pretreated $SiO_{2(T)}$. When the transfer was complete, the flask was slowly warmed to room temperature and the contents lightly shaken to ensure uniformity of the sample. After a reaction period of 30 minutes, the material was post-treated at 50 °C under reduced pressure (20 μbar) to remove any unreacted precursor. The reaction between HBpin and isolated silanol groups is shown at the top of Figure 3.1. The material at this stage is called $Bpin/SiO_{2(T)}$.

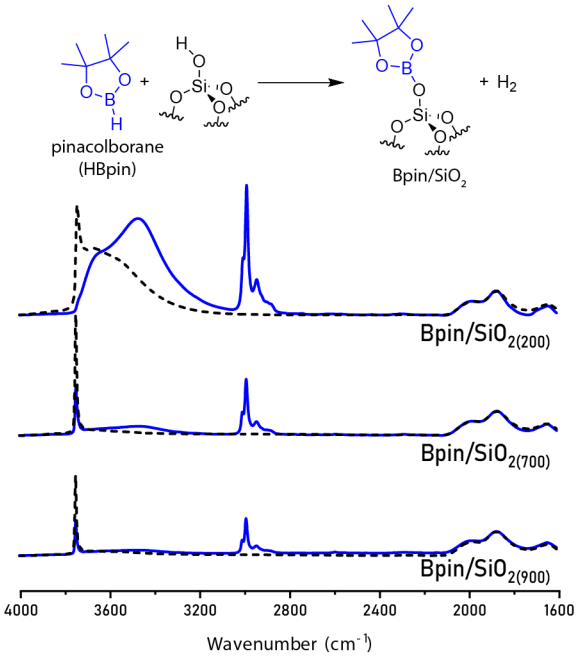

Figure 3.2. Transmission IR spectra of SiO_2 supports (black dashed lines) and HBpin grafted materials (blue solid lines). The intensity of each spectrum is normalized to the Si-O-Si overtone features at ca. 1870 cm^{-1}.

The structure of the grafted Bpin/$SiO_{2(T)}$ materials was probed by Fourier Transform Infrared (FTIR) and solid-state NMR spectroscopies. Transmission FTIR spectra of $SiO_{2(200,\ 700,\ 900)}$ contain a sharp peak at 3747 cm^{-1} which can be assigned to isolated silanol groups (Si-OH, Figure 3.1 – black dashed lines).[48-49] $SiO_{2(200)}$ features an intense, broad peak extending to *ca*. 3200 cm^{-1} which corresponds to hydrogen-bonded silanol groups. Not surprisingly, this broad feature extending from *ca.* 3750 – 3200 cm^{-1} is absent for the $SiO_{2(700,\ 900)}$ materials, consistent with reduced silanol density caused by increased dehydration temperatures (Table S2). After grafting with HBpin, new features in the C-H stretching region (3000-2850 cm^{-1}) appear, corresponding to the methyl groups of the Bpin precursor (Figure 3.1 – blue solid lines). There is an accompanying decrease in the signal intensity for isolated silanol groups at 3747 cm^{-1}. For Bpin/$SiO_{2(200)}$, nearly 100% of the isolated silanol groups are consumed while only *ca.* 70% of isolated silanols on $SiO_{2(700)}$ and $SiO_{2(900)}$ react with the precursor. Additionally, on each Bpin/$SiO_{2(T)}$ sample, a new, broad signal in the OH region appears, indicating a new hydrogen-bonding interaction upon grafting. This new hydrogen-bonding interaction is likely between an unreacted Si-OH group and grafted Bpin molecule. As expected, the intensity of the hydrogen-bonding feature is significantly reduced with increasing SiO_2 thermal treatment temperatures.

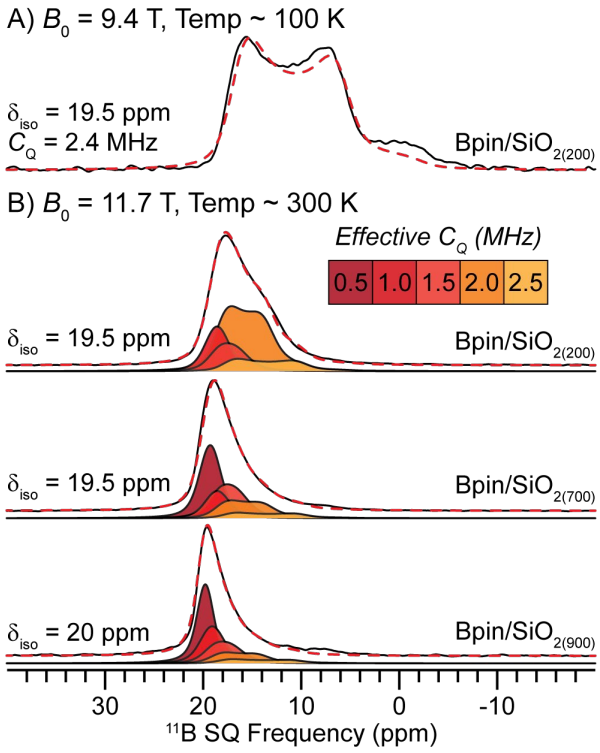

Figure 3.2. 1D direct excitation ^{11}B NMR spectra of (A and B, upper) Bpin/SiO$_{2(200)}$, (B, middle) Bpin/SiO$_{2(700)}$ and (B, lower) Bpin/SiO$_{2(900)}$ recorded at (A) 100 K and B_0 = 9.4 T with 10 kHz MAS or (B) room temperature and B_0 = 11.7 T with either (upper, lower) 10 or (middle) 12 kHz MAS. (A) The ^{11}B NMR spectrum was analytically simulated to a single site (red dashed line): δ_{iso} = 19.5 ppm, C_Q = 2.4 MHz and η = 0. (B) The ^{11}B NMR spectra were fit to multiple sites with identical δ_{iso} but varying C_Q from 0.5 – 2.5 MHz to represent partial averaging of the EFG tensor via reorientation about the B-O-Si bond (see Figure 3.1).

Solid-state NMR spectroscopy was used to further characterize the grafting of HBpin onto the SiO$_{2(T)}$ surface and probe the local hydrogen-bonding network surrounding the grafted Bpin molecule. One-dimensional (1D) direct excitation ^{11}B NMR spectra of Bpin/SiO$_{2(200)}$ were recorded at a sample temperature of either *ca.* 100 K or room temperature (Figure 3.2A, 3.22B upper, respectively). Interestingly, the two ^{11}B NMR spectra display significantly different features. At 100 K, a single, well-defined central-transition (CT) ^{11}B quadrupolar powder pattern is observed and can be simulated with an ^{11}B isotropic chemical shift (δ_{iso}) of 19.5 ppm, a quadrupolar coupling constant (C_Q) of 2.4 MHz and a quadrupolar asymmetry parameter (η) of 0, typical of 3-coordinate BO_3 species.[15, 21, 50-53] However, at room temperature, the lower frequency horn of the quadrupolar powder pattern is mostly absent, and the center of gravity peak position is shifted to a higher

frequency (Figure 3.2B, upper). The observation of a narrower signal with a higher center of gravity peak position at room temperature versus 100 K suggests that the ^{11}B electric field gradient (EFG) tensors are being partially averaged due to molecular motion. The partial averaging of the EFG tensors will essentially lead to a smaller effective C_Q.[54-55] Indeed, the room temperature ^{11}B NMR spectrum can be analytically simulated to multiple sites with $\delta_{iso}(^{11}B)$ of 19.5 ppm and C_Q varying from 0.5 to 2.5 MHz. Thus, comparison of room and low temperature ^{11}B NMR spectra reveal that Bpin/$SiO_{2(200)}$ contains only one boron species: Bpin monopodally grafted onto the silica surface (Figure 3.1 – upper). The distribution in C_Q observed for the room temperature ^{11}B NMR spectrum illustrates a distribution in the degree of mobility (*i.e.,* monopodal rotation about the B-O-Si bond).

1D ^{11}B NMR spectra of Bpin/$SiO_{2(700,\ 900)}$ were also recorded at room temperature and display similar trends observed for Bpin/$SiO_{2(200)}$, confirming the presence of only monopodally grafted Bpin (Figure 3.2B, middle and lower). Interestingly, the 1D ^{11}B NMR spectra become narrower with increasing support thermal treatment temperature, indicating that a higher fraction of surface boron species undergo faster reorientation. The difference in the degree of rotation is likely due to a reduced number of hydrogen-bonding silanol species surrounding the grafted Bpin molecule, consistent with the IR spectra discussed above. It should be noted that the room temperature ^{11}B NMR spectra of Bpin/$SiO_{2(T)}$ are consistent with that previously reported by Eedugurala *et al.*[56] Below, two-dimensional (2D) ^{1}H dipolar double-quantum-single-quantum (DQ-SQ) homonuclear and ^{1}H-^{11}B heteronuclear correlation (HETCOR) spectra of Bpin/$SiO_{2(200,\ 700,\ 900)}$ confirm molecular structure and further probe the hydrogen bonding network surrounding the grafted Bpin molecule. Figure 3.3A illustrates the proposed structures supported by the spectra in Figures 3.3B and C.

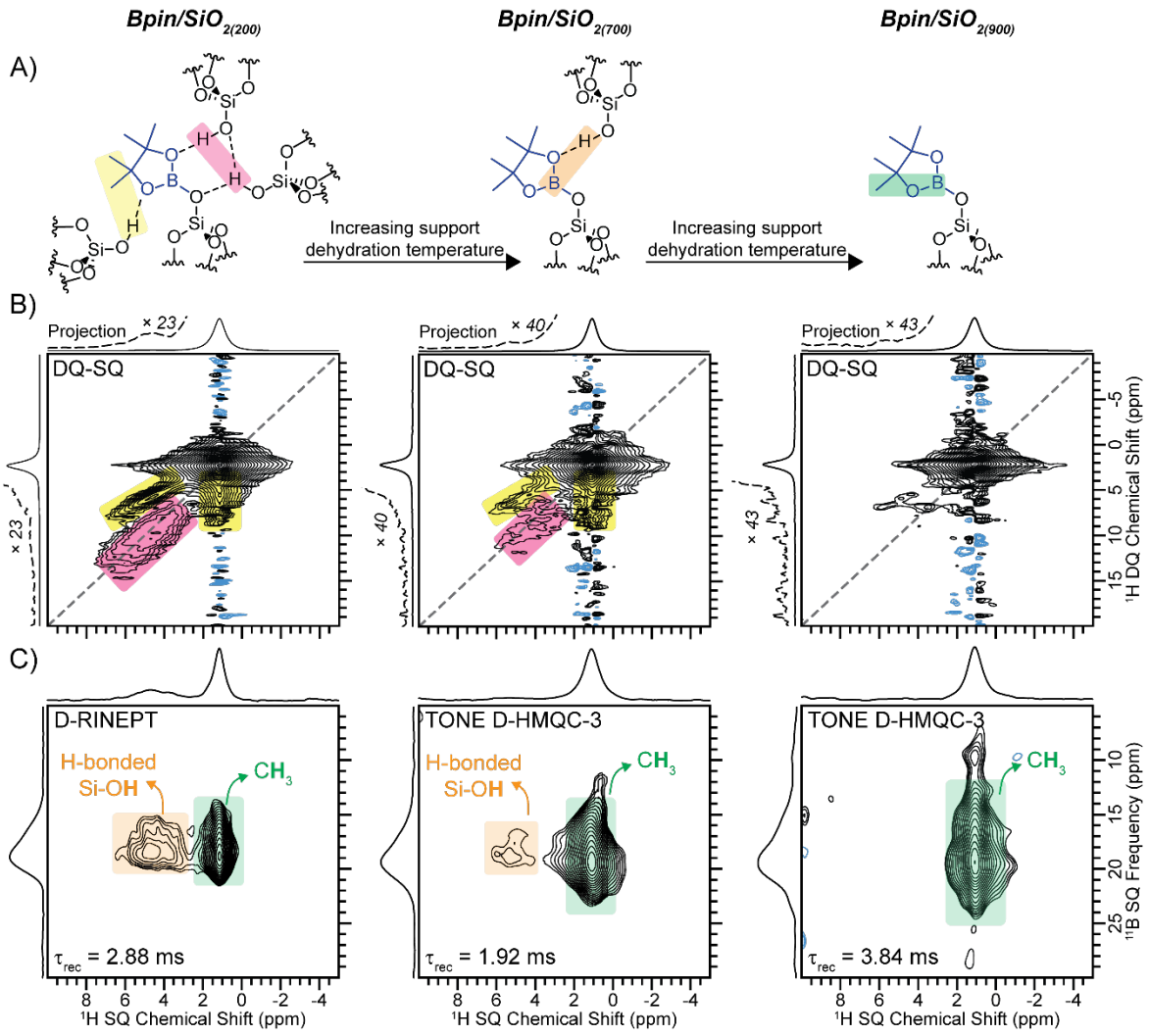

Figure 3.3. (A) Structural representation of Bpin grafted onto the surface of (left to right) Bpin/$SiO_{2(200)}$, Bpin/$SiO_{2(700)}$ or Bpin/$SiO_{2(900)}$. The number of near-by silanol groups is not exact and is merely used to illustrate the correlations observed in the 2D (B) ^{1}H DQ-SQ and (C) ^{1}H-^{11}B HETCOR spectra. The highlight boxes on the structures match the highlighted correlations overlaid on the 2D spectra. ^{1}H-^{11}B HETCOR spectra were recorded using either [Bpin/$SiO_{2(200)}$] ^{11}B→^{1}H D-RINEPT[40-41] or [Bpin/$SiO_{2(700,\ 900)}$] ^{1}H{^{11}B} TONE D-HMQC-3[42] pulse sequences. All NMR spectra were recorded at room temperature and B_0 = 14.1 T with 25 kHz MAS.

A 2D ^{1}H dipolar DQ-SQ homonuclear correlation NMR spectrum of Bpin/$SiO_{2(200)}$ reveals intense autocorrelations for ^{1}H SQ NMR signals *ca.* 1.5 and 4 – 7 ppm, corresponding, respectively, to the CH_3 methyl signals of Bpin and hydrogen-bonded silanol species on the silica surface (Si-OH - - HO-Si, Figure 3.3B, left and S4).[57] In addition, strong off-diagonal correlations

are observed between the CH_3 methyl signals of Bpin and the hydrogen bonded silanol species (CH_3 - - HO-Si, Figure 3.3B, left). The observed off-diagonal correlations reveal that silanol species are in close spatial proximity to the grafted Bpin molecule and the autocorrelations at *ca.* 4 – 7 ppm confirm that there are multiple silanol species surrounding the Bpin molecule in a hydrogen-bonded nest. A 2D ^{1}H-^{11}B HETCOR spectrum of Bpin/$SiO_{2(200)}$ further confirms that the silanol species are in close spatial proximity to the grafted Bpin molecule (Figure 3.3C, left), leading to the molecular structure proposed in Figure 3.3A (left). Here, three neighboring silanol groups are proposed to be surrounding the Bpin molecule based on integration of a ^{1}H direct excitation NMR spectrum (Figure S5). However, it should be noted that there is likely a significant source of error in this integration due to extensive signal broadening and the possibility of other types of hydrogen bonded silanols occurring on the surface. Nevertheless, the 2D spectra confirm that there are multiple silanol groups surrounding the grafted Bpin molecule in a hydrogen-bonded nest (Figure 3.3A, left).

2D ^{1}H DQ-SQ NMR spectra of Bpin/$SiO_{2(700,\ 900)}$ both display strong autocorrelations for ^{1}H SQ NMR signals at *ca.* 1.5 ppm which correspond to the CH_3 methyl signals of Bpin (Figure 3.3B, middle, right). Interestingly, the intensity of the H-bonded silanol autocorrelations (colored pink) and methyl to silanol off-diagonal correlations (colored yellow) are significantly reduced for Bpin/$SiO_{2(700)}$ as compared to Bpin/$SiO_{2(200)}$ and are near absent in Bpin/$SiO_{2(900)}$ (Figure 3.3B), suggesting a reduced number of neighboring silanol species to the grafted Bpin molecule. Comparison of 2D ^{1}H-^{11}B HETCOR spectra of Bpin/$SiO_{2(200,\ 700,\ 900)}$ show identical trends observed in the 2D ^{1}H DQ-SQ spectra, where Bpin/$SiO_{2(700)}$ displays significantly reduced correlations between nearby silanol species and the grafted Bpin molecule whereas these correlations are absent for Bpin/$SiO_{2(900)}$ (Figure 3.3C, orange color). The observed reduction in the number of hydrogen bonded silanol species to the grafted Bpin molecule is consistent with the room temperature ^{11}B NMR and transmission IR spectra discussed above. Therefore, we illustrate that Bpin/$SiO_{2(200)}$ contains multiple silanol species in a hydrogen-bonded nest surrounding the

monopodally grafted Bpin molecule, while the number of nearby silanol species is significantly reduced for Bpin/$SiO_{2(700)}$ and are near absent for Bpin/$SiO_{2(900)}$, meaning Bpin is relatively isolated on the silica surface (Figure 3.3A).

To summarize, pinacolborane (HBpin) grafted in the gas phase onto silica results in selective monopodal anchoring of Bpin to the surface by reaction with an Si-OH group (Figure 3.1, upper). Neighboring unreacted Si-OH groups can form hydrogen-bonding interactions with the grafted molecule, limiting the degree of rotation of Bpin around the B-O-Si bond. The hydrogen-bonding environment around the grafted Bpin molecule depends on the density of surface silanol groups, which can be controlled by the support dehydration temperature (Figure 3.3A).

3.3.2. Formation of active ODH catalysts.

The grafted Bpin/$SiO_{2(T)}$ materials were thermally treated at 20 μbar and 500 °C for 10 hours to remove the organics and generate the active catalysts. The materials after thermal treatment are denoted in the Figures as Bpin/$SiO_{2(T)}$-^{500v}. As a shorthand in the text, the materials will be referred to as S2, S7, and S9, where the number corresponds to the initial support dehydration temperature (*i.e.,* S2 corresponds to an initial support dehydration temperature of 200 °C). The boron weight loadings (determined via ICP-MS) and BET surface areas are 1.65 ± 0.01 % and 246 m^2g^{-1}, 0.81 ± 0.01 % and 271 m^2g^{-1}, and 0.18 ± 0.01 % and 252 m^2g^{-1} for S2, S7, and S9, respectively (Table S2).

Transmission IR spectra of the thermally treated materials do not show aliphatic C-H stretching near 3000 cm^{-1}, indicating complete removal of the Bpin methyl groups (Figure S6). The IR spectra display two sharp features at 3747 and 3704 cm^{-1}, corresponding to SiO-H and BO-H stretching, respectively.[21, 49, 58-59] In addition, all materials show a broad peak extending to *ca.* 3200 cm^{-1} that can be assigned to hydrogen bonded SiO-H and/or BO-H species. As

expected, the intensity of this broad hydrogen bonded hydroxyl signal is reduced with increasing silica thermal treatment temperatures.

We note that the experimentally determined boron weight loadings on S2 and S7 are higher than that calculated based on the initial silanol content, assuming HBpin grafts exclusively to isolated silanol species (Table S2). SiO_2 dehydrated at 700 °C has a silanol density of *ca.* 0.9/nm^2.[49] The stoichiometric reaction of HBpin with isolated SiOH groups would result in a boron weight loading of 0.48 wt %. The discrepancy between the calculated (0.48 wt %) and measured (0.81 wt %) boron loadings can be explained by the reaction of HBpin with the strained siloxane bridges that form at high dehydration temperatures. The reaction between strained siloxane bridges and a precursor has been previously observed when grafting vanadium triisopropoxide to $SiO_{2(700)}$.[28] Indeed, when the silanol groups on $SiO_{2(700)}$ are capped with trimethylsilane (TMS) groups (TMS-$SiO_{2(700)}$), leaving only siloxane bridges as possible anchoring sites (Table S2), HBpin can anchor to the surface as seen by IR spectroscopy (Figure S7), resulting in a boron weight loading of 0.56 ± 0.01 % (Table S2). Silica dehydrated at 200 °C has an isolated SiOH density of 1.2/nm^2 and the surface is additionally populated by hydrogen-bonding silanol nests.[49] Silanol nests are often assumed to be relatively unreactive; however, a recent study of the grafting synthesis of vanadium triisopropoxide on $SiO_{2(200)}$ revealed that the presence of a hydrogen-bond acceptor on the surface can activate H-bonding silanols as additional anchoring sites.[27] Given the formation of new H-bonding interactions upon the grafting of HBpin onto $SiO_{2(200)}$, we propose that a similar activation of H-bonding silanols occurs, increasing the boron content of the sample. Unlike the S2 and S7 materials, the S9 sample does not show a discrepancy between expected and measured boron loadings (Table S2). The agreement between calculated and measured weight loadings on S9 indicates a change in reactivity of siloxane bridges on the $SiO_{2(900)}$ support. This change in reactivity is likely associated with the partial collapse of the SiO_2 framework that occurs above 800 °C, which is supported by a decreased BET surface area determined for S9 compared to S7 (Table S2).[49]

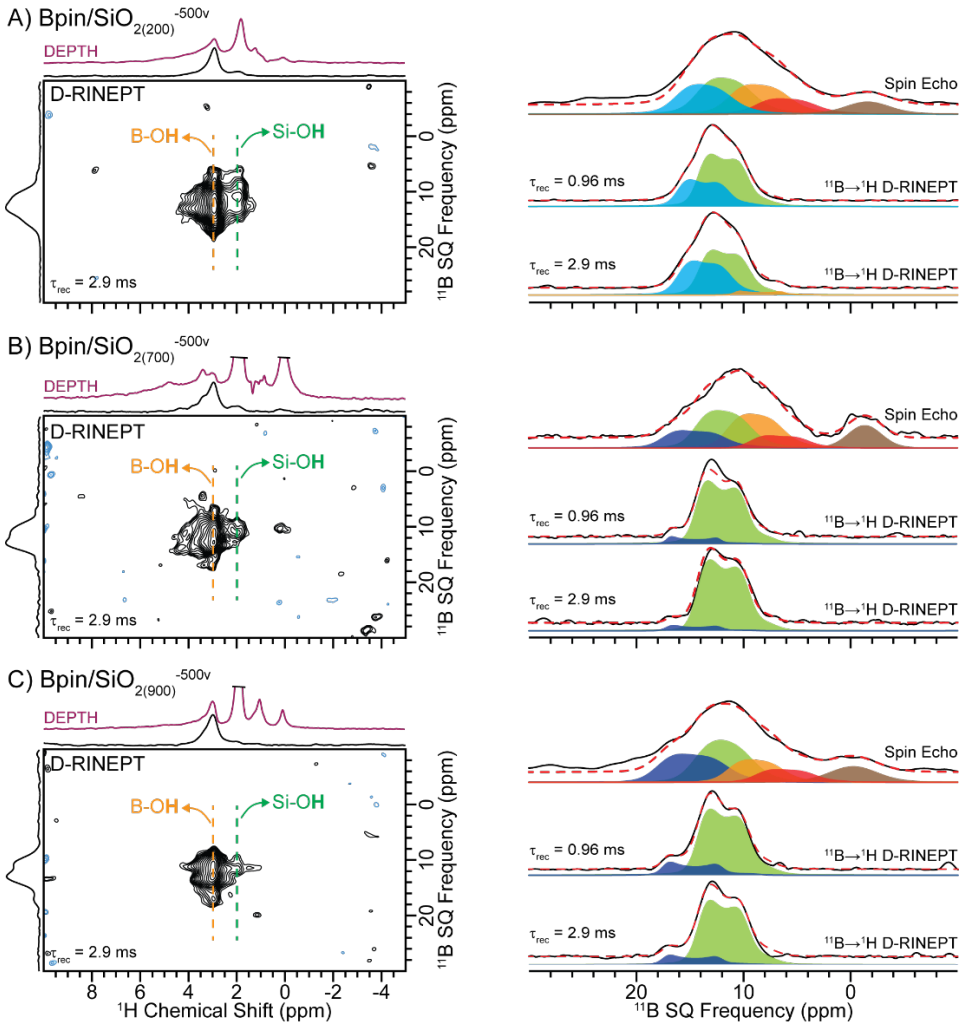

Figure 3.4. (Left) 2D $^{11}B \rightarrow {}^{1}H$ D-RINEPT NMR spectra of the calcined (A) Bpin/$SiO_{2(200)}$, (B) Bpin/$SiO_{2(700)}$ and (C) Bpin/$SiO_{2(900)}$ fresh catalysts. (Right) Comparison of (recycle delay ≥ 5 × T_1) 1D ^{11}B spin echo NMR spectra with ^{11}B projections from the 2D $^{11}B \rightarrow {}^{1}H$ D-RINEPT NMR spectra. The black and red lines correspond to the experimental and analytically simulated spectra, respectively. The exact parameters used to fit the ^{11}B spin echo spectra are given in Table S3. All spectra were recorded at B_0 = 14.1 T with 25 kHz MAS.

1D direct excitation ^{11}B spin echo NMR spectra of S2, S7, and S9 display two main groups of signals centered at *ca.* 0 or 10 ppm, corresponding to 4-coordinate (BO_4) and three-coordinate (BO_3) boron oxide-type species, respectively (Figure 3.4, right column).[15, 21, 50-53] The broad signal centered at *ca.* 10 ppm (BO_3-type species) can be analytically simulated to four unique boron sites with a C_Q between 2.2 and 2.5 MHz and $\delta_{iso}(^{11}B)$ ~ (blue) 17 – 19 ppm, (green) 15 ppm, (orange) 12 ppm, and (red) 10 ppm (Figure 3.4, right column, Table 3.1). The identification of

each site is discussed below. We note that each ^{11}B fit in the analytical simulations have a significant amount of gaussian broadening to represent a distribution in shift/C_Q caused by structural disorder, typical of surface supported boron oxide/hydroxide species.[15] 2D ^{11}B→^{1}H dipolar refocused INEPT (D-RINEPT) HETCOR spectra of S2, S7, and S9 recorded with a short duration of dipolar recoupling (0.96 ms) all display intense ^{1}H NMR signals at *ca.* 3 ppm correlating to ^{11}B NMR signals centered at *ca.* 12 – 14 ppm (Figure S8). The short duration of dipolar recoupling ensures that the ^{1}H and ^{11}B NMR signals arise from boron hydroxide species (B-OH); the ^{1}H NMR signal at *ca.* 3 ppm is assigned to B-OH, similar to that observed in B-MWW and B/SiO_2-IWI.[15, 17, 21] An analytical simulation of the 2D ^{11}B projections reveal that there are two unique boron species containing hydroxyl groups with δ_{iso}(^{11}B) ~ (green fit) 15 ppm or (blue fit) 17 – 19 ppm (Figure 3.4, right column). As the dipolar recoupling duration is increased to 2.9 ms, enabling the observation of H-B spin pairs further away in space, an additional correlation between the same ^{11}B NMR signals and a ^{1}H NMR signal at *ca.* 2 ppm is observed (Figure 3.4, left column). The ^{1}H NMR signal at *ca.* 2 ppm is assigned to a nearby isolated (*i.e.*, not hydrogen bonded) silanol (Si-OH) group (Figure 3.5, S9).[51, 57, 60]

The 2D ^{1}H-^{11}B HETCOR spectra identified B-OH containing boron species and revealed that they are in close-spatial proximity to isolated silanol groups. It is well known that δ_{iso}(^{11}B) decreases as B-O-B groups are replaced with B-O-Si; $B(OB)_3$ and $B(OSi)_3$ on silica/zeolites typically resonance at *ca.* 17 and 10 ppm, respectively.[15, 50-51, 61-64] Therefore, based on the high δ_{iso}(^{11}B) and strong ^{1}H-^{11}B HETCOR correlations observed with a short duration of recoupling, we assign the ^{11}B NMR signals at δ_{iso}(^{11}B) ~ 17 – 19 ppm to $B(OB)_x(OH)_{3-x}$ (x = 1 – 2) exhibiting at least one B-O-B and B-O-H bond (Table 1). The ^{11}B NMR signal at δ_{iso}(^{11}B) ~ 15 ppm also displays strong ^{1}H-^{11}B heteronuclear correlations and thus contains a B-OH bond. However, the decrease in shift is likely a result of replacing a B-O-B group with B-O-Si, suggesting this species corresponds to $B(OB)_x(OH)_{2-x}(OSi)$ (x = 0 – 1) (Table 1). The ^{11}B NMR signals at ~ 10 and 12 ppm

observed in the direct excitation experiment were not observed in the ^{1}H-^{11}B HETCOR spectra and thus do not contain a hydroxyl group. Based on well-established literature and the low observed $\delta_{iso}(^{11}B)$, the ^{11}B NMR signals at $\delta_{iso}(^{11}B)$ ~ 12 and 10 ppm correspond to $B(OB)(OSi)_2$ and $B(OSi)_3$ species, respectively (Table 1).[15, 50-51, 61-64] 1D ^{11}B dipolar DQ-SQ NMR spectra of S2 and S7 resemble that of 1D direct excitation ^{11}B NMR spectra, corroborating our NMR assignments and illustrating that the majority of 3-coordinate boron is clustered on the silica surface (Figure S10). It should be noted that we were unsuccessful in recording a ^{11}B DQ-SQ spectrum of S9, however, this is attributed to low sensitivity associated with the DQ-SQ experiment and low B weight loading (~ 0.18 wt %) on the silica surface. Lastly, no 4-coordinate BO_4 species were observed in the ^{1}H-^{11}B HETOR spectra, revealing that BO_4 is not proximate to ^{1}H spins. The BO_4 species are likely charge balanced by ion impurities in the silica, such as Na^+,[24, 65] which has been previously reported for borosilicate zeolites.[51] Therefore, we hypothesize that BO_4 is likely incorporated into the silica framework, taking the formula $B(OSi)_4$ (Table 3.1).

Table 3.2. Structure of boron species, NMR parameters, and percent population for each $Bpin/SiO_{2(T)}$-^{500v} material.

Species[a]	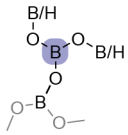	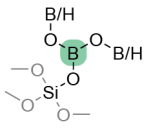	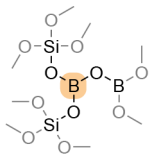	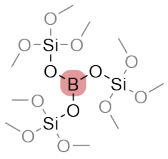	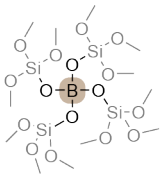
	$B(OB)(OB/H)_2$	$B(OB/H)_2(OSi)$	$B(OB)(OSi)_2$	$B(OSi)_3$	$B(OSi)_4$
δ_{iso} (ppm)	~17-19	~15	~12	~10	~0
C_Q (MHz)	2.4-2.5	2.2	2.2	2.3	0.5
	Percent Population (%)				
$Bpin/SiO_{2(200)}$-^{500v}	24	29	25	13	9
$Bpin/SiO_{2(700)}$-^{500v}	17	32	29	10	12
$Bpin/SiO_{2(900)}$-^{500v}	27	33	18	10	12

[a]Species with "OB/H" means it is either an O-B or O-H functional group.

The analytical simulations of the 1D ^{11}B NMR spectra (recycle delay > $5 \times T_1$) suggest that the relative populations of each type of boron species is similar between all catalysts, with minor differences that are likely within error of the simulations (Table 3.1). However, comparison of ^{1}H NMR spectra reveal significant differences between the catalysts (Figure 3.5). A ^{1}H DQ-SQ NMR spectrum of S2 displays an intense, broad signal centered at *ca.* 4 ppm which is assigned to hydrogen-bonded Si-OH species (Figure 3.5 and S11). Alternatively, this broad NMR signal at 4 ppm is nearly absent in the ^{1}H DQ-SQ NMR spectrum of S7 and is completely absent in the ^{1}H DQ-SQ NMR spectrum of S9, revealing that the hydrogen bonding network in the active catalysts is significantly reduced with increased SiO_2 thermal pre-treatment temperatures (Figure 3.5 and S11). The observation of decreased hydrogen bonding with increased SiO_2 thermal treatment is consistent with that observed in the transmission IR spectra discussed above (Figure S6). Closer inspection of the ^{11}B→^{1}H D-RINEPT NMR spectra of S2, S7, and S9 shows there are two unique B-OH ^{1}H chemical shifts at *ca.* 3.0 and 3.4 ppm. Interestingly, only the B-OH ^{1}H NMR signal at *ca.* 3.4 ppm is observed in the ^{1}H DQ-SQ spectra of S7 and S9 and displays autocorrelations, showing that the B-OH ^{1}H NMR signal at *ca.* 3.4 ppm is proximate to another B-OH species while the B-OH ^{1}H NMR signal at *ca.* 3.0 ppm is relatively isolated (within ~ 5 Å distance) from other hydrogen atoms (Figure S11). We note there are two additional ^{1}H NMR signals at *ca.* 0 and 1 ppm that come through the DQ-filter that did not reveal correlations to ^{11}B (Figure 3.4, 3.5, S8 and S11). The ^{1}H NMR signal at *ca.* 1 ppm has been previously assigned to water-inaccessible or internal non-hydrogen bonded Si-OH species that likely reside inside the silica rather than near or on the surface;[66-69] the Si-OH ^{1}H NMR signal at *ca.* 2 ppm is likely near or on the surface as it correlated to the surface boron oxide/hydroxide ^{11}B NMR signals (Figure 3.4, left column). Therefore, we assign the ^{1}H NMR signal at *ca.* 1 ppm to internal non-hydrogen bonded Si-OH species. The ^{1}H NMR signal at *ca.* 0 ppm is preliminarily assigned to silicone vacuum grease impurities that immobilized on the silica surface during the thermal treatment of Bpin/$SiO_{2(T)}$. We

note that the 0 ppm ^{1}H NMR signal was also observed in the as-grafted materials, further suggesting assignment to silicone vacuum grease (Figure S5).

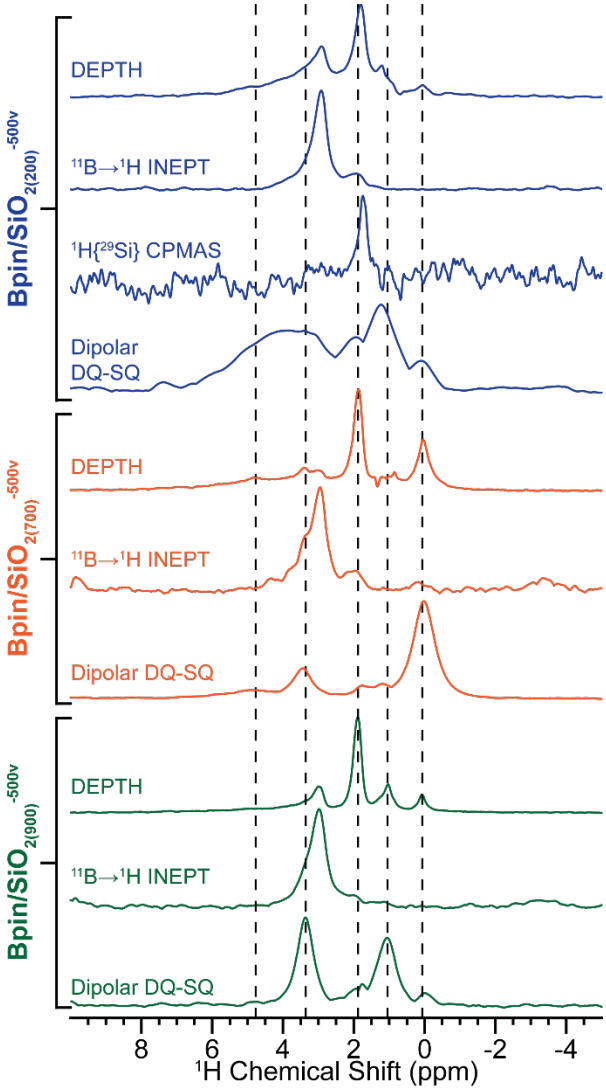

Figure 5. Comparison of 1D direct excitation (DEPTH) ^{1}H, ^{11}B→^{1}H D-RINEPT, ^{1}H{^{29}Si} CPMAS and ^{1}H DQ-SQ spectra for (upper, blue) Bpin/SiO$_{2(200)}$-^{500v}, (middle, orange) Bpin/SiO$_{2(700)}$-^{500v} and (lower, green) Bpin/SiO$_{2(900)}$-^{500v}. The exact experiment is given above each spectrum. All spectra were recorded at B_0 = 14.1 T with 25 kHz MAS.

In summary, ^{11}B solid-state NMR spectroscopy revealed that the boron speciation after thermal treatment is not dependent on the initial silanol density or the boron weight loading. The grafted materials, Bpin/SiO$_{2(T)}$, contained monopodally grafted molecular boron and the number

of neighboring hydrogen bonded silanol groups was controlled by the temperature of SiO_2 thermal pretreatment, where Bpin/$SiO_{2(900)}$ exhibited little to no hydrogen-bonded silanol species. Therefore, the observation of similar boron species for all catalysts illustrates that boron oxide/hydroxide can move around on the surface of SiO_2 under the thermal treatment conditions to form an agglomerated boron oxide/hydroxide phase regardless of boron weight loading and surface hydrogen bonding networks. The boron speciation and the presence of a large proportion of silanol groups suggests the formation of small boron clusters or particles rather than an even monolayer on the support surface. ^{1}H solid-state NMR and FTIR spectroscopies suggest that the main difference between the different catalyst materials is the hydrogen bonding network on the surface of silica, where increased silica pretreatment temperatures lead to decreased surface hydrogen bonding networks, as expected. Future studies should evaluate the effect of thermal treatment conditions on the boron speciation.

3.3.3. Evaluating catalytic activity and changes in boron structure.

Propane ODH experiments were performed in a fixed bed quartz reactor at 500 °C under a mixture of C_3H_8, O_2, and N_2 in a 6:3:11 molar ratio. The conversion stabilized over 24 hours (Figure 3.6A), after which the gas flow rates were changed to acquire the conversion-selectivity trends shown in Figure 3.6B. As is seen in Figure 3.6A, each material undergoes an induction period before reaching steady-state conversion. For each catalyst, steady-state conversion is *ca.* 2 %

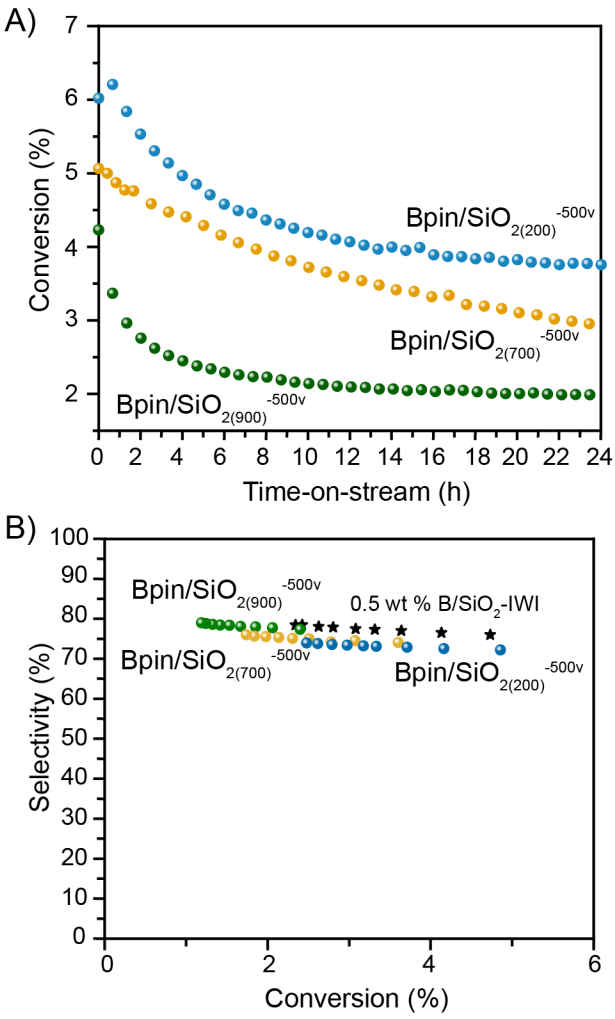

Figure 3.6. (A) Conversion as a function of time-on-stream and (B) Propylene selectivity as a function of propane conversion. Different conversions were achieved by changing the gas flow rate between 40 and 200 mL min^{-1}.

lower than the initial conversion. We presume that some boron is removed from the surface during this induction period as the surface likely restructures under reaction conditions. Elemental analysis of the catalysts after reaction showed that the boron weight loading of S2 and S7 decreased from 1.65 to 0.33 wt.% and 0.81 to 0.32 wt.%, respectively (Table S2). The weight loading of the spent S9 sample could not be reliably determined, likely because of very low boron content (0.18 wt. % initial B loading). The conversion-selectivity trends in Figure 3.6B are typical of other B/SiO_2 catalysts in the literature.[16, 19, 21] There are slight differences in the conversion-

selectivity trends between the materials which might be correlated with the amount of unselective silanol groups exposed on the surface.

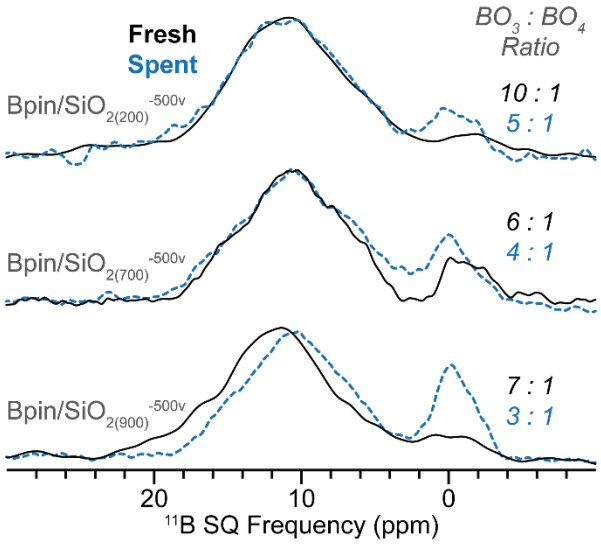

Figure 3.7. Comparison of relatively quantitative (recycle delay ≥ 5 × T_1) 1D ^{11}B spin echo NMR spectra of the B/spin/$SiO_{2(T)}$-^{500v} materials (black, solid) before and (blue, dashed) after catalysis.

^{11}B solid-state NMR spectroscopy analysis of the catalysts after reaction do not show a drastic change in boron speciation (Figure 3.7). For each material, the ^{11}B NMR spectra for the spent catalysts (dashed blue lines) display similar 3-coordinate ^{11}B NMR signals as the fresh catalysts (solid black lines). Notably, there is an increase in the relative amount of BO_4 species in each sample. Based on the decrease in boron weight loading for S2 and S7 mentioned above, the relative increase in BO_4 is most likely due to leaching of surface BO_3 species; however, we cannot rule out the possibility of forming new $B(OSi)_4$ species under reaction conditions. There is also a clear loss of the boron-rich clusters that show up at the high frequency edge of the ^{11}B NMR spectrum of the S9 material. This loss of boron-rich clusters is consistent with our previous observation that boroxol ring-type species are lost from B/SiO_2-IWI after catalysis.[15, 21] Notably, the shape of the ^{11}B NMR spectra for all spent catalysts are near identical, revealing that similar ODH active boron oxide/hydroxide clusters are present for all materials regardless of the initial

silica thermal dehydration temperature (Figure S12). This further suggests that boron oxide/hydroxide is highly mobile on the silica surface under reaction conditions.

2D $^{11}B \rightarrow {}^{1}H$ D-RINEPT spectra of the spent materials are also very similar to that of the fresh catalysts, with some minor differences in the ^{11}B projections likely due to the partial leaching of boron rich clusters containing hydroxyl groups (Figure S13 and S14). It should be mentioned that the 2D $^{11}B \rightarrow {}^{1}H$ D-RINEPT spectra of the spent catalysts required significantly longer experimental times which is consistent with a decrease in boron loading after reaction and the partial removal of boron hydroxide species (Table S1).[15] Interestingly, ^{1}H dipolar DQ-SQ spectra of fresh S7 and S9 are significantly different than the spent materials (Figure S15). All spent catalysts reveal an intense, broad feature center at *ca.* 4-5 ppm in the ^{1}H DQ-SQ spectra which is assigned to hydrogen-bonded surface silanol species. This broad hydrogen-bonded surface silanol species was present in fresh S2 but was near absent in fresh S7 and completely absent in fresh S9 (Figure 3.5 and S15). The observation of surface hydrogen-bonding silanol species after catalysis for S7 and S9 further confirms the restructuring and partial leaching of boron oxide/hydroxide clusters under reaction conditions.

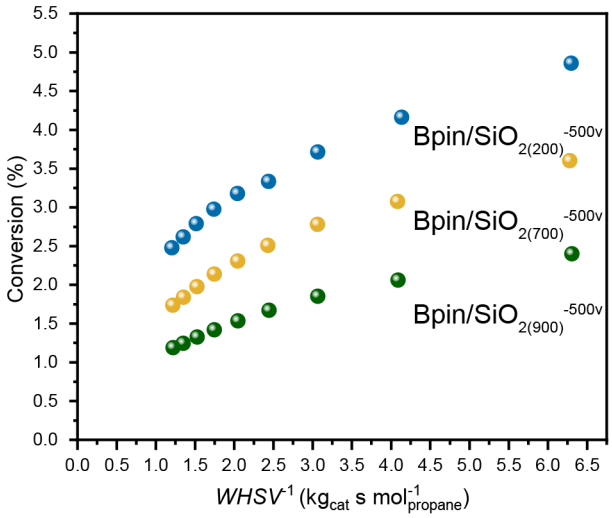

Figure 3.8. Propane conversion as a function of inverse weight hourly space velocity for all $Bpin/SiO_{2(T)}^{-500v}$ materials.

Although these materials do not allow us to probe the effect of initial boron agglomeration, we can probe the effect of boron weight loading on catalyst activity, uncomplicated by differences in initial boron speciation. We emphasize that we do not attempt to ascribe the catalytic activity to any one boron species. Rather, we seek to understand activity based on the overall structure and composition of the catalyst surface. Because the boron oxide/hydroxide phase is dynamic under reaction conditions, the accessible structures under such conditions are likely distinct from those observed at room temperature using *ex situ* characterization, where the most thermodynamically favorable phases are detected.

Figure 3.8 shows the propane conversion as a function of inverse weight-hourly-space-velocity (*i.e.*, the contact time between the gas and the surface) for each catalyst. As expected, when weight loading increases, the conversion at a given contact time increases. Often, such a plot is fit with a linear line to determine the initial reaction rate. However, for all three materials, the conversion begins to level off at higher contact times. This is unlike the behavior of the bulk boron-based materials, which show a linear increase of conversion as the contact time increases.[2] This difference suggests that the observed catalytic results do not have a straightforward interpretation and are likely complicated by the gas phase chemistry that occurs during the reaction.

The propylene productivity normalized per mole of boron is shown in Figure S16. The S9 material is the most productive per mole B, followed by S7, then S2. This trend is consistent with the formation of different sized particles on the surface of the materials. The particles on S9 are smaller than those on the higher weight loading S2 material, so more boron atoms are at the surface of the particles on S9 and are able to participate in the reaction. For each material, the normalized productivity decreases as the conversion and contact time increase. To understand this behavior, we must put these results into context with our hypothesized mechanism and the role the surface plays within that mechanism.

Scheme 3.1. Simplified proposed reaction network showing only reactions involving BO•. The square denotes the active site.

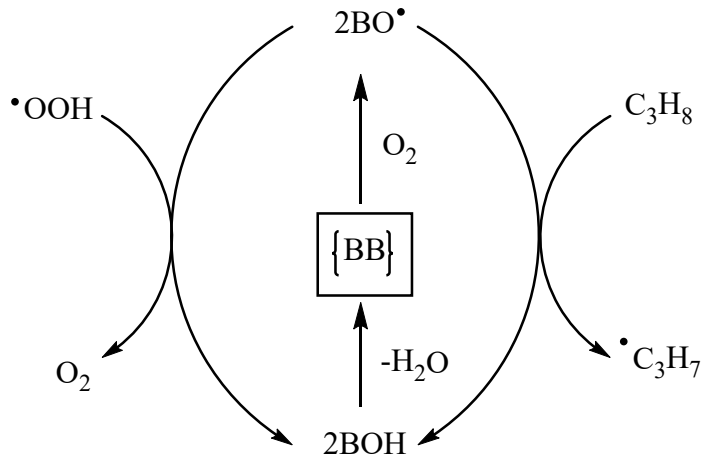

The proposed mechanism proceeds via a radical pathway.[9-10, 18] The main role of the surface is to initiate the reaction by generating radical species.[9] Under reaction conditions, the surface generates unsaturated {BB} units that can activate O_2 to form 2BO• species. As can be seen in the simplified reaction network in Scheme 1, any reaction with BO• is a termination reaction that generates B-OH groups. B-OH groups are not readily reactive and must be dehydrated to regenerate active {BB} sites. The calculated barrier for this regeneration step is 222 kJ/mol,[10] in line with experimentally reported apparent activation energies of 200-250 kJ/mol for hBN-catalyzed ODH.[3, 10] Based on the closeness of the calculated barrier and experimental activation energies, we have hypothesized that active site regeneration is the rate-limiting reaction step in the overall mechanism. We emphasize that the hypothesized BO• surface species would only form under reaction conditions and that such a species would not be detected using *ex situ* characterization techniques.

While more systematic kinetic studies are needed to better understand the behavior of these supported materials, the proposed mechanism offers a possible explanation for the observed loss of activity at higher conversions. As the gas moves more slowly through the catalyst bed, more active sites are consumed. The consumption of the active sites leads to the eventual

formation of unreactive B-OH groups that must be regenerated. If active site regeneration is indeed rate limiting, perhaps the loss of productivity per mole B occurs because at high conversions, the reaction becomes limited, as there is a fixed amount of boron available in a given cluster or particle on SiO_2, and the surface can eventually become saturated in B-OH groups, decreasing the active site concentration and the rate of initiation. Such saturation-like behavior does not occur with bulk materials where boron is abundant. A more thorough exploration of the reaction kinetics over these materials is ongoing in our lab.

3.4 Conclusion

A combination of transmission FTIR and solid-state NMR spectroscopies revealed that the grafting of HBpin onto SiO_2 generates isolated, monopodally grafted Bpin (B-O-Si bond to the silica surface) that can form hydrogen bonds with nearby unreacted silanol groups. The number of neighboring hydrogen-bonded silanol species can be decreased with increased silica thermal treatment temperature, enabling high controllability of the local chemical environment surrounding the isolated, singly anchored Bpin molecule. However, the control over surface speciation is lost during the thermal treatment of Bpin/$SiO_{2(T)}$ materials, as a similar boron oxide/hydroxide phase is observed for all catalysts. The observation of similar boron species, especially for S9, which contained ~ 0.18 wt. % B and exhibited highly isolated grafted Bpin before thermal treatment, illustrates that boron oxide/hydroxide is highly mobile on the SiO_2 surface and is able to generate clustered boron oxide/hydroxide under thermal treatment conditions. Modification of thermal treatment conditions, chemically treating the surface before or after grafting, and/or doping the silica surface could potentially enable better control over the species formed on the silica surface by reducing boron oxide/hydroxide mobility.

The catalytic activity of Bpin/$SiO_{2(T)}^{-500v}$ materials is typical for silica-supported boron oxide catalysts previously reported.[19, 21] Because these materials of different boron weight loadings

contained similar boron speciation, we were able to probe the effect of boron content on catalytic activity. We observed the highest propylene productivity per mole of boron in the S9 material, consistent with the presence of boron oxide/hydroxide particles. Additionally, we observed the loss of productivity at increased conversions for all catalysts. More thorough kinetic studies are needed to understand this observation in terms of the proposed reaction mechanism.

3.5 References

(1) Grant, J. T.; Carrero, C. A.; Goeltl, F.; Venegas, J.; Mueller, P.; Burt, S. P.; Specht, S. E.; McDermott, W. P.; Chieregato, A.; Hermans, I., Selective Oxidative Dehydrogenation of Propane to Propene Using Boron Nitride Catalysts. *Science* 2016, *354* (6319), 1570-1573. 10.1126/science.aaf7885.

(2) Grant, J. T.; McDermott, W. P.; Venegas, J. M.; Burt, S. P.; Micka, J.; Phivilay, S. P.; Carrero, C. A.; Hermans, I., Boron and Boron-Containing Catalysts for the Oxidative Dehydrogenation of Propane. *ChemCatChem* 2017, *9* (19), 3623-3626. 10.1002/cctc.201701140.

(3) Venegas, J. M.; Grant, J. T.; McDermott, W. P.; Burt, S. P.; Micka, J.; Carrero, C. A.; Hermans, I., Selective Oxidation of N-Butane and Isobutane Catalyzed by Boron Nitride. *ChemCatChem* 2017, *9* (12), 2118-2127. 10.1002/cctc.201601686.

(4) Huang, R.; Zhang, B.; Wang, J.; Wu, K.-H.; Shi, W.; Zhang, Y.; Liu, Y.; Zheng, A.; Schlögl, R.; Su, D. S., Direct Insight into Ethane Oxidative Dehydrogenation over Boron Nitrides. *ChemCatChem* 2017, *9* (17), 3293-3297. doi:10.1002/cctc.201700725.

(5) Lei Shi, B. Y., Dan Shao, Fan Jiang, Dongqi Wang, An-Hui Lu, Selective Oxidative Dehydrogenation of Ethane to Ethylene over a Hydroxylated Boron Nitride Catalyst. *Chinese J Catal* 2017, *38* (2), 389-395. 10.1016/s1872-2067(17)62786-4.

(6) Shi, L.; Wang, D.; Song, W.; Shao, D.; Zhang, W.-P.; Lu, A.-H., Edge-Hydroxylated Boron Nitride for Oxidative Dehydrogenation of Propane to Propylene. *ChemCatChem* 2017, *9* (10), 1788-1793. doi:10.1002/cctc.201700004.

(7) Cavani, F.; Ballarini, N.; Cericola, A., Oxidative Dehydrogenation of Ethane and Propane: How Far from Commercial Implementation? *Catal. Today* 2007, *127* (1), 113-131. https://doi.org/10.1016/j.cattod.2007.05.009.

(8) Ren, T.; Patel, M.; Blok, K., Olefins from Conventional and Heavy Feedstocks: Energy Use in Steam Cracking and Alternative Processes. *Energy* 2006, *31* (4), 425-451. https://doi.org/10.1016/j.energy.2005.04.001.

(9) Zhang, X.; You, R.; Wei, Z.; Jiang, X.; Yang, J.; Pan, Y.; Wu, P.; Jia, Q.; Bao, Z.; Bai, L., et al., Radical Chemistry and Reaction Mechanisms of Propane Oxidative Dehydrogenation over Hexagonal Boron Nitride Catalysts. *Angew. Chem., Int. Ed.* 2020, *59* (21), 8042-8046. 10.1002/anie.202002440.

(10) Venegas, J. M.; Zhang, Z.; Agbi, T. O.; McDermott, W. P.; Alexandrova, A.; Hermans, I., Why Boron Nitride Is Such a Selective Catalyst for the Oxidative Dehydrogenation of Propane. *Angew. Chem. Int.l Ed.* 2020, *59* (38), 16527-16535. 10.1002/anie.202003695.

(11) Si, C.; Lian, Z.; Olanrele, S. O.; Sun, X.; Li, B., Revealing the Origin of the Reactivity of Metal-Free Boron Nitride Catalysts in Oxidative Dehydrogenation of Propane. *Appl. Surf. Sci.* 2020, *519*, 146241. https://doi.org/10.1016/j.apsusc.2020.146241.

(12) Rajbanshi, B.; Saha, S.; Fricke, C.; Ammal, S. C.; Heyden, A., Oxidative Dehydrogenation of Propane on the Oxygen Adsorbed Edges of Boron Nitride Nanoribbons. *Cat. Sci. Tech.* 2020, *10* (15), 5181-5195. 10.1039/D0CY01031F.

(13) Qiu, B.; Jiang, F.; Lu, W.-D.; Yan, B.; Li, W.-C.; Zhao, Z.-C.; Lu, A.-H., Oxidative Dehydrogenation of Propane Using Layered Borosilicate Zeolite as the Active and Selective Catalyst. *J. Catal.* 2020, *385*, 176-182. https://doi.org/10.1016/j.jcat.2020.03.021.

(14) McDermott, W. P.; Venegas, J.; Hermans, I., Selective Oxidative Cracking of N-Butane to Light Olefins over Hexagonal Boron Nitride with Limited Formation of Cox. *ChemSusChem* 2020, *13* (1), 152-158. 10.1002/cssc.201901663.

(15) Dorn, R. W.; Cendejas, M. C.; Chen, K.; Hung, I.; Altvater, N. R.; McDermott, W. P.; Gan, Z.; Hermans, I.; Rossini, A. J., Structure Determination of Boron-Based Oxidative Dehydrogenation Heterogeneous Catalysts with Ultrahigh Field 35.2 T 11B Solid-State NMR Spectroscopy. *ACS Catal.* 2020, *10* (23), 13852-13866. 10.1021/acscatal.0c03762.

(16) Belgamwar, R.; Rankin, A. G. M.; Maity, A.; Mishra, A. K.; Gomez, J. S.; Trebosc, J.; Vinod, C. P.; Lafon, O.; Polshettiwar, V., Boron Nitride and Oxide Supported on Dendritic Fibrous Nanosilica for Catalytic Oxidative Dehydrogenation of Propane. *ACS Sus. Chem. Eng.* 2020, *8* (43), 16124-16135. 10.1021/acssuschemeng.0c04148.

(17) Altvater, N. R.; Dorn, R. W.; Cendejas, M. C.; McDermott, W. P.; Thomas, B.; Rossini, A. J.; Hermans, I., B-MWW Zeolite: The Case against Single-Site Catalysis. *Angew. Chem. Int. Ed.* 2020, *59* (16), 6546-6550. 10.1002/anie.201914696.

(18) Venegas, J. M.; Hermans, I., The Influence of Reactor Parameters on the Boron Nitride-Catalyzed Oxidative Dehydrogenation of Propane. *Org. Process Res. & Dev.* 2018, *22* (12), 1644-1652. 10.1021/acs.oprd.8b00301.

(19) Lu, W.-D.; Wang, D.; Zhao, Z.; Song, W.; Li, W.-C.; Lu, A.-H., Supported Boron Oxide Catalysts for Selective and Low-Temperature Oxidative Dehydrogenation of Propane. *ACS Catal.* 2019, *9* (9), 8263-8270. 10.1021/acscatal.9b02284.

(20) Love, A. M.; Thomas, B.; Specht, S. E.; Hanrahan, M. P.; Venegas, J. M.; Burt, S. P.; Grant, J. T.; Cendejas, M. C.; McDermott, W. P.; Rossini, A. J., et al., Probing the Transformation of Boron Nitride Catalysts under Oxidative Dehydrogenation Conditions. *J. Am. Chem. Soc.* 2019, *141* (1), 182-190. 10.1021/jacs.8b08165.

(21) Love, A. M.; Cendejas, M. C.; Thomas, B.; McDermott, W. P.; Uchupalanun, P.; Kruszynski, C.; Burt, S. P.; Agbi, T.; Rossini, A. J.; Hermans, I., Synthesis and Characterization of Silica-Supported Boron Oxide Catalysts for the Oxidative Dehydrogenation of Propane. *J. Phys. Chem. C* 2019, *123* (44), 27000-27011. 10.1021/acs.jpcc.9b07429.

(22) Zhang, Z.; Jimenez-Izal, E.; Hermans, I.; Alexandrova, A. N., Dynamic Phase Diagram of Catalytic Surface of Hexagonal Boron Nitride under Conditions of Oxidative Dehydrogenation of Propane. *J, Phys. Chem. Let.* 2019, *10* (1), 20-25. 10.1021/acs.jpclett.8b03373.

(23) Carrero, C. A.; Burt, S. P.; Huang, F.; Venegas, J. M.; Love, A. M.; Mueller, P.; Zhu, H.; Grant, J. T.; Mathison, R.; Hanraham, M. P., et al., Supported Two- and Three-Dimensional Vanadium Oxide Species on the Surface of B-Sic. *Cat. Sci. Tech.* 2017, *7* (17), 3707-3714. 10.1039/C7CY01036B.

(24) Grant, J. T.; Carrero, C. A.; Love, A. M.; Verel, R.; Hermans, I., Enhanced Two-Dimensional Dispersion of Group V Metal Oxides on Silica. *ACS Catal.* 2015, *5* (10), 5787-5793. 10.1021/acscatal.5b01679.

(25) Williams, L. A.; Marks, T. J., Synthesis, Characterization, and Heterogeneous Catalytic Implementation of Sulfated Alumina Nanoparticles. Arene Hydrogenation and Olefin Polymerization Properties of Supported Organozirconium Complexes. *ACS Catal.* 2011, *1* (4), 238-245. 10.1021/cs100119w.

(26) Chabanas, M.; Vidal, V.; Copéret, C.; Thivolle-Cazat, J.; Basset, J.-M., Low-Temperature Hydrogenolysis of Alkanes Catalyzed by a Silica-Supported Tantalum Hydride Complex, and Evidence for a Mechanistic Switch from Group IV to Group V Metal Surface Hydride Complexes. *Angew. Chem. Int. Ed.* 2000, *39* (11), 1962-1965. https://doi.org/10.1002/1521-3773(20000602)39:11<1962::AID-ANIE1962>3.0.CO;2-1.

(27) Love, A. M.; Cendejas, M. C.; Hanrahan, M. P.; Carnahan, S. L.; Uchupalanun, P.; Rossini, A. J.; Hermans, I., Understanding the Synthesis of Supported Vanadium Oxide Catalysts Using Chemical Grafting. *Chem.Eur. J.* 2020, *26* (5), 1052-1063. 10.1002/chem.201904260.

(28) Love, A. M.; Carrero, C. A.; Chieregato, A.; Grant, J. T.; Conrad, S.; Verel, R.; Hermans, I., Elucidation of Anchoring and Restructuring Steps During Synthesis of Silica-Supported Vanadium Oxide Catalysts. *Chem. Mater.* 2016, *28* (15), 5495-5504. 10.1021/acs.chemmater.6b02118.

(29) Copéret, C., Single-Sites and Nanoparticles at Tailored Interfaces Prepared Via Surface Organometallic Chemistry from Thermolytic Molecular Precursors. *Acc. Chem. Res.* 2019, *52* (6), 1697-1708. 10.1021/acs.accounts.9b00138.

(30) Fujdala, K. L.; Brutchey, R. L.; Tilley, T. D., Tailored Oxide Materials Via Thermolytic Molecular Precursor (TMP) Methods. In *Surface and Interfacial Organometallic Chemistry and Catalysis*, Copéret, C.; Chaudret, B., Eds. Springer Berlin Heidelberg: Berlin, Heidelberg, 2005; pp 69-115.

(31) Harris, R. K.; Becker, E. D.; Cabral de Menezes, S. M.; Goodfellow, R.; Granger, P., NMR Nomenclature: Nuclear Spin Properties and Conventions for Chemical Shifts: Iupac Recommendations 2001. *Solid State Nuc. Magn. Res.* 2002, *22* (4), 458-483. https://doi.org/10.1006/snmr.2002.0063.

(32) Mali, G.; Fink, G.; Taulelle, F., Double-Quantum Homonuclear Correlation Magic Angle Sample Spinning Nuclear Magnetic Resonance Spectroscopy of Dipolar-Coupled Quadrupolar Nuclei. *J. Chem. Phys.* 2004, *120* (6), 2835-2845. 10.1063/1.1638741.

(33) Edén, M.; Zhou, D.; Yu, J., Improved Double-Quantum NMR Correlation Spectroscopy of Dipolar-Coupled Quadrupolar Spins. *Chem. Phys. Lett.* 2006, *431* (4), 397-403. https://doi.org/10.1016/j.cplett.2006.09.081.

(34) Yao, Z.; Kwak, H.-T.; Sakellariou, D.; Emsley, L.; Grandinetti, P. J., Sensitivity Enhancement of the Central Transition NMR Signal of Quadrupolar Nuclei under Magic-Angle Spinning. *Chem. Phys. Lett.* 2000, *327* (1), 85-90. https://doi.org/10.1016/S0009-2614(00)00805-8.

(35) Kwak, H.-T.; Prasad, S.; Clark, T.; Grandinetti, P. J., Enhancing Sensitivity of Quadrupolar Nuclei in Solid-State NMR with Multiple Rotor Assisted Population Transfers. *Solid State Nuc. Magn. Res.* 2003, *24* (2), 71-77. https://doi.org/10.1016/S0926-2040(03)00051-1.

(36) Wang, Q.; Li, Y.; Trébosc, J.; Lafon, O.; Xu, J.; Hu, B.; Feng, N.; Chen, Q.; Amoureux, J.-P.; Deng, F., Population Transfer HMQC for Half-Integer Quadrupolar Nuclei. *J. Chem. Phys.* 2015, *142* (9), 094201. 10.1063/1.4913683.

(37) Fung, B. M.; Khitrin, A. K.; Ermolaev, K., An Improved Broadband Decoupling Sequence for Liquid Crystals and Solids. *J. Magn.. Reson.* 2000, *142* (1), 97-101. https://doi.org/10.1006/jmre.1999.1896.

(38) Feike, M.; Demco, D. E.; Graf, R.; Gottwald, J.; Hafner, S.; Spiess, H. W., Broadband Multiple-Quantum NMR Spectroscopy. *J Magn. Reson. A* 1996, *122* (2), 214-221. https://doi.org/10.1006/jmra.1996.0197.

(39) Schnell, I.; Lupulescu, A.; Hafner, S.; Demco, D. E.; Spiess, H. W., Resolution Enhancement in Multiple-Quantum MAS NMR Spectroscopy. *J. Magn. Reson.* 1998, *133* (1), 61-69. https://doi.org/10.1006/jmre.1998.1432.

(40) Trebosc, J.; Hu, B.; Amoureux, J. P.; Gan, Z., Through-Space R3-Hetcor Experiments between Spin-1/2 and Half-Integer Quadrupolar Nuclei in Solid-State NMR. *J. Magn. Reson.* 2007, *186* (2), 220-227. https://doi.org/10.1016/j.jmr.2007.02.015.

(41) Venkatesh, A.; Hanrahan, M. P.; Rossini, A. J., Proton Detection of Mas Solid-State NMR Spectra of Half-Integer Quadrupolar Nuclei. *Solid State Nuc. Magn. Res.* 2017, *84*, 171-181. https://doi.org/10.1016/j.ssnmr.2017.03.005.

(42) Venkatesh, A.; Luan, X.; Perras, F. A.; Hung, I.; Huang, W.; Rossini, A. J., T 1-Noise Eliminated Dipolar Heteronuclear Multiple-Quantum Coherence Solid-State NMR Spectroscopy. *Phys. Chem. Chem. Phys.* 2020, *22* (36), 20815-20828. 10.1039/D0CP03511D.

(43) Brinkmann, A.; Kentgens, A. P. M., Proton-Selective 17o−H Distance Measurements in Fast Magic-Angle-Spinning Solid-State NMR Spectroscopy for the Determination of Hydrogen Bond Lengths. *J. Am. Chem. Soc.* 2006, *128* (46), 14758-14759. 10.1021/ja065415k.

(44) Venkatesh, A.; Ryan, M. J.; Biswas, A.; Boteju, K. C.; Sadow, A. D.; Rossini, A. J., Enhancing the Sensitivity of Solid-State NMR Experiments with Very Low Gyromagnetic Ratio

Nuclei with Fast Magic Angle Spinning and Proton Detection. *J. Phys. Chem. A* 2018, *122* (25), 5635-5643. 10.1021/acs.jpca.8b05107.

(45) Ishii, Y.; Tycko, R., Sensitivity Enhancement in Solid State ^{15}N NMR by Indirect Detection with High-Speed Magic Angle Spinning. *J. Magn. Reson.* 2000, *142* (1), 199-204. https://doi.org/10.1006/jmre.1999.1976.

(46) Mathey, L.; Alphazan, T.; Valla, M.; Veyre, L.; Fontaine, H.; Enyedi, V.; Yckache, K.; Danielou, M.; Kerdiles, S.; Guerrero, J., et al., Functionalization of Silica Nanoparticles and Native Silicon Oxide with Tailored Boron-Molecular Precursors for Efficient and Predictive P-Doping of Silicon. *J. Phys. Chem. C* 2015, *119* (24), 13750-13757. 10.1021/acs.jpcc.5b03408.

(47) Agarwala, A.; Subramani, T.; Goldbourt, A.; Danovich, D.; Yerushalmi, R., Facile Monolayer Formation on Sio2 Surfaces Via Organoboron Functionalities. *Angew. Chem. Int. Ed.* 2013, *52* (29), 7415-7418. 10.1002/anie.201302655.

(48) Rascón, F.; Wischert, R.; Copéret, C., Molecular Nature of Support Effects in Single-Site Heterogeneous Catalysts: Silicavs.Alumina. *Chem. Sci.* 2011, *2* (8), 1449-1456. 10.1039/C1SC00073J.

(49) Zhuravlev, L. T., The Surface Chemistry of Amorphous Silica. Zhuravlev Model. *Colloids Surf. A. Physicochem. Eng. Asp.* 2000, *173* (1), 1-38. https://doi.org/10.1016/S0927-7757(00)00556-2.

(50) Angel Wong, Y.-T.; Bryce, D. L., Chapter Four - Recent Advances in ^{11}B Solid-State Nuclear Magnetic Resonance Spectroscopy of Crystalline Solids. In *Annual Reports on Nmr Spectroscopy*, Webb, G. A., Ed. Academic Press: 2018; Vol. 93, pp 213-279.

(51) Hwang, S.-J.; Chen, C.-Y.; Zones, S. I., Boron Sites in Borosilicate Zeolites at Various Stages of Hydration Studied by Solid State NMR Spectroscopy. *J. Phys. Chem. B* 2004, *108* (48), 18535-18546. 10.1021/jp0476904.

(52) Kroeker, S.; Stebbins, J. F., Three-Coordinated Boron-11 Chemical Shifts in Borates. *Inorg. Chem.* 2001, *40* (24), 6239-6246. 10.1021/ic010305u.

(53) Hwang, S. J.; Fernandez, C.; Amoureux, J. P.; Cho, J.; Martin, S. W.; Pruski, M., Quantitative Study of the Short Range Order in B_2O_3 and B_2S_3 by Mas and Two-Dimensional Triple-Quantum MAS ^{11}B NMR. *Solid State Nuc. Magn. Res.* 1997, *8* (2), 109-121. https://doi.org/10.1016/S0926-2040(96)01280-5.

(54) Kong, X.; O'Dell, L. A.; Terskikh, V.; Ye, E.; Wang, R.; Wu, G., Variable-Temperature ^{17}O NMR Studies Allow Quantitative Evaluation of Molecular Dynamics in Organic Solids. *J.Am. Chem. Soc.* 2012, *134* (35), 14609-14617. 10.1021/ja306227p.

(55) Dračínský, M.; Hodgkinson, P., A Molecular Dynamics Study of the Effects of Fast Molecular Motions on Solid-State NMR Parameters. *CrystEngComm* 2013, *15* (43), 8705-8712. 10.1039/C3CE40612A.

(56) Eedugurala, N.; Wang, Z.; Chaudhary, U.; Nelson, N.; Kandel, K.; Kobayashi, T.; Slowing, I. I.; Pruski, M.; Sadow, A. D., Mesoporous Silica-Supported Amidozirconium-Catalyzed Carbonyl Hydroboration. *ACS Catal.* 2015, *5* (12), 7399-7414. 10.1021/acscatal.5b01671.

(57) Trébosc, J.; Wiench, J. W.; Huh, S.; Lin, V. S. Y.; Pruski, M., Solid-State NMR Study of MCM-41-Type Mesoporous Silica Nanoparticles. *J. Am. Chem. Soc.* 2005, *127* (9), 3057-3068. 10.1021/ja043567e.

(58) Andrews, L.; Burkholder, T. R., Infrared Spectra of Molecular $B(OH)_3$ and HOBO in Solid Argon. *J. Chem. Phys.* 1992, *97* (10), 7203-7210. 10.1063/1.463545.

(59) Gilson, T. R., Characterisation of Ortho- and Meta-Boric Acids in the Vapour Phase. *J. Chem. Soc., Dalton Trans.* 1991, (9), 2463-2466. 10.1039/DT9910002463.

(60) Chen, J.; Liang, T.; Li, J.; Wang, S.; Qin, Z.; Wang, P.; Huang, L.; Fan, W.; Wang, J., Regulation of Framework Aluminum Siting and Acid Distribution in H-MCM-22 by Boron Incorporation and Its Effect on the Catalytic Performance in Methanol to Hydrocarbons. *ACS Catal.* 2016, *6* (4), 2299-2313. 10.1021/acscatal.5b02862.

(61) Koller, H.; Fild, C.; Lobo, R. F., Variable Anchoring of Boron in Zeolite Beta. *Microporous and Mesoporous Mater.* 2005, *79* (1), 215-224. https://doi.org/10.1016/j.micromeso.2004.10.035.

(62) Lezcano-González, I.; Vidal-Moya, A.; Boronat, M.; Blasco, T.; Corma, A., Modelling Active Sites for the Beckmann Rearrangement Reaction in Boron-Containing Zeolites and Their Interaction with Probe Molecules. *Phys. Chem. Chem. Phys.* 2010, *12* (24), 6396-6403. 10.1039/C002427A.

(63) Tong, H. T. T.; Koller, H., Control of Al for B Framework Substitution in Zeolite Beta by Counterions. *Microporous and Mesoporous Mater.* 2012, *148* (1), 80-87. https://doi.org/10.1016/j.micromeso.2011.07.021.

(64) Wiper, P. V.; Amelse, J.; Mafra, L., Multinuclear Solid-State NMR Characterization of the Brønsted/Lewis Acid Properties in the Bp Hams-1b (H-[B]-ZSM-5) Borosilicate Molecular Sieve Using Adsorbed Tmpo and Tbpo Probe Molecules. *J. Catal.* 2014, *316*, 240-250. https://doi.org/10.1016/j.jcat.2014.05.017.

(65) Grant, J. T.; Love, A. M.; Carrero, C. A.; Huang, F.; Panger, J.; Verel, R.; Hermans, I., Improved Supported Metal Oxides for the Oxidative Dehydrogenation of Propane. *Top. Catal.* 2016, *59* (17), 1545-1553. 10.1007/s11244-016-0671-2.

(66) Hartmeyer, G.; Marichal, C.; Lebeau, B.; Rigolet, S.; Caullet, P.; Hernandez, J., Speciation of Silanol Groups in Precipitated Silica Nanoparticles by ^{1}H MAS NMR Spectroscopy. *J. Phys. Chem. C* 2007, *111* (26), 9066-9071. 10.1021/jp071490l.

(67) Dorémieux-Morin, C.; Heeribout, L.; Dumousseaux, C.; Fraissard, J.; Hommel, H.; Legrand, A. P., Study of the Constitutive Superficial Water of Precipitated Amorphous Silicas Using ^{1}H NMR: Broad-Line at 4 K and HR MAS at 300 K. *J. Am. Chem. Soc.* 1996, *118* (51), 13040-13045. 10.1021/ja962057k.

(68) Kim, H. N.; Lee, S. K., Atomic Structure and Dehydration Mechanism of Amorphous Silica: Insights from ^{29}Si and ^{1}H Solid-State MAS NMR Study of SiO_2 Nanoparticles. *Geochimica et Cosmochimica Acta* 2013, *120*, 39-64. https://doi.org/10.1016/j.gca.2013.05.047.

(69) Paris, M.; Fritsch, E.; Aguilar Reyes, B. O., ^{1}H, ^{29}Si and ^{27}Al NMR Study of the Destabilization Process of a Paracrystalline Opal from Mexico. *J. Non-Crystalline Solids* 2007, *353* (16), 1650-1656. https://doi.org/10.1016/j.jnoncrysol.2006.12.111.

CHAPTER 4

Tracking the Formation of the Active Phase on hBN during the Oxidative Dehydrogenation of Propane

This chapter has been prepared for publication under the following:

Cendejas, M. C.; Sokaras, D.; Dong, S.; Bare S. R.; Hermans, I, Tracking the Formation of the Active Phase on hBN during the Oxidative Dehydrogenation of Propane

Supporting Information for Chapter 4 is presented in Appendix B

Chapter 4: Tracking the Formation of the Active Phase on hBN during the Oxidative Dehydrogenation of Propane

4.1 Introduction

Hexagonal boron nitride (hBN) and other boron-containing materials are active and highly selective catalysts for the oxidative dehydrogenation (ODH) of propane to propylene.[1-4] Propylene is the 2nd highest volume organic chemical produced,[5] and as such, catalysts with the potential to produce propylene at a lower energy cost are greatly desired,[6] making the highly selective boron-based materials very promising catalysts.

The kinetics of ODH over hBN have been well established as a foundation to investigate the underlying mechanism.[2, 7-10] The reaction proceeds *via* a radical mechanism, presumably initiated by the surface.[9] The product selectivity is affected by the O_2 concentration in the gas phase, with C-C cracking products favored at low concentrations and ODH products favored at high concentrations.[7, 11] The addition of water in the form of steam to the reaction feed enhances the reaction rate, likely by increasing the radical pool, although the effect of steam on the surface has not yet been experimentally investigated.[9] We have hypothesized that water can help regenerate the active sites by catalyzing the surface dehydration (*vide infra*).

Catalytic activity on these boron materials is attributed to the formation of an amorphous boron oxide/hydroxide phase with the general formula $B_2(OH)_{2x}O_{3-x}$ ($x \leq 3$).[12-13] This phase is expected to be highly dynamic under ODH reaction conditions, as the reaction temperature (500 °C) is well above the Tamman temperature for boron oxide compounds (*e.g.,* m.p. of B_2O_3 = 450 °C; Tamman temp. = 225 °C). Because the active phase is molten and dynamic, it can easily sample many different stoichiometries of boron and oxygen and different structures within a given stoichiometry.[14] Extensive *ex situ* characterization studies have been conducted with the aim of identifying an active site, or at the very least identifying species that would correlate with the active

site.[12-13, 15-25] However, the nature of the active phase is such that the species present under reaction conditions are likely distinct from those present on the thermally relaxed surface observed *ex situ*, making an important case for *in situ* studies.

Our current hypothesis, based on a combined experimental and computational study, is that a metastable oxygen-deficient {BB} species can activate O_2 to generate surface BO• sites, which can then react with propane to initiate the radical reaction.[9] Any reaction with a BO• site results in the formation of B-OH, which is relatively unreactive. A proposed active site regeneration step is the water-assisted condensation of two adjacent B-OH species to release water and allow boron to reform the metastable site, {BB} (Figure 4.1). This regeneration step has a high calculated energy barrier of 222 kcal/mol, indicating that the surface regeneration step is kinetically slow.

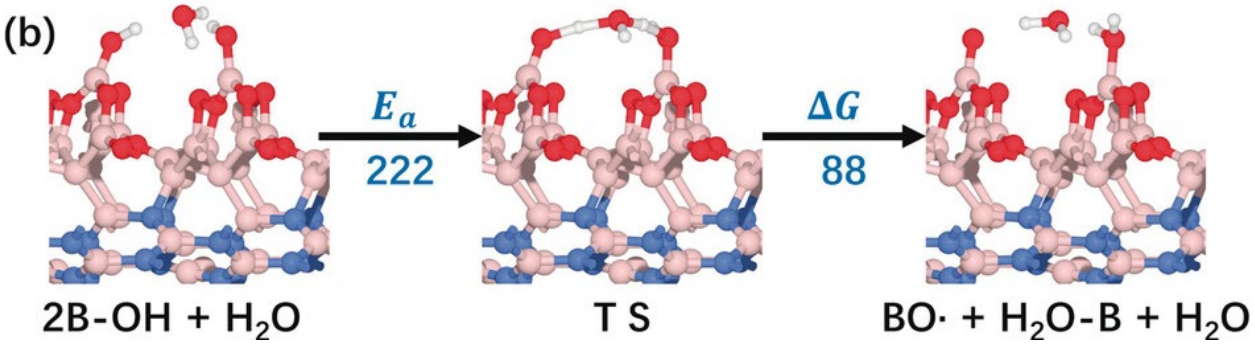

Figure 4.3. Structural model showing the water-assisted dehydration of the surface (figure from ref 9).

Few *in situ/operando* studies of this system have been reported, owing to the rather harsh reaction conditions in combination with the difficulties of analyzing the light elements that comprise the active phase. *In situ* vibrational spectroscopy (IR and Raman) has been employed with limited success.[3-4] Synchrotron vacuum ultraviolet photoionization mass spectrometry (SVUV-PIMS) was used to observe the formation of methyl radicals during propane ODH.[26] The analytical tools applied to this system so far have been limited in their sensitivity, resolution, and available sample environments, highlighting the need for improved *in situ/operando* methods.

X-Ray Absorption Spectroscopy (XAS) is a powerful tool for the *in situ/operando* measurements of heterogenous catalysts, providing detailed atomistic information about geometry, oxidation state, and the local coordination environment. For light elements, such as B, N, C, and O, soft X-rays (<1 keV) are needed to measure XAS. The need for soft x-rays limits the types of experiments that can be done, as the short scattering path necessitates the use of vacuum chambers.

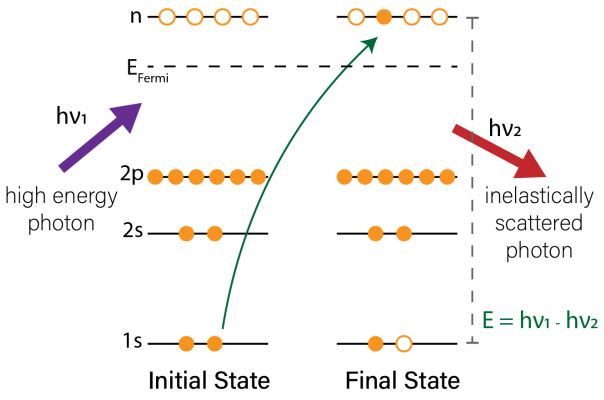

Figure 4.2. Illustration of X-Ray Raman process.

X-Ray Raman Spectroscopy (XRS) measures the energy loss of a hard X-ray (>5 keV), generating XAS-equivalent information.[27-28] General Raman scattering refers to the inelastic scattering of photons by matter. Typically, this process involves a molecule or compound gaining vibrational energy by scattering an incident visible photon. When X-rays are used, electronic transitions are induced. In an XRS experiment, a high energy photon (*ca*. 6.5 keV) excites a core electron of a desired element and is inelastically scattered (Figure 4.2). The difference between the incident photon and the scattered photon equals the energy needed to excite a core electron. Because the energy transfer from a hard x-ray is measured, XRS enables the measurement of the K-edge of light elements under atmospheric conditions. The use of hard x-rays allows for studies of light element-containing catalysts under true working conditions.

The use of XRS has been limited by the small Raman scattering cross-section and is only made possible by improvements in synchrotron optics and large acceptance, high resolution spectrometers.[28] This technique is at the forefront of *in situ* spectroscopy has been used to study intercalation in hydrogen sorption and battery materials.[29-33] The application of XRS in the study

of heterogenous catalysts is in its infancy, with this study serving as the first *operando* measurement of a heterogeneous catalyst using this technique.

With XRS, we can probe boron catalysts under true working conditions, a feat which has not yet been achieved. hBN undergoes an induction period of several hours during which the propane conversion and product distribution fluctuate before reaching a steady state. Based on *ex situ* characterization, this induction period is attributed to the formation of the oxidized boron phase necessary for catalytic activity. The steady-state catalytic activity of hBN has been thoroughly characterized, while studies of the induction period have been lacking. In this study, we use *operando* XRS to observe the oxidation of hBN during the catalyst induction period in the ODH of propane. However, XRS is a bulk measurement while catalysis is a surface event, suggesting that traditional bulk hBN would yield noisy spectra. To increase the active surface area and achieve enhanced signal from the active phase, of hBN nanosheets (hBNNS) were used in this study.

4.2 Materials and Methods

Sample Preparation. hBNNS were prepared *via* sonication as described in the literature.[34] Commercial hBN was suspended in DI water and sonicated using a tip sonicator at 75% amplitude with 1s on/4s off pulse cycles for a total of 4h sonication (~26h total). The suspension was transferred into centrifuge tubes and allowed to settle overnight, followed by centrifugation at 4500 rpm for 30 min. The top ¾ of the liquid was collected and dried. SEM and TEM images show successful exfoliation of hBN into nanosheets (Figure S1).

X-Ray Raman Measurements. The hBNNS sample was packed into a 1mm o.d. quartz capillary tube to make a 5mm long catalyst bed, supported on either side by quartz wool. The packed capillary tube was loaded into an *in situ* XAS capillary flow cell (illustration and packed cell shown in Figure 4.3).[35]

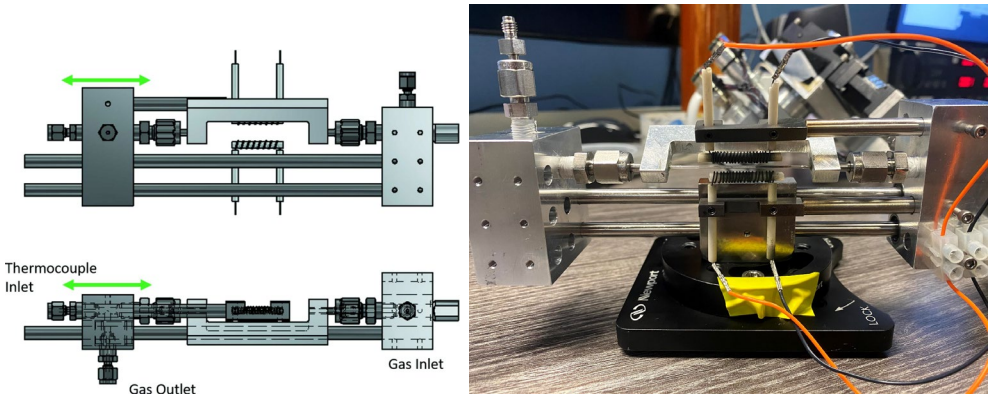

Figure 4.3. Illustration of capillary flow cell (left, from ref. 30) and a photo showing the packed capillary tube (right).

The sample cell was mounted at BL 15-2 at the Stanford Synchrotron Radiation Lightsource (SSRL).[28] A scheme of the experimental setup at BL 15-2 is shown in Figure 4.4, and the details of the beamline have been reported elsewhere.[28]

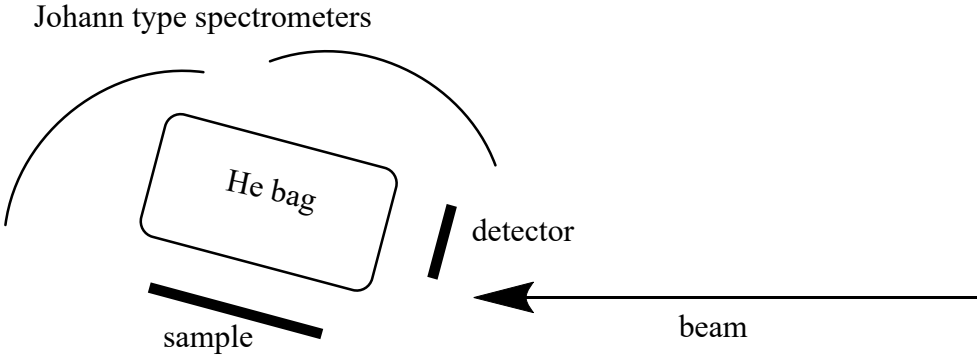

Figure 4.4. Diagram of the XRS setup at BL 15-2.

The *operando* experiments were performed using a gas flow control board and mass spectrometer provided by the CoACCESS Laboratory at SSRL. Propane, synthetic air, and He flows were controlled by individual mass flow controllers calibrated for the specific gas. The outlet

of the reactor cell was connected to the mass spectrometer. Computers outside of the experimental hutch controlled and monitored the MS and the reactor gas flow, pressure, and temperature.

Data Analysis. Each spectrum under reaction conditions is the average of 5 scans (ca. 7 min per scan; ca. 35 min per spectrum); each spectrum under air is the average of 10 scans. All spectra were normalized in the Athena software package and the peak areas were integrated using Origin software.

4.3. Results

The hBNNS sample was packed into a 1mm o.d. quartz capillary tube, loaded into a capillary flow cell, and mounted at the beamline. At room temperature under a flow of air, the hBNNS sample exhibits a strong, sharp peak at 192 eV and a set of broader features above 197 eV (Figure 4.5). The 192 eV feature is attributed to B 1s → π* transition in hBN (BN_3 species), while transitions to σ* and π* contribute to the features above 197 eV.[36] This spectrum agrees with XRS and XAS reported in the literature.[13, 36]

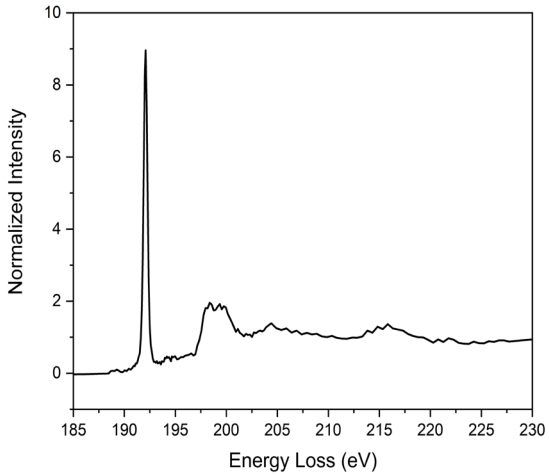

Figure 4.5. X-Ray Raman B K-edge spectrum of hBNNS at room temperature.

The sample was heated from room temperature to 500 °C (10 °C/min) under a flow of synthetic air (10 sccm). After the temperature stabilized, propane was added into the feed in a 2:1 C_3H_8:O_2 ratio to give a total flow rate of 10 sccm (3 sccm C_3H_8, 7 sccm air), and spectra were continuously recorded. Each spectrum under reaction conditions is the average of 5 scans (*ca.* 7 min per scan, *ca.* 35 min each spectrum); each spectrum under air is the average of 10 scans.

After the 5th spectrum, the total flow rate is decreased to 7 sccm (2 sccm C_3H_8, 5 sccm air) to increase the contact time and the reaction proceeds until there is a steady amount of boron oxide (*ca.* 7.5 h total reaction time). The sample is cooled to room temperature, then heated back up to 500 °C and re-exposed to reaction conditions for 105 min before being cooled back down to end the experiment.

The outlet of the reactor was monitored by mass spectrometry (Figure S2). When propane is added to the hot reactor, the signals for ODH reaction products (m/z = 18 (H_2O) and 42 (C_3H_6)) increase, indicating that catalysis was occurring.

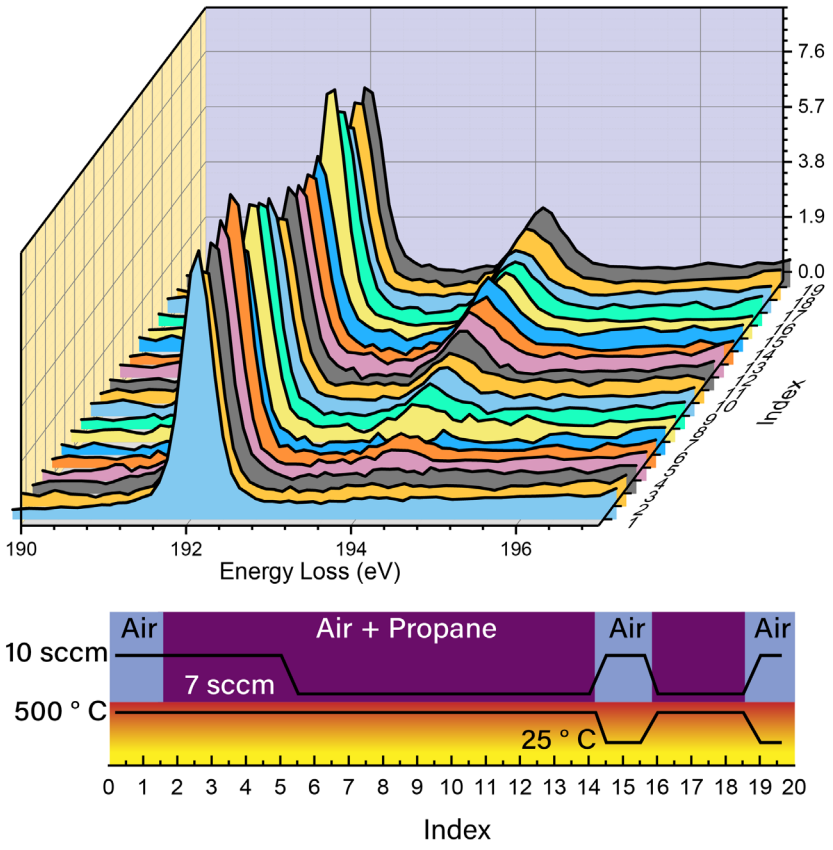

Figure 4.6. *Operando* X-Ray Raman spectra of the B K-edge of hBNNS during propane ODH. Experimental conditions are shown in the legend below the spectra.

Two features at 192 eV and 194 eV are observed during the reaction. As seen in Figure 4.5, the peak at 192 eV corresponds to BN_3 species. The peak at 194 eV corresponds to BO_3-

type species (B_2O_3 B K-edge XRS spectrum shown in Figure S3). Figure 4.6 shows the growth in the intensity of the boron oxide feature over the course of the reaction, except for outliers at spectra 7 and 15. The intensity of the BN_3 peak has a less apparent trend than the BO_3 feature.

The 192 and 194 eV signals were integrated, and the percent areas over the course of the experiment are plotted in Figure 4.7. With a total flow rate of 10 sccm, there is a slow increase in the amount of oxidized boron. When the flow rate is decreased to 7 sccm, increasing the contact time, the amount of oxide initially decreases then quickly increases, eventually reaching a maximum of *ca*. 25% of the total integrated area. This value is similar to the previous oxide quantification by SSNMR, which shows that hBN after reaction contains 30% *ca.* BO_3 .[13] Upon cooling to 25 °C, there is a slight decrease in the amount of oxide, which is reversed when the sample is re-exposed to reaction conditions. The amount of oxide increase is marginal upon re-

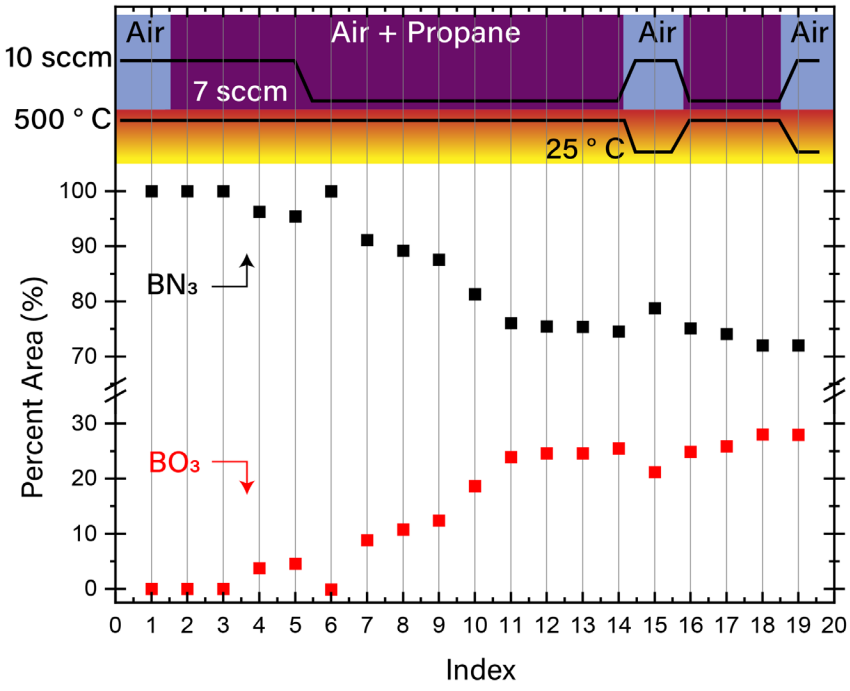

Figure 4.7. BN_3 and BO_3 percent areas over the course of the experiment. Reaction conditions are shown in the legend at the top of the figure.

exposure to reaction conditions, likely indicating the surface has reached a steady state composition.

4.4 Discussion

These results are the first direct observation of the hBN surface oxidation during the induction period, confirming the assumption based on *ex situ* characterization and reactivity studies. These results also show that once the boron oxide layer is formed, the reactivity and the structure is stable. This observation highlights the importance of studying the induction period to understanding the origins of activity on boron-based catalysts.

Interestingly, when the flow rate is decreased, the oxide temporarily disappears for a spectrum (no. 6), reappearing in the next (*i.e.,* the oxide was not present far *ca*. 35 min.). Decreasing the gas flow rate increases the contact time and therefore the conversion, so one possible explanation for the temporary loss of the BO_3 signal is that the species were consumed through reaction with propane, and the re-oxidation of hBN is slow at this stage of the reaction. Indeed, the MS shows a brief increase in the signals associated with reaction products (C_3H_6 and H_2O) and a decrease in the O_2 signal upon the change in flow rate (Figure S4). These results also indicate that the O_2/C_3H_8 ratio might be important in controlling the surface speciation. However, more work is needed to understand the effect of gas composition on the surface.

4.5 Conclusion

We observed the formation of the boron oxide phase on hBN during the induction period of the propane ODH reaction. We found that the oxide gradually grows in over the course of reaction, eventually reaching a steady composition. This study is the first direct observation of the surface changes that occur during the induction period. While these results are expected, they demonstrate the power XRS has in observing this system, allowing us to design experiments that can answer lingering questions.

4.6 References

(1) Grant, J. T.; Carrero, C. A.; Goeltl, F.; Venegas, J.; Mueller, P.; Burt, S. P.; Specht, S. E.; McDermott, W. P.; Chieregato, A.; Hermans, I., Selective Oxidative Dehydrogenation of Propane to Propene Using Boron Nitride Catalysts. *Science (Washington, DC, U. S.)* **2016,** *354* (6319), 1570-1573. 10.1126/science.aaf7885.

(2) Grant, J. T.; McDermott, W. P.; Venegas, J. M.; Burt, S. P.; Micka, J.; Phivilay, S. P.; Carrero, C. A.; Hermans, I., Boron and Boron-Containing Catalysts for the Oxidative Dehydrogenation of Propane. *ChemCatChem* **2017,** *9* (19), 3623-3626. 10.1002/cctc.201701140.

(3) Huang, R.; Zhang, B.; Wang, J.; Wu, K.-H.; Shi, W.; Zhang, Y.; Liu, Y.; Zheng, A.; Schloegl, R.; Su, D. S., Direct Insight into Ethane Oxidative Dehydrogenation over Boron Nitrides. *ChemCatChem* **2017,** *9* (17), 3293-3297. 10.1002/cctc.201700725.

(4) Shi, L.; Wang, D.; Song, W.; Shao, D.; Zhang, W.-P.; Lu, A.-H., Edge-Hydroxylated Boron Nitride for Oxidative Dehydrogenation of Propane to Propylene. *ChemCatChem* **2017,** *9* (10), 1788-1793. 10.1002/cctc.201700004.

(5) Rightor, E. G.; Tway, C. L., Global Energy & Emissions Reduction Potential of Chemical Process Improvements. *Catalysis Today* **2015,** *258* (Part 2), 226-229. https://doi.org/10.1016/j.cattod.2015.02.023.

(6) Cavani, F.; Ballarini, N.; Cericola, A., Oxidative Dehydrogenation of Ethane and Propane: How Far from Commercial Implementation? *Catalysis Today* **2007,** *127* (1), 113-131. https://doi.org/10.1016/j.cattod.2007.05.009.

(7) Venegas, J. M.; Grant, J. T.; McDermott, W. P.; Burt, S. P.; Micka, J.; Carrero, C. A.; Hermans, I., Selective Oxidation of N-Butane and Isobutane Catalyzed by Boron Nitride. *ChemCatChem* **2017,** *9* (12), 2118-2127. 10.1002/cctc.201601686.

(8) Venegas, J. M.; Hermans, I., The Influence of Reactor Parameters on the Boron Nitride-Catalyzed Oxidative Dehydrogenation of Propane. *Org. Process Res. Dev.* **2018,** *22* (12), 1644-1652. 10.1021/acs.oprd.8b00301.

(9) Venegas, J. M.; Zhang, Z.; Agbi, T. O.; McDermott, W. P.; Alexandrova, A.; Hermans, I., Why Boron Nitride Is Such a Selective Catalyst for the Oxidative Dehydrogenation of Propane. *Angew. Chem., Int. Ed.* **2020,** *59* (38), 16527-16535. 10.1002/anie.202003695.

(10) Kraus, P.; Lindstedt, R. P., It's a Gas: Oxidative Dehydrogenation of Propane over Boron Nitride Catalysts. *J. Phys. Chem. C* **2021,** *125* (10), 5623-5634. 10.1021/acs.jpcc.1c00165.

(11) McDermott, W. P.; Venegas, J.; Hermans, I., Selective Oxidative Cracking of N-Butane to Light Olefins over Hexagonal Boron Nitride with Limited Formation of Cox. *ChemSusChem* **2020,** *13* (1), 152-158. 10.1002/cssc.201901663.

(12) Love, A. M.; Cendejas, M. C.; Thomas, B.; McDermott, W. P.; Uchupalanun, P.; Kruszynski, C.; Burt, S. P.; Agbi, T.; Rossini, A. J.; Hermans, I., Synthesis and Characterization of Silica-Supported Boron Oxide Catalysts for the Oxidative Dehydrogenation of Propane. *J. Phys. Chem. C* **2019,** *123* (44), 27000-27011. 10.1021/acs.jpcc.9b07429.

(13) Love, A. M.; Thomas, B.; Specht, S. E.; Hanrahan, M. P.; Venegas, J. M.; Burt, S. P.; Grant, J. T.; Cendejas, M. C.; McDermott, W. P.; Rossini, A. J., et al., Probing the Transformation of Boron Nitride Catalysts under Oxidative Dehydrogenation Conditions. *J. Am. Chem. Soc.* **2019,** *141* (1), 182-190. 10.1021/jacs.8b08165.

(14) Zhang, Z.; Jimenez-Izal, E.; Hermans, I.; Alexandrova, A. N., Dynamic Phase Diagram of Catalytic Surface of Hexagonal Boron Nitride under Conditions of Oxidative Dehydrogenation of Propane. *J. Phys. Chem. Lett.* **2019,** *10* (1), 20-25. 10.1021/acs.jpclett.8b03373.

(15) Lu, W.-D.; Wang, D.; Zhao, Z.; Song, W.; Li, W.-C.; Lu, A.-H., Supported Boron Oxide Catalysts for Selective and Low-Temperature Oxidative Dehydrogenation of Propane. *ACS Catal.* **2019,** *9* (9), 8263-8270. 10.1021/acscatal.9b02284.

(16) Altvater, N. R.; Dorn, R. W.; Cendejas, M. C.; McDermott, W. P.; Thomas, B.; Rossini, A. J.; Hermans, I., B-Mww Zeolite: The Case against Single-Site Catalysis. *Angew. Chem., Int. Ed.* **2020,** *59* (16), 6546-6550. 10.1002/anie.201914696.

(17) Belgamwar, R.; Rankin, A. G. M.; Maity, A.; Mishra, A. K.; Gomez, J. S.; Trebosc, J.; Vinod, C. P.; Lafon, O.; Polshettiwar, V., Boron Nitride and Oxide Supported on Dendritic Fibrous Nanosilica for Catalytic Oxidative Dehydrogenation of Propane. *ACS Sustainable Chem. Eng.* **2020,** *8* (43), 16124-16135. 10.1021/acssuschemeng.0c04148.

(18) Dorn, R. W.; Cendejas, M. C.; Chen, K.; Hung, I.; Altvater, N. R.; McDermott, W. P.; Gan, Z.; Hermans, I.; Rossini, A. J., Structure Determination of Boron-Based Oxidative Dehydrogenation Heterogeneous Catalysts with Ultrahigh Field 35.2 T 11B Solid-State NMR Spectroscopy. *ACS Catal.* **2020,** *10* (23), 13852-13866. 10.1021/acscatal.0c03762.

(19) Qiu, B.; Jiang, F.; Lu, W.-D.; Yan, B.; Li, W.-C.; Zhao, Z.-C.; Lu, A.-H., Oxidative Dehydrogenation of Propane Using Layered Borosilicate Zeolite as the Active and Selective Catalyst. *J. Catal.* **2020,** *385*, 176-182. 10.1016/j.jcat.2020.03.021.

(20) Si, C.; Lian, Z.; Olanrele, S. O.; Sun, X. Y.; Li, B., Revealing the Origin of the Reactivity of Metal-Free Boron Nitride Catalysts in Oxidative Dehydrogenation of Propane. *Appl. Surf. Sci.* **2020,** *519*, 146241. 10.1016/j.apsusc.2020.146241.

(21) Cendejas, M. C.; Dorn, R. W.; McDermott, W. P.; Lebron-Rodriguez, E. A.; Mark, L. O.; Rossini, A. J.; Hermans, I., Controlled Grafting Synthesis of Silica-Supported Boron for Oxidative Dehydrogenation Catalysis. *J. Phys. Chem. C* **2021,** *125* (23), 12636-12649. 10.1021/acs.jpcc.1c01899.

(22) Liu, Z.; Yan, B.; Meng, S.; Liu, R.; Lu, W.-D.; Sheng, J.; Yi, Y.; Lu, A.-H., Plasma Tuning Local Environment of Hexagonal Boron Nitride for Oxidative Dehydrogenation of Propane. *Angew Chem Int Ed Engl* **2021**.

(23) Mark, L. O.; Dorn, R. W.; McDermott, W. P.; Agbi, T. O.; Altvater, N. R.; Jansen, J.; Lebron-Rodriguez, E. A.; Cendejas, M. C.; Rossini, A. J.; Hermans, I., Highly Selective Carbon-Supported

Boron for Oxidative Dehydrogenation of Propane. *ChemCatChem* **2021**, Ahead of Print. 10.1002/cctc.202100759.

(24) Yan, H.; Alayoglu, S.; Wu, W.; Zhang, Y.; Weitz, E.; Stair, P. C.; Notestein, J. M., Identifying Boron Active Sites for the Oxidative Dehydrogenation of Propane. *ACS Catal.* **2021,** *11* (15), 9370-9376. 10.1021/acscatal.1c02168.

(25) Zhou, H.; Yi, X.; Hui, Y.; Wang, L.; Chen, W.; Qin, Y.; Wang, M.; Ma, J.; Chu, X.; Wang, Y., et al., Isolated Boron in Zeolite for Oxidative Dehydrogenation of Propane. *Science (Washington, DC, U. S.)* **2021,** *372* (6537), 76-80. 10.1126/science.abe7935.

(26) Zhang, X.; You, R.; Wei, Z.; Jiang, X.; Yang, J.; Pan, Y.; Wu, P.; Jia, Q.; Bao, Z.; Bai, L., et al., Radical Chemistry and Reaction Mechanisms of Propane Oxidative Dehydrogenation over Hexagonal Boron Nitride Catalysts. *Angew. Chem., Int. Ed.* **2020,** *59* (21), 8042-8046. 10.1002/anie.202002440.

(27) Bergmann, U.; Glatzel, P.; Cramer, S. P., Bulk-Sensitive Xas Characterization of Light Elements: From X-Ray Raman Scattering to X-Ray Raman Spectroscopy. *Microchemical Journal* **2002,** *71* (2), 221-230. https://doi.org/10.1016/S0026-265X(02)00014-0.

(28) Sokaras, D.; Nordlund, D.; Weng, T.-C.; Mori, R. A.; Velikov, P.; Wenger, D.; Garachtchenko, A.; George, M.; Borzenets, V.; Johnson, B., et al., A High Resolution and Large Solid Angle X-Ray Raman Spectroscopy End-Station at the Stanford Synchrotron Radiation Lightsource. *Review of Scientific Instruments* **2012,** *83* (4), 043112. 10.1063/1.4704458.

(29) Miedema, P. S.; Ngene, P.; van der Eerden, A. M. J.; Weng, T.-C.; Nordlund, D.; Sokaras, D.; Alonso-Mori, R.; Juhin, A.; de Jongh, P. E.; de Groot, F. M. F., In Situ X-Ray Raman Spectroscopy of Libh4. *Phys. Chem. Chem. Phys.* **2012,** *14* (16), 5581-5587. 10.1039/c2cp24025d.

(30) Miedema, P. S.; Ngene, P.; van der Eerden, A. M. J.; Sokaras, D.; Weng, T.-C.; Nordlund, D.; Au, Y. S.; de Groot, F. M. F., In Situ X-Ray Raman Spectroscopy Study of the Hydrogen

Sorption Properties of Lithium Borohydride Nanocomposites. *Phys. Chem. Chem. Phys.* **2014,** *16* (41), 22651-22658. 10.1039/C4CP02918F.

(31) Braun, A.; Nordlund, D.; Song, S.-W.; Huang, T.-W.; Sokaras, D.; Liu, X.; Yang, W.; Weng, T.-C.; Liu, Z., Hard X-Rays in-Soft X-Rays Out: An Operando Piggyback View Deep into a Charging Lithium Ion Battery with X-Ray Raman Spectroscopy. *J. Electron Spectrosc. Relat. Phenom.* **2015,** *200*, 257-263. 10.1016/j.elspec.2015.03.005.

(32) Ketenoglu, D.; Spiekermann, G.; Harder, M.; Oz, E.; Yin, Z.; Yavas, H.; Koz, C.; Yagci, M. C.; Yilmaz, E.; Sahle, C. J., et al., X-Ray Raman Spectroscopy of Lithium-Ion Battery Electrolyte Solutions in a Flow Cell. *J Synchrotron Radiat* **2018,** *25* (Pt 2), 537-542.

(33) Boesenberg, U.; Sokaras, D.; Nordlund, D.; Weng, T.-C.; Gorelov, E.; Richardson, T. J.; Kostecki, R.; Cabana, J., Electronic Structure Changes Upon Lithium Intercalation into Graphite - Insights from Ex Situ and Operando X-Ray Raman Spectroscopy. *Carbon* **2019,** *143*, 371-377. 10.1016/j.carbon.2018.11.031.

(34) Dorn, R. W.; Ryan, M. J.; Kim, T.-H.; Goh, T. W.; Venkatesh, A.; Heintz, P. M.; Zhou, L.; Huang, W.; Rossini, A. J., Identifying the Molecular Edge Termination of Exfoliated Hexagonal Boron Nitride Nanosheets with Solid-State NMR Spectroscopy and Plane-Wave DFT Calculations. *Chemistry of Materials* **2020,** *32* (7), 3109-3121. 10.1021/acs.chemmater.0c00104.

(35) Hoffman, A. S.; Singh, J. A.; Bent, S. F.; Bare, S. R., In Situ Observation of Phase Changes of a Silica-Supported Cobalt Catalyst for the Fischer-Tropsch Process by the Development of a Synchrotron-Compatible in Situ/Operando Powder X-Ray Diffraction Cell. *Journal of Synchrotron Radiation* **2018,** *25* (6), 1673-1682. doi:10.1107/S1600577518013942.

(36) Watanabe, N.; Hayashi, H.; Udagawa, Y.; Takeshita, K.; Kawata, H., Anisotropy of Hexagonal Boron Nitride Core Absorption Spectra by X-Ray Raman Spectroscopy. *Appl. Phys. Lett.* **1996,** *69* (10), 1370-1372. 10.1063/1.117439.

CHAPTER 5

Ambient Pressure X-Ray Photoelectron Spectroscopy of hBN Nanosheets During the Oxidative Dehydrogenation of Propane

Supplemental Information for Chapter 5 is provided in Appendix C.

Chapter 5: Ambient Pressure X-Ray Photoelectron Spectroscopy of hBN Nanosheets During the Oxidative Dehydrogenation of Propane

5.1 Introduction

Hexagonal boron nitride (hBN) and other boron-based materials are highly selective catalysts for the oxidative dehydrogenation (ODH) of propane to propylene.[1-5] The origin of the activity on the surface is the subject of much interest. *Ex situ* characterization has shown that an amorphous oxidized boron phase with the general formula $B_2(OH)_{2x}O_{3-x}$ ($x \leq 3$) forms on the surface of hBN.[6] This boron oxide phase is responsible for catalytic activity.[5-7] hBN exhibits an induction period during which the propane conversion fluctuates before reaching a steady state.[8] Operando X-Ray Raman spectroscopy shows that the boron oxide gradually increases over the first hours of the propane ODH reaction before reaching a stable composition of nitride and boron (Chapter 4). However, *in situ* spectroscopy studies have been limited because of the harsh reaction conditions.

X-ray Photoelectron Spectroscopy (XPS) is commonly used for surface characterization.[9-10] In XPS, an incident x-ray excites an electron from a core level to the vacuum and the kinetic energy of the escaping photoelectron is measured. The difference between the incident photon energy and the photoelectron kinetic energy corresponds to the electron binding energy. XPS is a surface sensitive technique, as the photoelectrons generated from the x-ray escape from the upper *ca.* 10 nm of the sample.[9] With XPS, elemental composition, chemical state, and the relative composition of a sample can be determined. Typically, XPS is performed under ultrahigh vacuum (UHV, $P < 1 \times 10^{-6}$ Pa), which limits the samples and sample environments that can be characterized using XPS.

Near-ambient pressure XPS (NAP-XPS) has been developed to expand the capabilities of this technique to study samples closer to their native environments.[9] In this study, we use NAP-XPS to observe the changes the occur in the O, N, and B 1s regions of hBN nanosheets (hBNNS)

upon exposure to propane ODH conditions. hBNNS were used to increase the reactive surface area and to mitigate any potential sample charging issues.

5.2 Materials and Methods

hBN nanosheets (hBNNS) were prepared via a temperature shock method as reported in the literature.[11] Commercial hBN was loaded into a quartz crucible and the crucible was placed in a muffle furnace heated to 800 °C. The crucible sat in the furnace at 800 °C for 5 minutes and immediately transferred into a stainless steel dewar filled with liquid N_2. The crucible was filled with liquid nitrogen and placed on the counter until all N_2 had evaporated. This process was repeated 10 times. The sample was then suspended in DI H_2O in a centrifuge tube, sonicated in a bath sonicator, and centrifuged at 4000 rpm for 30 min. The supernatant was collected and dried in a 150 °C oven. The nanosheets were analyzed by SEM and TEM to observe the extent of exfoliation (Figure S1).

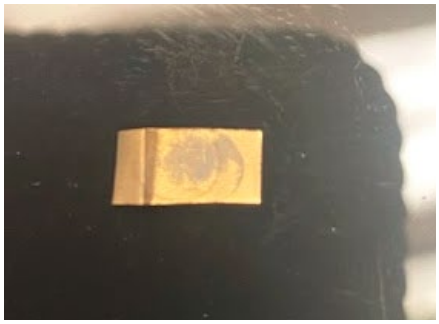

Figure 5.1 Photo of the hBNNS/Ti foil sample used in the NAP-XPS experiments.

To prepare the sample for XPS analysis, ~1 mg of hBNNS were dispersed in ~10 mL DI H2O and dropped onto a small piece of Ti foil (Figure 5.1).

NAP-XPS experiments were performed at beamline 13-2 at the Stanford Synchrotron Radiation Lightsource (SSRL). Two different incident photon energies were used: 940 eV and 675 eV. The spectra were referenced to the fermi level.

5.3. Results and Discussion

hBN is an insulating material and exhibits sample charging during the XPS experiment (Figure S2). In a typical lab based UHV XPS experiment, sample charging is compensated for by irradiating the sample with an ion or electron beam. Such charge compensation schemes are not available during an *in situ* experiment. In an effort to mitigate sample charging effects, we

prepared hBN nanosheets via a previously reported temperature shock method. SEM and TEM of the hBNNS sample were used to observe the extent of exfoliation of commercial hBN (Figure S1). hBNNS provide the added benefit of increased reactive surface area, which should lead to improvements in signal to noise.

The hBNNS sample was dispersed in water and deposited onto a small piece of Ti foil. The sample was allowed to dry before being loaded into the AP-XPS sample chamber at BL 13-2 at SSRL. All experiments described were done with the same hBNNS/Ti foil sample. Two different photon energies – 940 eV and 675 eV – were used to probe different depths. Each spectrum is comprised of the O, N, and B 1s regions, taking ca. 16 minutes total. The binding energies are referenced to the Fermi level at 0 eV binding energy.

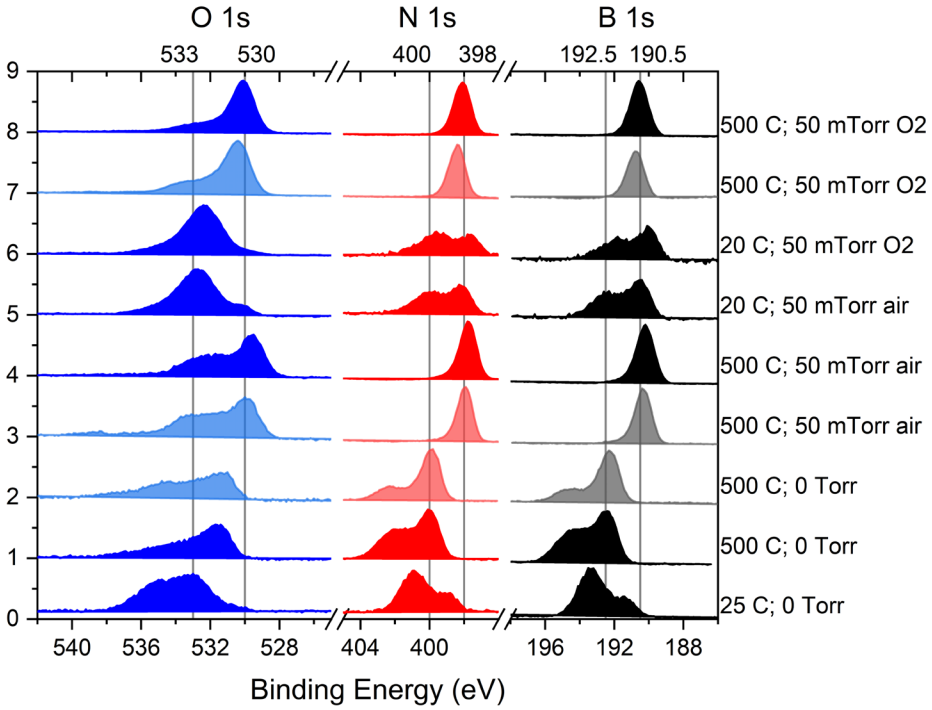

Figure 5.2 NAP-XPS spectra of the O, N, and B 1s regions of hBNNS/Ti foil under the conditions indicated to the right of the spectra. The lighter colored spectra were acquired using a 940 eV incident photon, while the darker spectra were acquired using a 675 eV photon.

To gain a baseline understanding of the sample, we acquired spectra with 0 mTorr gas pressure at 25 °C and 500 °C (Figure 5.2). We then introduced air at 500 °C followed by cooling the sample to 20 °C. Next, the gas atmosphere was changed to O_2, and spectra at 20 °C were acquired before heating the sample back up to 500 °C. Notably, the spectra acquired with 0 Torr gas pressure are shifted 2 eV higher than the spectra recorded with 50 mTorr gas present. This difference is consistent with the binding energy difference seen with lab-based UHV XPS spectra acquired with and without charge compensation (Figure S2), indicating that the NAP-XPS spectra acquired with gas in the chamber exhibit little to no charging effects.

The B 1s spectra at 500 °C can be fit with a single peak at 190.5 eV, corresponding to BN_3 species.[12] The N 1s region under the same conditions can be fitted with a single peak at 398 eV, typical for hBN.[12] At low temperatures, a feature at higher binding energies can be seen in the B and N 1s regions centered around 192.5 eV and 400 eV, respectively. The boron 1s signal in the range of 192-193 eV indicates oxidized boron,[13-14] and the nitrogen 1s signal in the range of 399-400 eV corresponds to primary amines.[15-16] These higher binding energy features are not observed at high temperature, suggesting that the species that give rise to those signals evaporate and leave the surface. We note that B_2O_3 has a melting point of 450 °C. This is in line with the O 1s spectra, which exhibit two main features centered around 530 eV and 533 eV. The 533 eV feature corresponds to boron oxide compounds,[17] while the feature at 530 eV is typical of metal oxides. The feature at 533 eV decreases with the boron oxide feature at 193 eV, further suggesting that the boron oxide present around room temperature evaporates from the surface at high temperatures. The 530 eV peak is most likely attributed to the formation of an oxide layer on the underlying Ti foil in the form of TiO_2, although this species has not been confirmed.

To perform the propane ODH reaction, the sample was heated from 230 °C to 500 °C in 50 mTorr O_2. Once the temperature stabilized, C_3H_8 was added into the chamber and spectra were acquired continuously for ca. 5.5 hours (Figure 5.3).

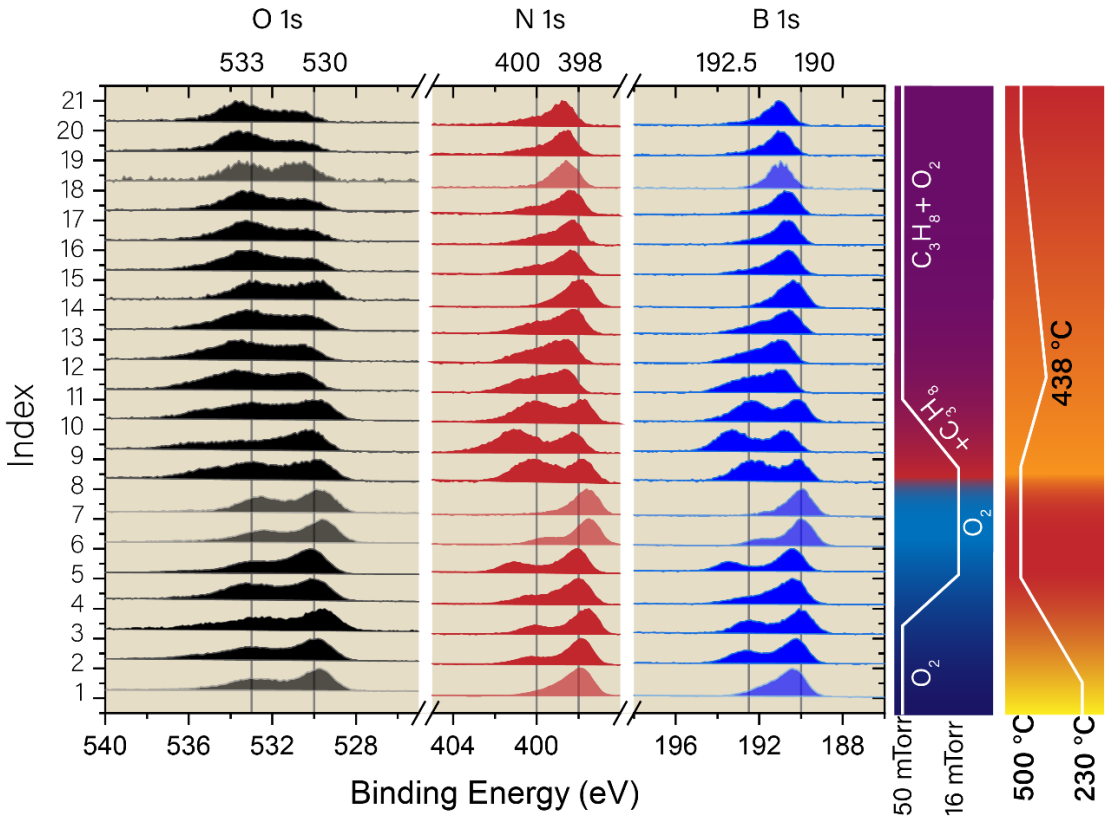

Figure 5.3 *In situ* spectra of the O, N, and B 1s regions of hBNNS recorded over the course of sample treatment under propane ODH conditions. Each spectrum is normalized to the maximum intensity for enhanced clarity in the stacked plot. The reaction conditions are shown in the legends to the right of the spectra. The lighter colored spectra were acquired using a 940 eV photon and the darker were acquired using a 675 eV photon.

The spectra in Figure 5.3 were deconvoluted in CasaXPS and the fractional compositions (f_x) were determined based on Equation 1.

$$f_x = \frac{\frac{A_x}{S_x \lambda_x}}{\sum \frac{A_i}{S_i \lambda_i}} \qquad \text{Equation 1}$$

Where A_x is the area of the region of interest, S_x is the element-specific sensitivity factor, and λ_x is the inelastic mean free path (IMFP) for each element. The sensitivity factors scale almost

linearly with the kinetic energy of the escaping electron and are calculated relative to B 1s. IMFP for boron was taken from the NIST XPS database and used to estimate values for N and O. The results of this analysis are shown in Figure 5.4. 20 spectra were taken over the course of the *in situ* experiment and are indexed along the horizontal axis. The color bars above the plot indicate the temperature and gas composition. The bar graphs are color coded by element, with the different color families corresponding to the individual element compositions. The different shades correspond to the deconvoluted species as indicated by the legend to the right. All spectra were

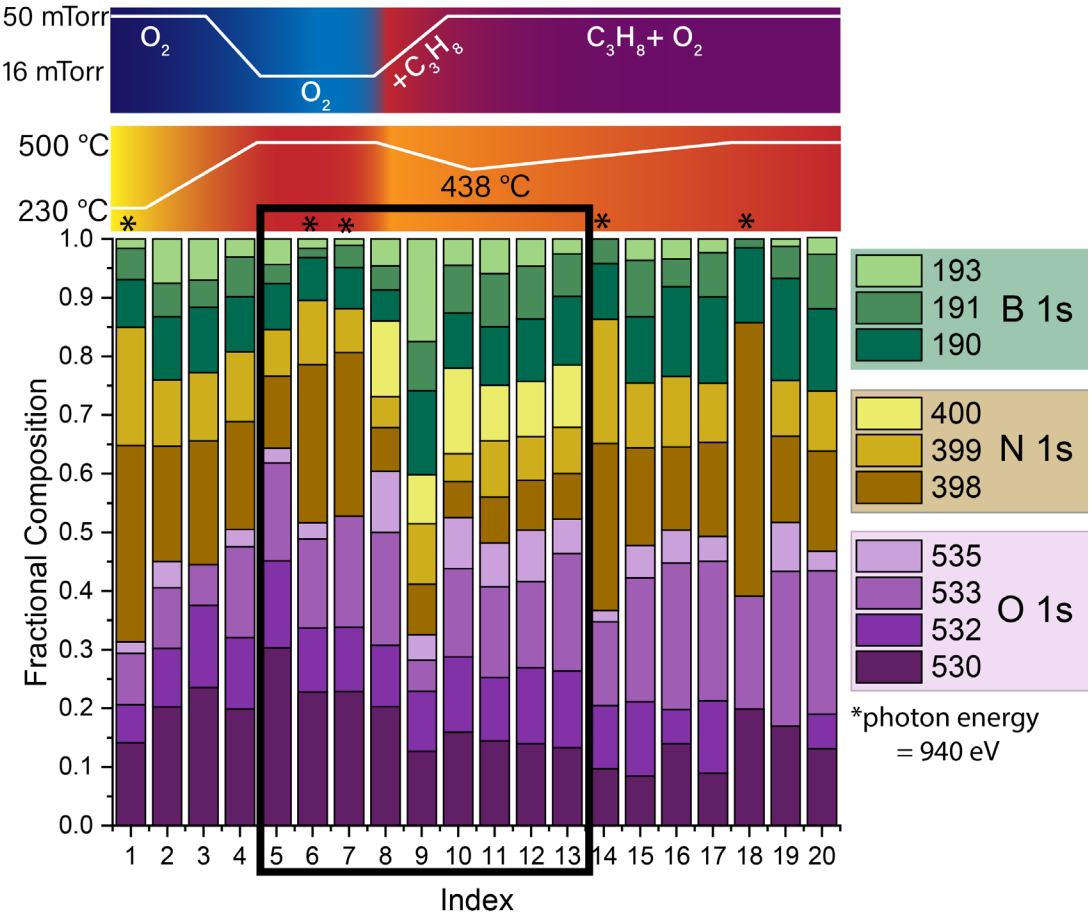

Figure 5.4 Fractional composition of the surface over the course of the *in situ* experiment. Reaction conditions are given in the legend above the plot. The color families – purple, orange, green – correspond to total atomic contribution from O, N, and B, respectively. The different shades within a color family correspond to the individual species indicated in the legend to the right. The asterisks* denote spectra acquired using a 940 eV incident photon.

acquired using 675 eV photon energy expect those denoted with asterisks that used 940 eV.

While the analysis and interpretation of this data is ongoing, I present here my preliminary observations and takeaways.

Over the first 4 spectra as the sample is heating up, the amount of oxygen increases at the expense of boron. The fractional composition of oxygen is highest at spectrum 5 when the sample is at 500 °C under 16 mTorr O_2. At spectrum 8, 34 mTorr of propane is added to the sample chamber, and the conditions are kept constant for the remaining spectra. The addition of a new gas causes the temperature to drop, reaching a minimum of 438 °C before heating back up.

Identifying the general trends in this data is a useful first step to make sense of all this data. If we just consider the elemental composition, after the first 5 spectra, the general composition of the surface is relatively steady, save for a few notable outliers. The 940 eV spectra all show N enrichment relative to the 675 eV spectra. The spectra acquired using a photon energy of 940 eV sample deeper into the surface than those taken using 675 eV, allowing us to probe

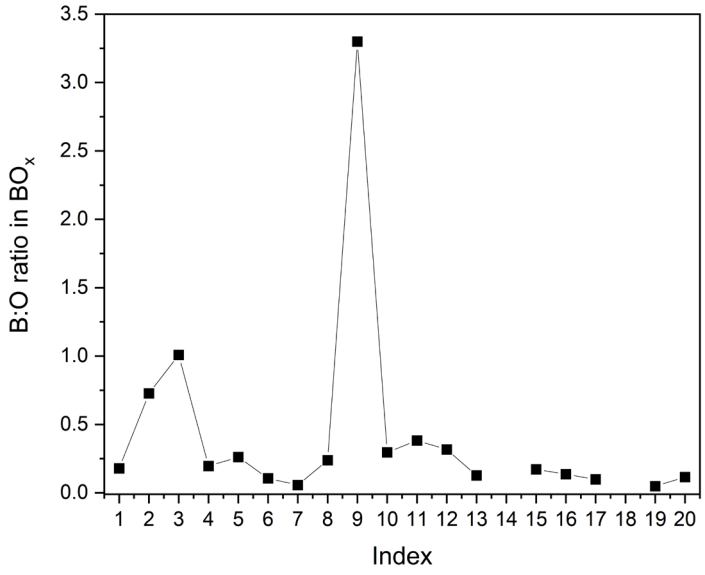

Figure 5.5 Plot of the B:O ratio in the boron oxide phase. Ratio calculated using the factional composition values of the 193 eV and 533 eV peaks.

compositional differences between the near surface and slightly deeper into the material. The N enrichment observed in the 940 eV spectra suggest that boron vacancies are present in the sub-surface hBN layers.

The black box around spectra 5-13 highlights the spectra just before (spectra 5-7) and after propane is added. Notably, spectrum 9 shows a sharp decrease in the amount of oxide that is entirely compensation for by boron. The oxygen compositions rebounds in the next spectrum and remains stable throughout the rest of the experiment. The largest loss of O 1s signal comes from the peak at 533 eV corresponding to boron oxide species. Conversely, the complementary signal for the boron oxide in the B 1s at 193 eV shows a sharp increase. A plot of the boron to oxygen ratio for boron oxide species (*i.e.,* the ratio between the 193 eV and 533 eV peaks, Figure 5.5) shows that the ratio reaches a maximum of *ca.* 3.2, which would generate B_6O_3, a species predicted in the calculated phase diagram of boron oxide on hBN.[18]

The nitrogen content stays relatively steady during this period. However, there is a transient nitrogen species at 400 eV that is only present in the six spectra after propane was added. This transient species is in the chemical shift range of a primary amine.[16] The role of this species in the reaction has not been established.

3.5 Conclusion

The interpretation of this data is ongoing and so the implications of the observed changes are not yet entirely clear. It is clear, however, that more data is needed to understand the complex processes that are happening on the surface of hBN during ODH. The surface response to the addition of propane is a promising result, and in future experiments, repeated dosing of propane should help clarify the changes observed in this study. During our next available beamtime, we will also collect high resolution C 1s spectra to build a more complete picture of the catalytic reaction.

3.6 References

(1) Grant, J. T.; Carrero, C. A.; Goeltl, F.; Venegas, J.; Mueller, P.; Burt, S. P.; Specht, S. E.; McDermott, W. P.; Chieregato, A.; Hermans, I., Selective oxidative dehydrogenation of propane to propene using boron nitride catalysts. *Science (Washington, DC, U. S.)* **2016,** *354* (6319), 1570-1573. 10.1126/science.aaf7885.

(2) Grant, J. T.; McDermott, W. P.; Venegas, J. M.; Burt, S. P.; Micka, J.; Phivilay, S. P.; Carrero, C. A.; Hermans, I., Boron and Boron-Containing Catalysts for the Oxidative Dehydrogenation of Propane. *ChemCatChem* **2017,** *9* (19), 3623-3626. 10.1002/cctc.201701140.

(3) Huang, R.; Zhang, B.; Wang, J.; Wu, K.-H.; Shi, W.; Zhang, Y.; Liu, Y.; Zheng, A.; Schloegl, R.; Su, D. S., Direct Insight into Ethane Oxidative Dehydrogenation over Boron Nitrides. *ChemCatChem* **2017,** *9* (17), 3293-3297. 10.1002/cctc.201700725.

(4) Shi, L.; Wang, D.; Song, W.; Shao, D.; Zhang, W.-P.; Lu, A.-H., Edge-hydroxylated Boron Nitride for Oxidative Dehydrogenation of Propane to Propylene. *ChemCatChem* **2017,** *9* (10), 1788-1793. 10.1002/cctc.201700004.

(5) Love, A. M.; Cendejas, M. C.; Thomas, B.; McDermott, W. P.; Uchupalanun, P.; Kruszynski, C.; Burt, S. P.; Agbi, T.; Rossini, A. J.; Hermans, I., Synthesis and Characterization of Silica-Supported Boron Oxide Catalysts for the Oxidative Dehydrogenation of Propane. *J. Phys. Chem. C* **2019,** *123* (44), 27000-27011. 10.1021/acs.jpcc.9b07429.

(6) Love, A. M.; Thomas, B.; Specht, S. E.; Hanrahan, M. P.; Venegas, J. M.; Burt, S. P.; Grant, J. T.; Cendejas, M. C.; McDermott, W. P.; Rossini, A. J., et al., Probing the Transformation of Boron Nitride Catalysts under Oxidative Dehydrogenation Conditions. *J. Am. Chem. Soc.* **2019,** *141* (1), 182-190. 10.1021/jacs.8b08165.

(7) Lu, W.-D.; Wang, D.; Zhao, Z.; Song, W.; Li, W.-C.; Lu, A.-H., Supported Boron Oxide Catalysts for Selective and Low-Temperature Oxidative Dehydrogenation of Propane. *ACS Catal.* **2019,** *9* (9), 8263-8270. 10.1021/acscatal.9b02284.

(8) Dorn, R. W.; Cendejas, M. C.; Chen, K.; Hung, I.; Altvater, N. R.; McDermott, W. P.; Gan, Z.; Hermans, I.; Rossini, A. J., Structure Determination of Boron-Based Oxidative Dehydrogenation Heterogeneous Catalysts With Ultrahigh Field 35.2 T 11B Solid-State NMR Spectroscopy. *ACS Catal.* **2020,** *10* (23), 13852-13866. 10.1021/acscatal.0c03762.

(9) Patel, D. I.; Roychowdhury, T.; Jain, V.; Shah, D.; Avval, T. G.; Chatterjee, S.; Bahr, S.; Dietrich, P.; Meyer, M.; Thißen, A., et al., Introduction to near-ambient pressure x-ray photoelectron spectroscopy characterization of various materials. *Surface Science Spectra* **2019,** *26* (1), 016801. 10.1116/1.5109118.

(10) van der Heide, P., Introduction. In *X-Ray Photoelectron Spectroscopy*, Wiley: 2011; pp 1-12.

(11) Zhu, W.; Gao, X.; Li, Q.; Li, H.; Chao, Y.; Li, M.; Mahurin, S. M.; Li, H.; Zhu, H.; Dai, S., Controlled Gas Exfoliation of Boron Nitride into Few-Layered Nanosheets. *Angewandte Chemie International Edition* **2016,** *55* (36), 10766-10770. https://doi.org/10.1002/anie.201605515.

(12) Trehan, R.; Lifshitz, Y.; Rabalais, J. W., Auger and x-ray electron spectroscopy studies of hexagonal and cubic boron nitride and nitrogen(N2+) ion irradiation of boron and boron nitride. *J. Vac. Sci. Technol., A* **1990,** *8* (6), 4026-32. 10.1116/1.576471.

(13) Mezentzeff, P.; Lifshitz, Y.; Rabalais, J. W., Boron nitride formation from bombardment of boron with nitrogen ion (N2+). *Nucl. Instrum. Methods Phys. Res., Sect. B* **1990,** *B44* (3), 289-95. 10.1016/0168-583X(90)90641-7.

(14) Il'inchik, E. A.; Volkov, V. V.; Mazalov, L. N., X-ray photoelectron spectroscopy of boron compounds. *J. Struct. Chem.* **2005,** *46* (3), 523-534. 10.1007/s10947-006-0133-y.

(15) Liu, Q.; Chen, C.; Du, M.; Wu, Y.; Ren, C.; Ding, K.; Song, M.; Huang, C., Porous Hexagonal Boron Nitride Sheets: Effect of Hydroxyl and Secondary Amino Groups on Photocatalytic Hydrogen Evolution. *ACS Applied Nano Materials* **2018,** *1* (9), 4566-4575. 10.1021/acsanm.8b00867.

(16) Bachmann, P.; Duell, F.; Spaeth, F.; Bauer, U.; Steinrueck, H.-P.; Papp, C., A HR-XPS study of the formation of h-BN on Ni(111) from the two precursors, ammonia borane and borazine. *J. Chem. Phys.* **2018,** *149* (16), 164709/1-164709/7. 10.1063/1.5051595.

(17) Moddeman, W. E.; Burke, A. R.; Bowling, W. C.; Foose, D. S., Surface oxides of boron and B12O2 as determined by XPS. *Surface and Interface Analysis* **1989,** *14* (5), 224-232. https://doi.org/10.1002/sia.740140503.

(18) Zhang, Z.; Jimenez-Izal, E.; Hermans, I.; Alexandrova, A. N., Dynamic Phase Diagram of Catalytic Surface of Hexagonal Boron Nitride under Conditions of Oxidative Dehydrogenation of Propane. *J. Phys. Chem. Lett.* **2019,** *10* (1), 20-25. 10.1021/acs.jpclett.8b03373.

CHAPTER 6

Summary and Future Directions

Chapter 6: Summary and Future Directions

When I started my PhD in 2016, the group had just published our initial findings on the catalytic activity of hBN. Since then, my research efforts have focused on trying to understand the structure and role of the surface during catalysis. While we still do not have a definitive picture of the surface, I have described tools and approaches that can help us probe the role of the surface during the catalytic reaction. The conclusions from my research presented in earlier chapters are restated below, followed by suggestions for future studies on this system.

6.1 Summary of Conclusions

Controlled Grafting Synthesis

A combination of transmission FTIR and solid-state NMR spectroscopies revealed that the grafting of HBpin onto SiO_2 generates isolated, monopodally grafted Bpin (B-O-Si bond to the silica surface) that can form hydrogen bonds with nearby unreacted silanol groups. The number of neighboring hydrogen-bonded silanol species can be decreased with increased silica thermal treatment temperature, enabling high controllability of the local chemical environment surrounding the isolated, singly anchored Bpin molecule. However, the control over surface speciation is lost during the thermal treatment of Bpin/$SiO_{2(T)}$ materials, as a similar boron oxide/hydroxide phase is observed for all catalysts. The observation of similar boron species, especially for S9, which contained ~ 0.18 wt. % B and exhibited highly isolated grafted Bpin before thermal treatment, illustrates that boron oxide/hydroxide is highly mobile on the SiO_2 surface and is able to generate clustered boron oxide/hydroxide under thermal treatment conditions. Modification of thermal treatment conditions, chemically treating the surface before or after grafting, and/or doping the silica surface could potentially enable better control over the species formed on the silica surface by reducing boron oxide/hydroxide mobility.

The catalytic activity of Bpin/$SiO_{2(T)}^{-500v}$ materials is typical for silica-supported boron oxide catalysts previously reported.[19, 21] Because these materials of different boron weight loadings

contained similar boron speciation, we were able to probe the effect of boron content on catalytic activity. We observed the highest propylene productivity per mole of boron in the S9 material, consistent with the presence of boron oxide/hydroxide particles. Additionally, we observed the loss of productivity at increased conversions for all catalysts. More thorough kinetic studies are needed to understand this observation in terms of the proposed reaction mechanism.

Operando X-ray Raman Spectroscopy (XRS)

We observed the formation of the boron oxide phase on hBN during the induction period of the propane ODH reaction. We found that the oxide gradually grows in over the course of reaction, eventually reaching a steady composition. This study is the first direct observation of the surface changes that occur during the induction period. While these results are expected, they demonstrate the power XRS has in observing this system, allowing us to design experiments that can answer lingering questions.

In Situ Near Ambient Pressure X-ray Photoelectron Spectroscopy (NAP-XPS)

The interpretation of this data is ongoing and so the implications of the observed changes are not yet entirely clear. It is clear, however, that more data is needed to understand the complex processes that are happening on the surface of hBN during ODH. The surface response to the addition of propane is a promising result, and in future experiments, repeated dosing of propane should help clarify the changes observed in this study. During our next available beamtime, we will also collect high resolution C 1s spectra to build a more complete picture of the catalytic reaction.

6.2 Future Directions

With the Bpin/$SiO_{2(T)}$-500v materials, the loss of productivity at higher conversions indicates that the surface is likely limiting the rate of reaction, supporting our hypothesis that active site regeneration is kinetically slow. This behavior, which is unique to silica-supported materials, can be leveraged to further probe our mechanistic hypotheses. Specifically, we have proposed a water-assisted dehydration of the surface as the regeneration step; co-feeding a small amount of

water into the reactor with Bpin/$SiO_{2(T)}$-500v should prevent or lessen the loss of productivity at higher conversions. However, boron leaching by hydrolysis will be a concern in this experiment but might offer some additional insights as to the amount of boron that can be stabilized on the active catalyst surface. Along the same vein, the S200 and S700 materials showed the same boron loading after reaction. A longer time-on-stream experiment with these materials should shed some additional light onto the amount of boron that can be stabilized.

Our application of XRS and NAP-XPS is in its infancy, and the list of experiments I want to perform on this system is long. Apparent in our initial studies is that the surface is highly sensitive to perturbations of the gas composition. Based on this observation, repeating propane dosing in NAP-XPS will confirm our initial result and help elucidate the complex surface chemistry. These NAP-XPS results can be coupled with calculations on our established structural model of boron oxide supported on hBN that has been used in previous studies and will help elucidate the dynamics early in the reaction as well as the fate of nitrogen in this system, which has not been thoroughly investigated.

With XRS, expanding our studies to other bulk boron-based materials, such as boron carbide and metal borides, will allow us to establish a more generalized picture of the catalytic surface. Additionally, I hypothesize that the rate of oxidation during the induction period is related to the steady-state rate of propane consumption. XRS can be used to probe this hypothesis. Switching the on-line analytical tool from mass spectrometry to a micro-GC will allow for better investigations of the kinetics of the reaction and will be pivotal in connecting spectroscopy to our studies of reaction kinetics.

In conclusion, the silica-supported materials, which are slightly worse catalysts than hBN, can be used to further probe surface dynamics. NAP-XPS and XRS are powerful tools that can reveal surface changes upon perturbations of the gas composition.

Appendix A

Supporting Information for Chapter 3

Controlled Grafting Synthesis of Silica-Supported Boron for Oxidative Dehydrogenation Catalysis

Appendix A: Supporting Information for Chapter 3

Controlled Grafting Synthesis of Silica-Supported Boron for Oxidative Dehydrogenation Catalysis

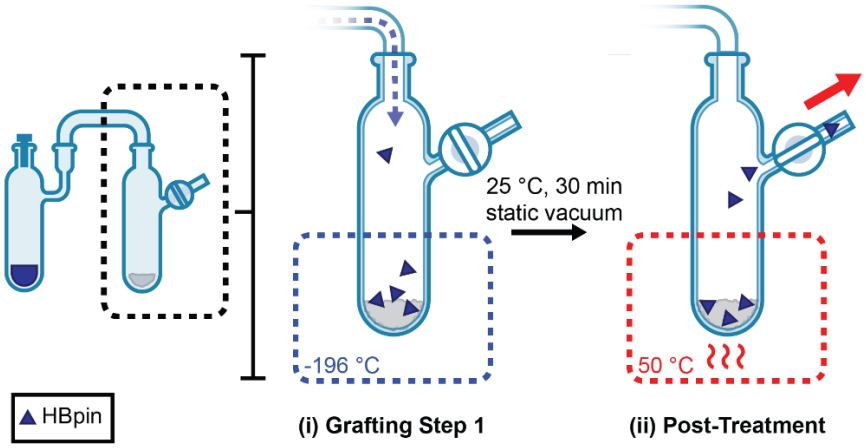

Figure S1. Cartoon depicting the gas phase grafting process. HBpin is transferred in the gas phase under static vacuum into a liquid N_2-cooled Schlenk flask containing thermally treated silica. The transfer step is followed by a 30-minute reaction period at room temperature. Finally, the material is post-treated at 50 °C under dynamic vacuum to remove any unreacted precursor.

Table S1. Experimental solid-state NMR spectroscopy parameters.

Figure	Expt.	B_0 (T)	MAS (kHz)	# of Scans	Recycle Delay (s)	t_1 TD	Dt_1 (ms)	Rec. Duration (ms)[a]	Total Expt. Time (h)[b]
2A	^{11}B spin echo	9.4[c]	10	1024	1	-	-	-	0.3
2B (upper)	^{11}B spin echo	11.7	10	1024	0.5	-	-	-	0.1
2B (middle)	^{11}B spin echo	11.7	12	6144	0.5	-	-	-	0.9

2B (lower)	^{11}B spin echo	11.7	10	1024	0.5	-	-	-	0.1
3B (left)	^{1}H DQ-SQ	14.1	25	32	1	256	40	0.095	2.3
3B (middle)	^{1}H DQ-SQ	14.1	25	64	1	256	40	0.095	4.6
3B (right)	^{1}H DQ-SQ	14.1	25	16	1	320	40	0.095	1.4
3C (left)	^{11}B→^{1}H D-RINEPT	14.1	25	256	0.5	52	80	2.88	1.8
3C (middle)	^{1}H{^{11}B} TONE DHMQC-3	14.1	25	256	1	78	80	1.92	5.5
3C (right)	^{1}H{^{11}B} TONE DHMQC-3	14.1	25	128	1	78	80	3.84	2.8
4A (left)	^{11}B→^{1}H D-RINEPT	14.1	25	512	0.5	64	80	2.88	4.6
4A (right)	^{11}B spin echo	14.1	25	176	100[d]	-	-	-	4.9
4B (left)	^{11}B→^{1}H D-RINEPT	14.1	25	1024	0.3	64	80	2.88	5.5
4B (right)	^{11}B spin echo	14.1	25	512	17.5[d]	-	-	-	2.5
4C (left)	^{11}B→^{1}H D-RINEPT	14.1	25	768	0.25	64	80	2.88	3.4
4C (right)	^{11}B spin echo	14.1	25	1024	10[d]	-	-	-	2.8
5 (blue)	^{1}H DEPTH	14.1	25	16	75[d]	-	-	-	0.3
5 (blue), S9	^{1}H{^{29}Si} CP-HETCOR	14.1	25	32	19.5	88	40	5 (forward and back)	15.3
5 (blue), S11 (left)	^{1}H DQ-SQ	14.1	25	16	7	48	40	0.095	1.5
5 (orange)	^{1}H DEPTH	14.1	25	128	20[d]	-	-	-	0.7
5 (orange), S11 (middle)	^{1}H DQ-SQ	14.1	25	32	5	160	40	0.095	7.1
5 (green)	^{1}H DEPTH	14.1	25	32	70[d]	-	-	-	0.6

5 (green), S11 (right)	^{1}H DQ-SQ	14.1	25	16	5	160	40	0.095	3.6
7 (upper, dashed)	^{11}B spin echo	14.1	25	11520	1[d]	-	-	-	3.2
7 (middle, dashed)	^{11}B spin echo	14.1	25	12288	1[d]	-	-	-	3.4
7 (lower, dashed)	^{11}B spin echo	14.1	25	8192	2[d]	-	-	-	4.6
S4	^{1}H{^{29}Si} CPMAS	14.1	25	3072	1.3	-	-	5 (forward and back)	1.1
S5 (upper)	^{1}H DEPTH	14.1	25	16	5[d]	-	-	-	0.02
S5 (middle)	^{1}H DEPTH	14.1	25	256	5[d]	-	-	-	0.4
S5 (lower)	^{1}H DEPTH	14.1	25	128	5[d]	-	-	-	0.2
S8 (upper, left)	^{11}B→^{1}H D-RINEPT	14.1	25	256	0.5	64	80	0.96	2.3
S8 (upper, middle)	^{11}B→^{1}H D-RINEPT	14.1	25	512	0.3	64	80	0.96	2.7
S8 (upper, right)	^{11}B→^{1}H D-RINEPT	14.1	25	512	0.25	64	80	0.96	2.3
S10 (upper, red)	^{11}B DQ-SQ	11.7	14	14127	4	-	-	0.571	15.7
S10 (upper, black)	^{11}B spin echo	11.7	14	1024	4	-	-	-	1.1
S10 (middle, red)	^{11}B DQ-SQ	11.7	14	99536	0.5	-	-	0.571	13.8
S10 (middle, black)	^{11}B spin echo	11.7	14	12288	0.5	-	-	-	1.7
S10 (lower, red)	^{11}B DQ-SQ	11.7	14	16170	4	-	-	0.571	18.0
S10 (lower, black)	^{11}B spin echo	11.7	14	2048	4	-	-	-	2.3

S13 A	$^{11}B \rightarrow {}^{1}H$ D-RINEPT	14.1	25	1536	0.25	64	40	0.96	6.8
S13 B	$^{11}B \rightarrow {}^{1}H$ D-RINEPT	14.1	25	1536	0.25	64	40	3.2	6.8
S13 C	$^{11}B \rightarrow {}^{1}H$ D-RINEPT	14.1	25	2560	0.25	60	40	0.96	10.7
S13 D	$^{11}B \rightarrow {}^{1}H$ D-RINEPT	14.1	25	3072	0.25	60	40	1.92	12.8
S13 E	$^{11}B \rightarrow {}^{1}H$ D-RINEPT	14.1	25	3072	0.25	52	40	0.96	11.1
S13 F	$^{11}B \rightarrow {}^{1}H$ D-RINEPT	14.1	25	4096	0.25	52	40	1.92	14.8
S15 B (blue)	^{1}H DEPTH	14.1	25	64	20[d]	-	-	-	0.4
S15 B (blue)	^{1}H DQ-SQ	14.1	25	256	4.8	-	-	0.095	0.3
S15 B (orange)	^{1}H DEPTH	14.1	25	64	40[d]	-	-	-	0.7
S15 B (orange)	^{1}H DQ-SQ	14.1	25	512	1	-	-	0.095	0.1
S15 B (green)	^{1}H DEPTH	14.1	25	32	50[d]	-	-	-	0.4
S15 B (green)	^{1}H DQ-SQ	14.1	25	512	1	-	-	0.095	0.1

[a]Total duration of dipolar recoupling or CP. [b]Experimental times only include recycle delay, number of scans and t_1 TD points. Other parameters (e.g., pre-saturation, dipolar recoupling, etc.) are not included. [c]Sample temperature was 100 K. [d]Recycle delay ≥ 5 × T_1.

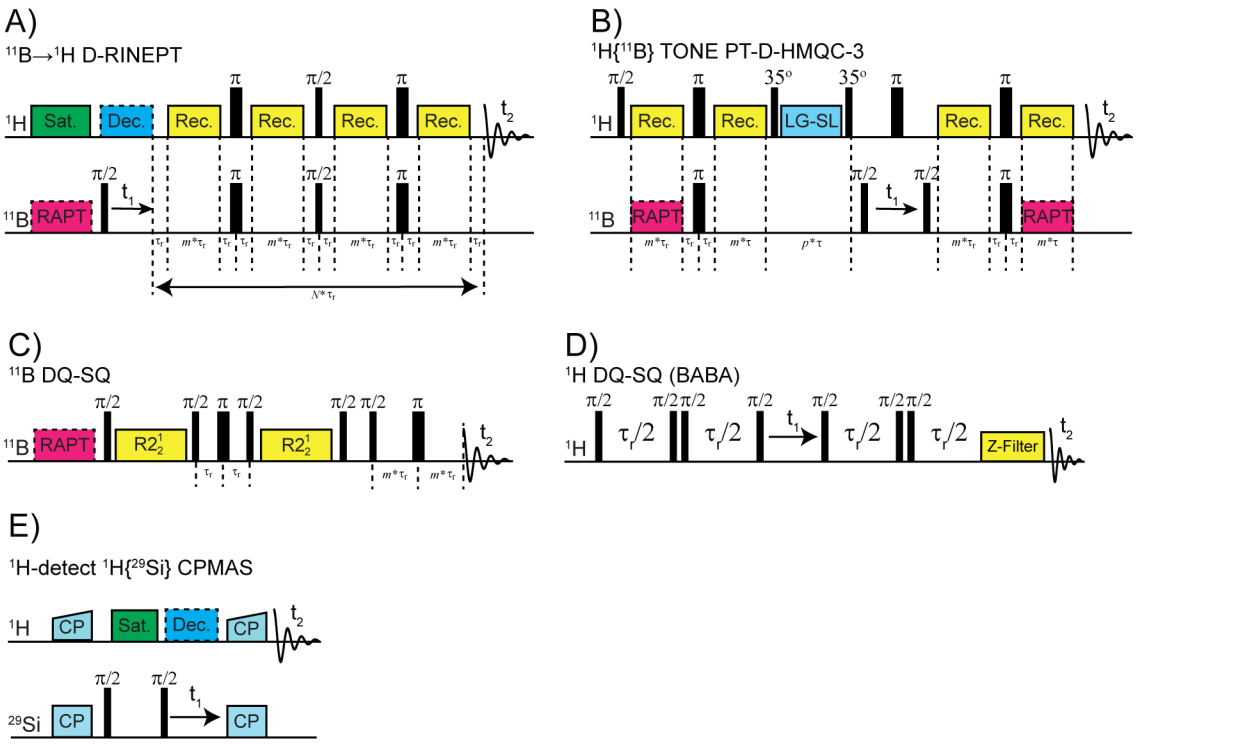

Figure S2. Schematic illustration of (A) ^{11}B→^{1}H D-RINEPT[1-2], (B) ^{1}H{^{11}B} TONE PT-D-HMQC-3,[3] (C) ^{11}B DQ-SQ,[4-5], (D) ^{1}H DQ-SQ,[6-7] and (E) ^{1}H-detect ^{1}H{^{29}Si} CPMAS[8-9] pulse sequences.

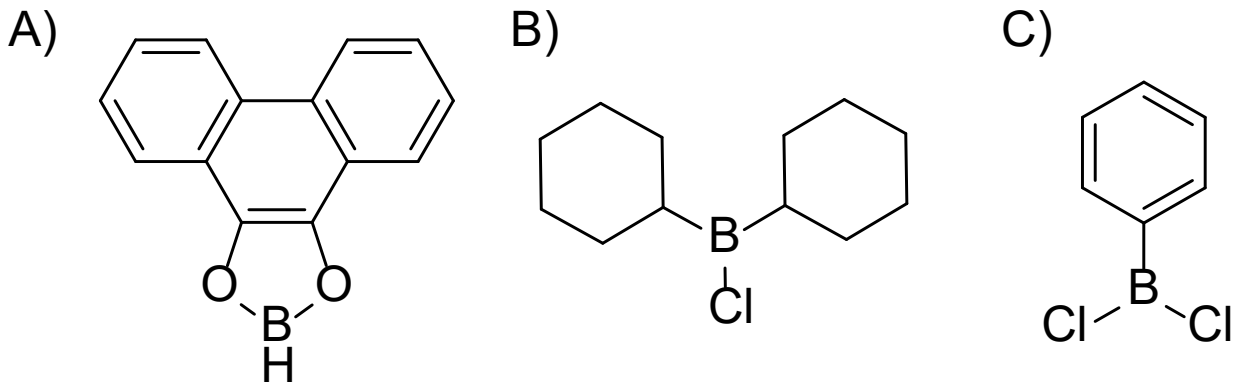

Figure S3. Structure of A) phenanthrene dioxoborane precursor used by Mathey, *et al,*[10] as well as B) chlorodicyclohexylborane, and C) dichlorophenylborane, both used by Agarwala, *et al.*[11]

Table S2. Boron weight loading and BET surface area for each Bpin/$SiO_{2(T)}$-^{500v} sample.

	Initial Isolated Silanol content[a] (OH/nm^2)	Calculated B loading[b] (wt. %)	Boron loading, Fresh[c] (wt. %)	BET Surface Area (m^2/g)	Boron loading, Spent (wt. %)
Bpin/$SiO_{2(200)}$-^{500v}	1.2	0.65	1.56 ± 0.01	246.00	0.33 ± 0.01
Bpin/$SiO_{2(700)}$-^{500v}	0.9	0.48	0.81 ± 0.01	271.22	0.32 ± 0.01
Bpin/$SiO_{2(900)}$-^{500v}	0.4	0.22	0.18 ± 0.01	251.90	N.D.[d]
Bpin/TMS-$SiO_{2(700)}$	0	-	0.56 ± 0.01	-	-

[a] From Ref. 2[12] [b] Assuming reaction only with isolated silanol groups. [c] Determined by ICP-MS. [d] Boron content could not be determined.

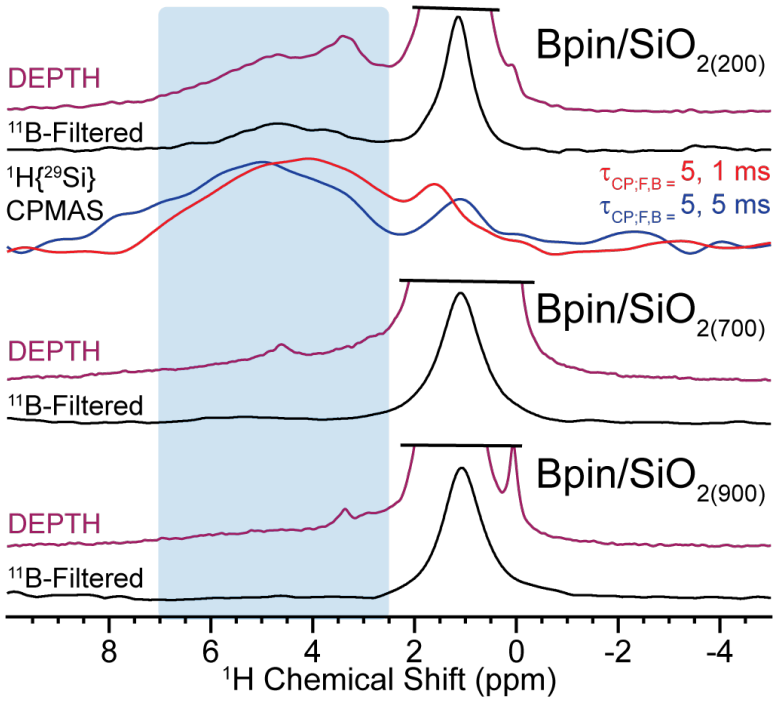

Figure S4. Comparison of ^{1}H NMR spectra of (top to bottom) Bpin/SiO$_{2(200)}$, Bpin/SiO$_{2(700)}$ and Bpin/SiO$_{2(900)}$. ^{1}H spectra were recorded either through (purple) direct excitation, (black) ^{1}H-^{11}B HETCOR or (blue and red) ^{1}H{^{29}Si} CPMAS experiment. The specific experiment is listed above each spectrum. The highlight blue region indicates hydrogen bonded silanol (Si-O**H**) ^{1}H NMR signals.

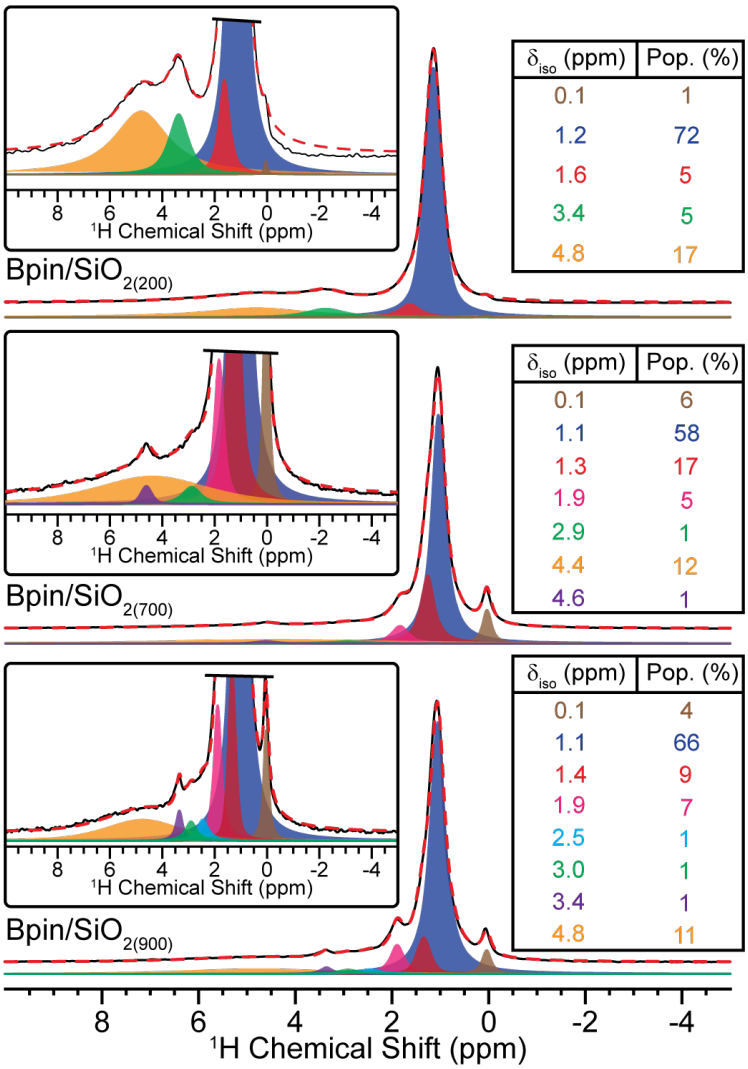

Figure S5. Quantitative (recycle delay ≥ 5 × T_1) direct excitation (DEPTH) ^{1}H NMR spectra of (top to bottom) Bpin/$SiO_{2(200)}$, Bpin/$SiO_{2(700)}$ and Bpin/$SiO_{2(900)}$. The black (solid) and red (dashed) lines correspond to the experimental and analytically simulated spectra, respectively. The isotropic chemical shift (d_{iso}) and relatively population of each species in the analytical fits is given next to the right of each spectrum.

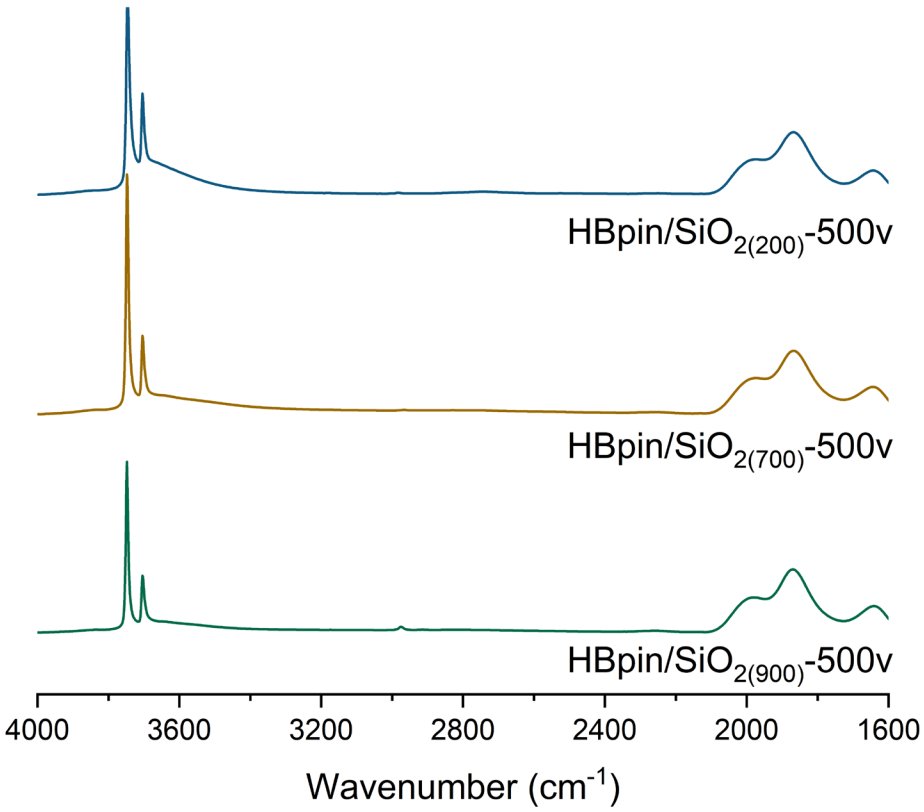

Figure S6. Transmission FTIR of the thermally treated Bpin/$SiO_{2(T)}$-500v materials. All spectra are normalized to the Si-O-Si overtone signal at *ca.* 1870 cm^{-1}.

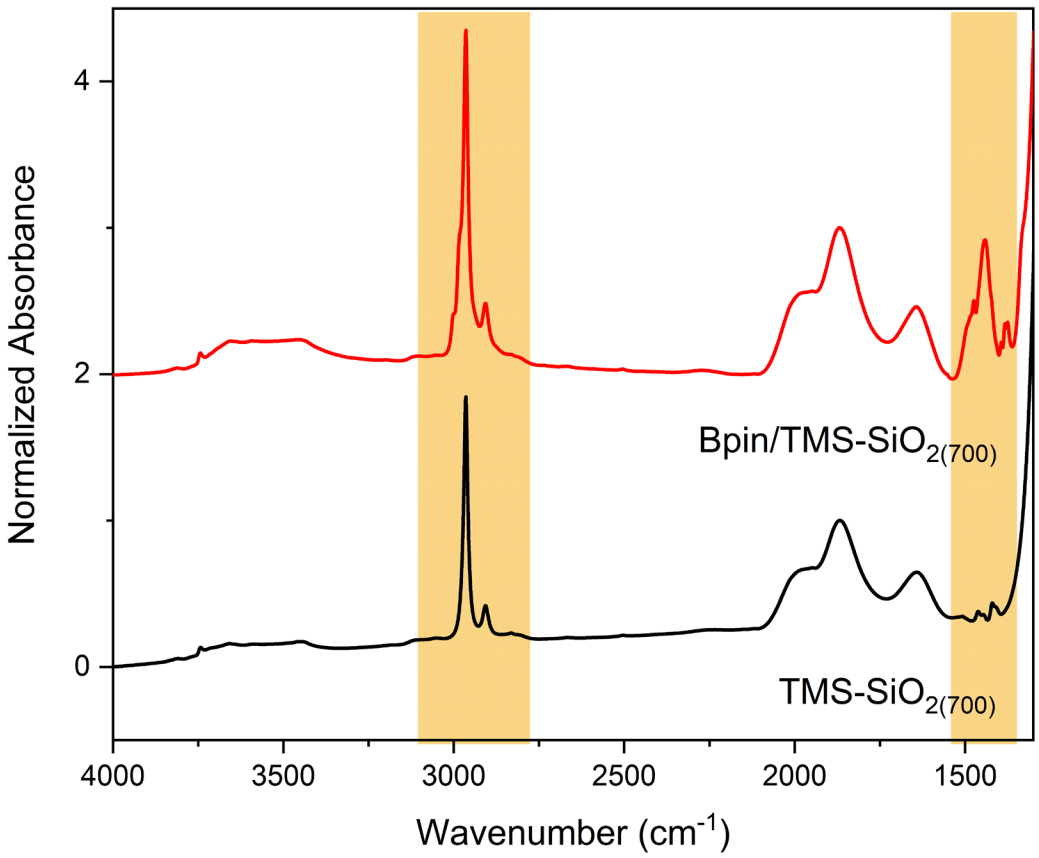

Figure S7. IR spectra of silylated SiO_2 (TMS-$SiO_{2(700)}$) and Bpin grafted to TMS-$SiO_{2(700)}$.

Table S3. ^{11}B solid-state NMR spectra analytical simulation fitting parameters of the fresh and spent Bpin/SiO_2 catalysts.

Species [a]	δ_{iso} (ppm)	C_Q (MHz)	Fresh Population (%)	Spent Population (%)
		Bpin/S2		
B($OSi)_4$	− 0.9 (0.5) [b]	1.0	8	10
B$(OSi)_3$	9.5	2.3	13	8
B$(OB)(OSi)_2$	12.0	2.3	25	31
B$(OB/H)_2(OSi)$	14.9	2.2	29	27
B$(OB/H)_3$	16.9	2.2	24	24
		Bpin/S7		
B($OSi)_4$	− 1.2 (0.0) [b]	0.5	12	14
B$(OSi)_3$	10	2.3	10	21
B$(OB)(OSi)_2$	12	2.2	29	20
B$(OB/H)_2(OSi)$	15	2.2	32	30
B$(OB/H)_3$	18.3	2.4	17	15
		Bpin/S9		
B($OSi)_4$	− 0.1	0.5	12	23
B$(OSi)_3$	9.5	2.3	10	13
B$(OB)(OSi)_2$	12	2.2	17	27
B$(OB/H)_2(OSi)$	15	2.2	33	30
B$(OB/H)_3$	18.8	2.5	27	8

[a]Species with “OB/H” indicate that the O atoms bonded to the central B atom is bonded to either a B or H atom. [b]d_{iso} given in parentheses is for the spent catalysts.

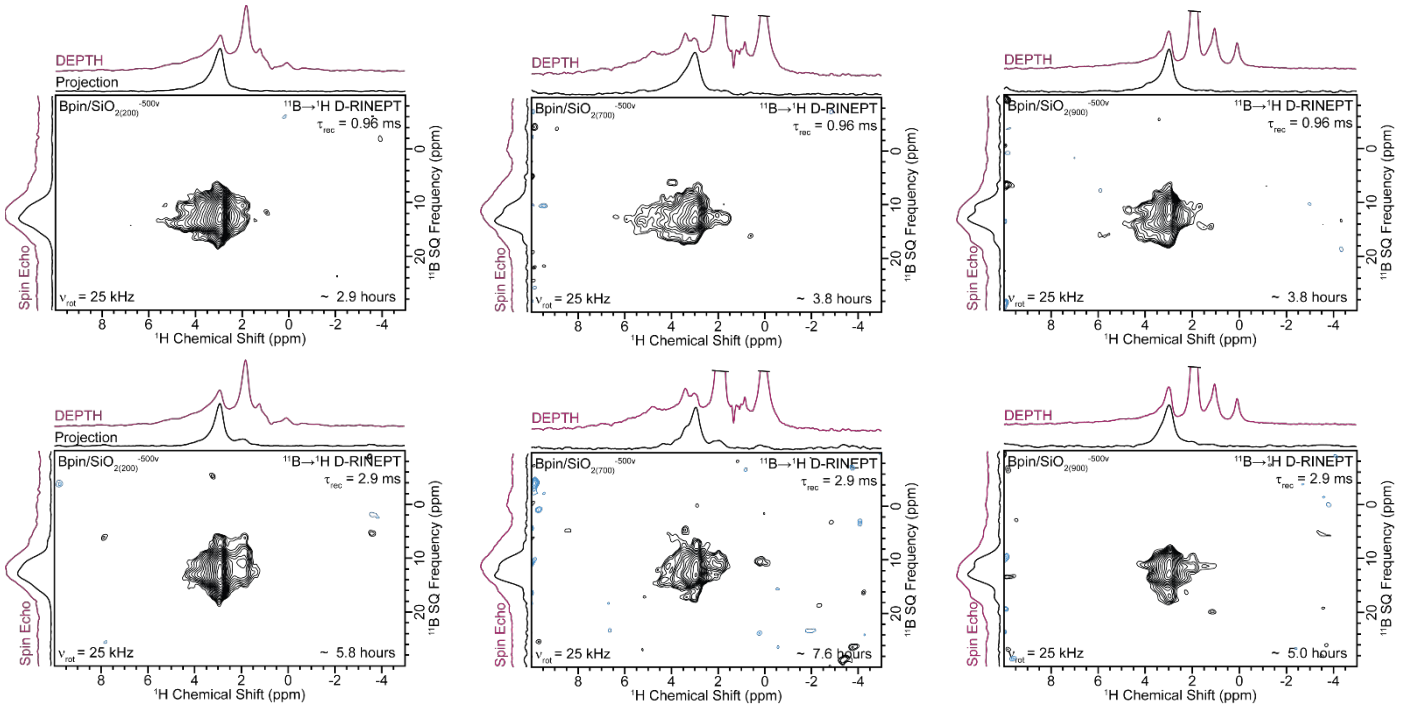

Figure S8. 2D $^{11}B \rightarrow {}^{1}H$ D-RINEPT spectra of (left to right) Bpin/$SiO_{2(200,\ 700,\ 900)}$-500v recorded with either (upper) 0.96 ms or (lower) 2.9 ms of total $SR4_1^2$ heteronuclear dipolar recoupling applied to the ^{1}H spins. Direct excitation (DEPTH) ^{1}H and (spin echo) ^{11}B spectra are overlaid above the 2D projections. All spectra were recorded at B_0 = 14.1 T with 25 kHz MAS.

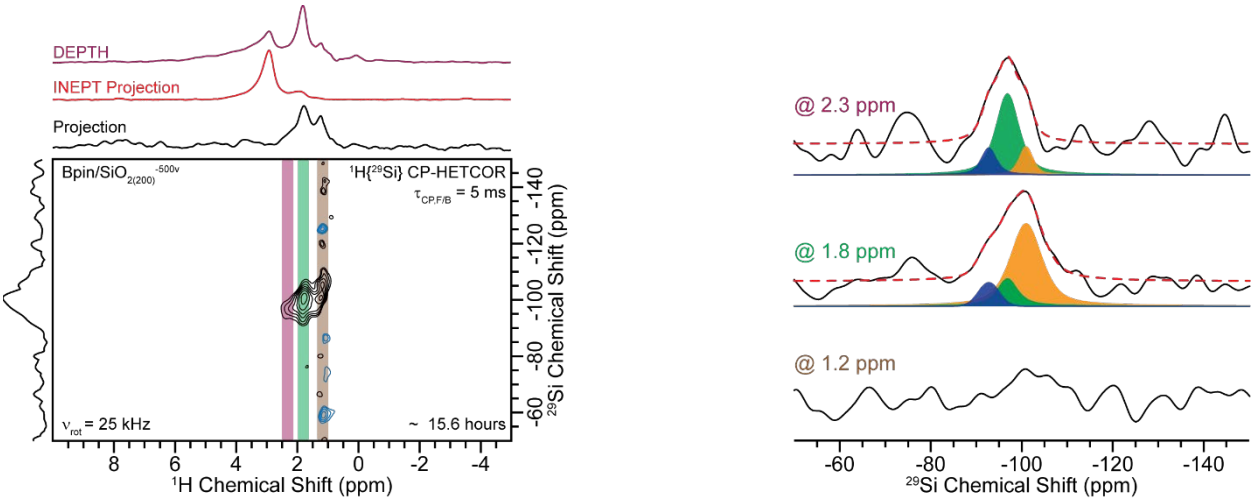

Figure S9. (Left) 2D $^{1}H\{^{29}Si\}$ CP-HETCOR spectrum of $Bpin/SiO_{2(200)}^{-500v}$ recorded with a 5 ms forward and backward CP contact time. (Right) ^{29}Si slices from the 2D spectra at ^{1}H shifts of (top to bottom) 2.3, 1.8 or 1.2 ppm.

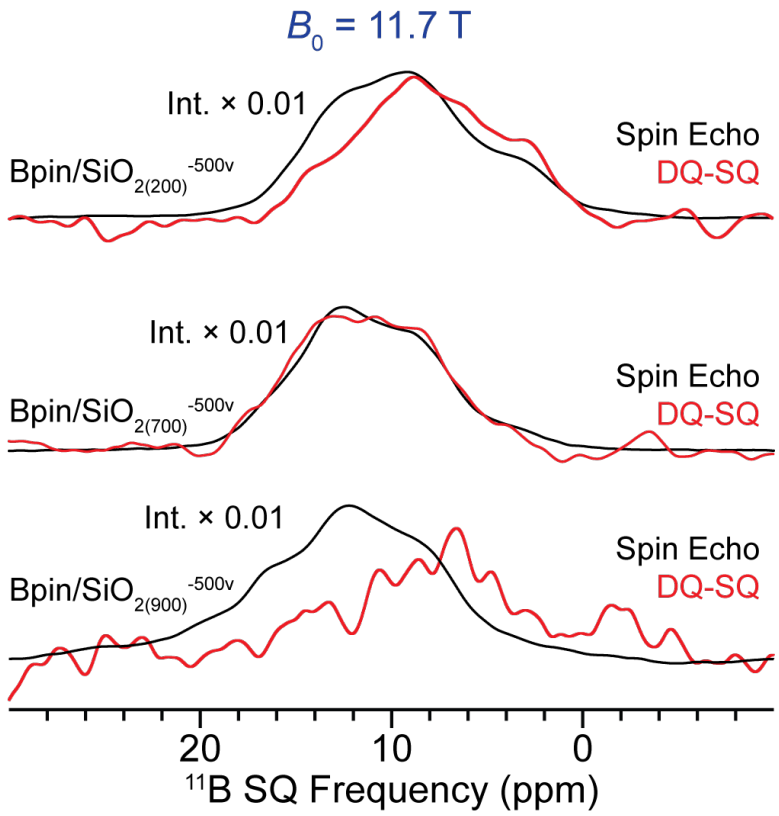

Figure S10. 1D (red) ^{11}B dipolar DQ-SQ spectra of (upper to lower) Bpin/$SiO_{2(200,\ 700,\ 900)}$$^{-500v}$ overlaid on (black) ^{11}B spin echo spectra. All spectra were recorded at B_0 = 11.7 T and with same relative parameters. The spin echo spectra intensities were scaled by 10 %.

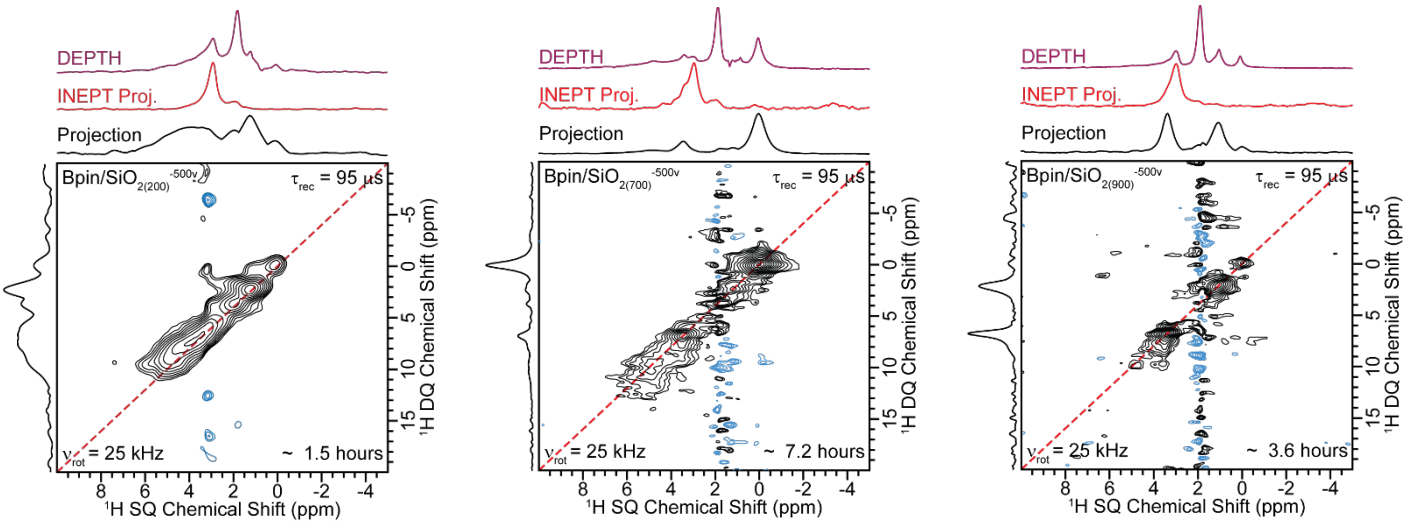

Figure S11. 2D ^{1}H dipolar DQ-SQ NMR spectra of (left to right) Bpin/$SiO_{2(200,\ 700,\ 900)}^{-500v}$ recorded at B_0 = 14.1 T with 25 kHz MAS.

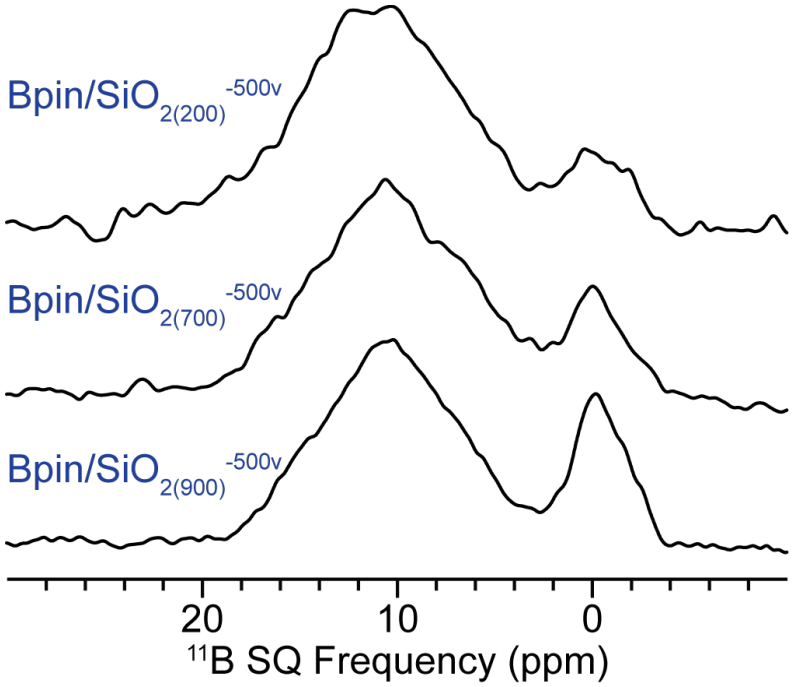

Figure S12. Comparison of 1D ^{11}B spin echo NMR spectra of spent (upper) Bpin/$SiO_{2(200)}^{-500v}$, (middle) Bpin/$SiO_{2(700)}^{-500v}$ and (lower) Bpin/$SiO_{2(900)}^{-500v}$ catalysts recorded at B_0 = 14.1 T with 25 kHz MAS.

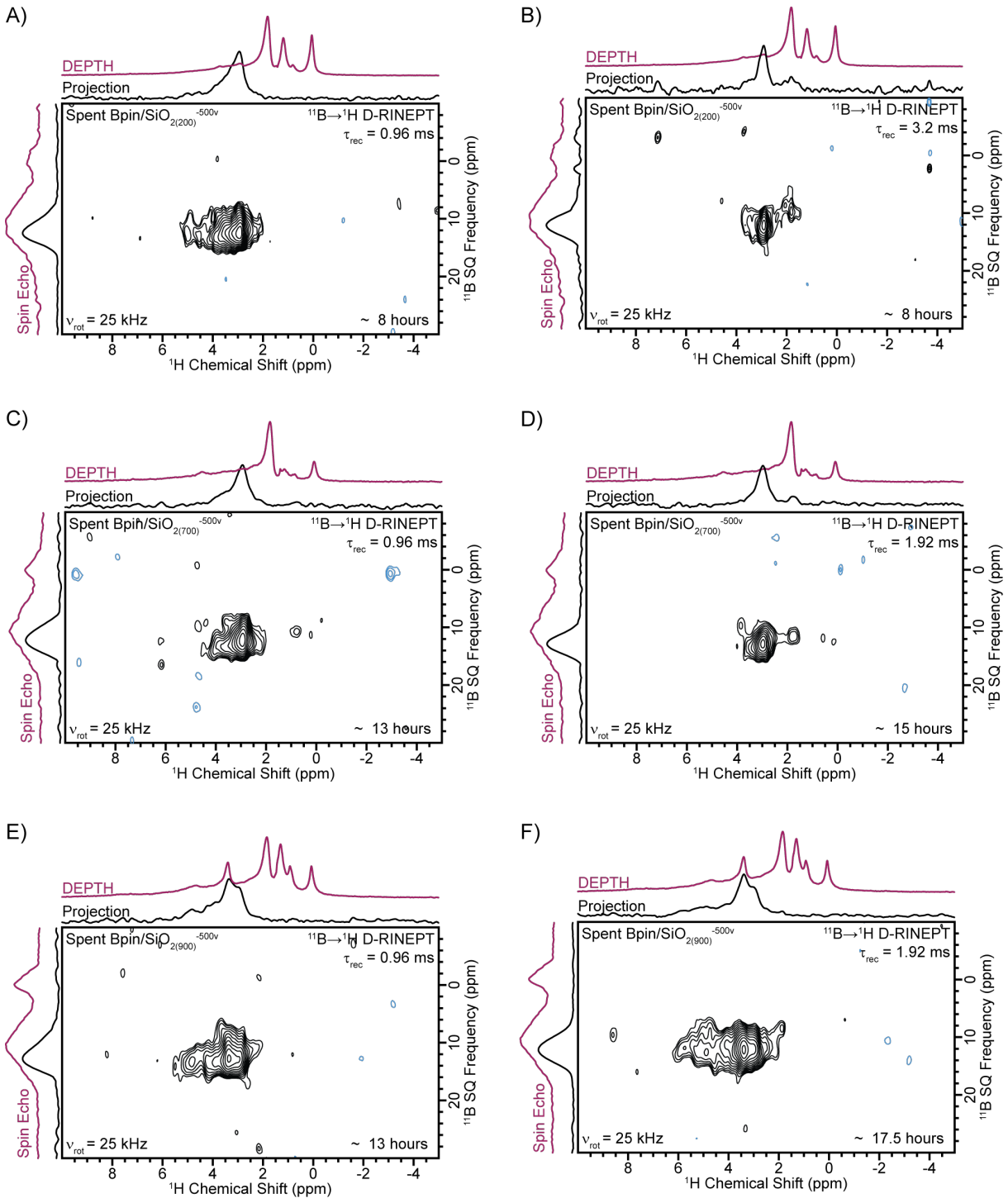

Figure S13. 2D $^{11}B \rightarrow {}^{1}H$ D-RINEPT spectra of spent (A, B) Bpin/$SiO_{2(200)}$-^{500v}, (C, D) Bpin/$SiO_{2(700)}$-^{500v} and (E, F) Bpin/$SiO_{2(900)}$-^{500v} recorded at B_0 = 14.1 T with 25 kHz MAS and either (A, C, E)

0.96 ms, (D, F) 1.92 ms or (B) 3.2 ms of total $SR4_1^2$ heteronuclear dipolar recoupling applied to the ^{1}H spins.

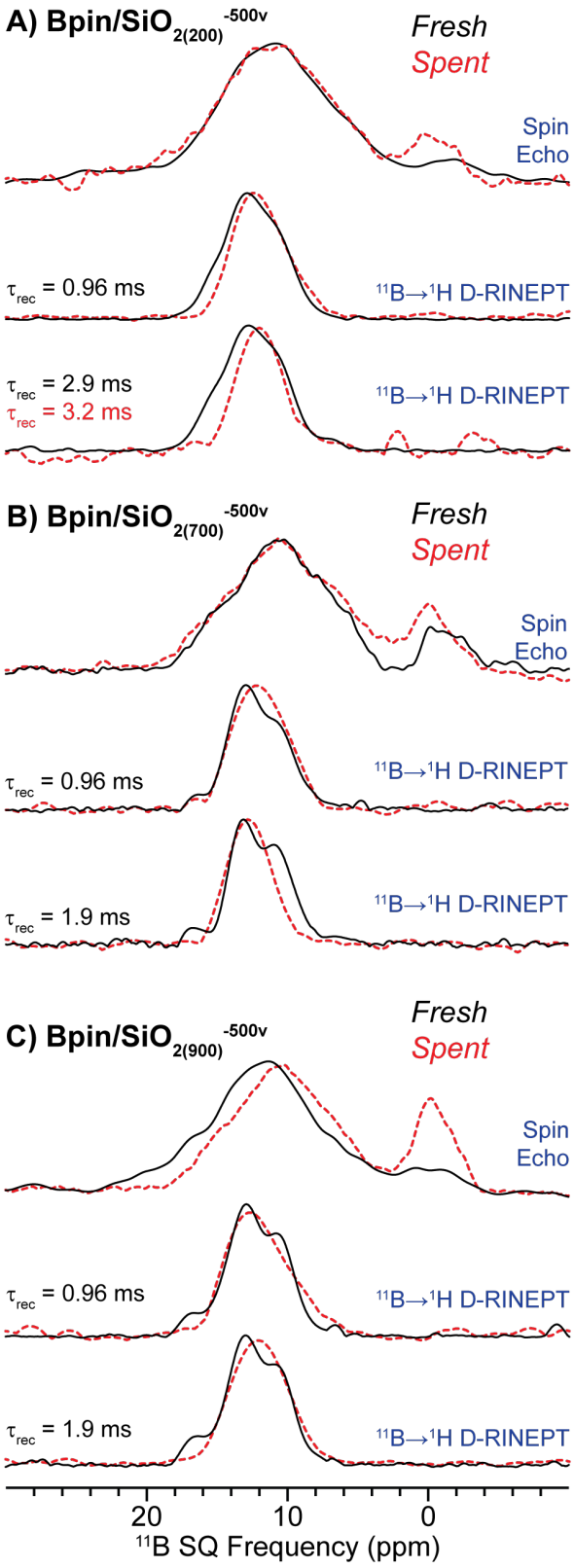
A) Bpin/SiO2(200) -500v
Fresh
Spent
Spin Echo
τrec = 0.96 ms
11B→1H D-RINEPT
τrec = 2.9 ms
τrec = 3.2 ms
11B→1H D-RINEPT
B) Bpin/SiO2(700) -500v
Fresh
Spent
Spin Echo
τrec = 0.96 ms
11B→1H D-RINEPT
τrec = 1.9 ms
11B→1H D-RINEPT
C) Bpin/SiO2(900) -500v
Fresh
Spent
Spin Echo
τrec = 0.96 ms
11B→1H D-RINEPT
τrec = 1.9 ms
11B→1H D-RINEPT
20
10
0
11B SQ Frequency (ppm)

Figure S14. Comparison of $^{11}B \rightarrow {}^{1}H$ D-RINEPT ^{11}B projections for the (black, solid) fresh and (red, dashed) spent catalysts.

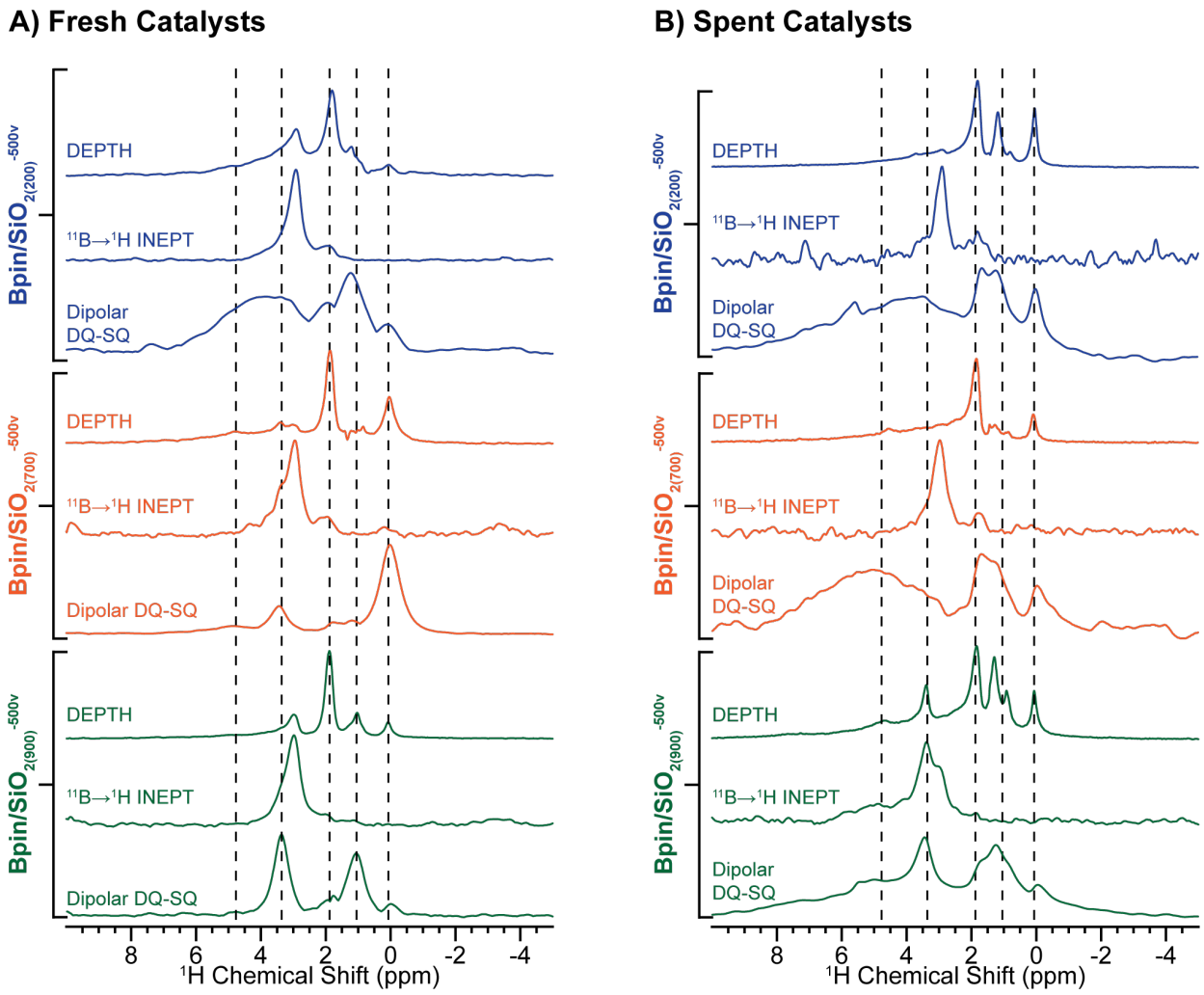

Figure S15. Comparison of ^{1}H NMR spectra, direct excitation (DEPTH), ^{11}B→^{1}H D-RINEPT and ^{1}H dipolar DQ-SQ, of (A) fresh and (B) spent (blue, upper) Bpin/$SiO_{2(200)}$-^{500v}, (orange, middle) Bpin/$SiO_{2(700)}$-^{500v} and (green, lower) Bpin/$SiO_{2(900)}$-^{500v} catalysts. The exact experiment is given above each spectrum. All spectra were recorded at B_0 = 14.1 T with 25 kHz MAS.

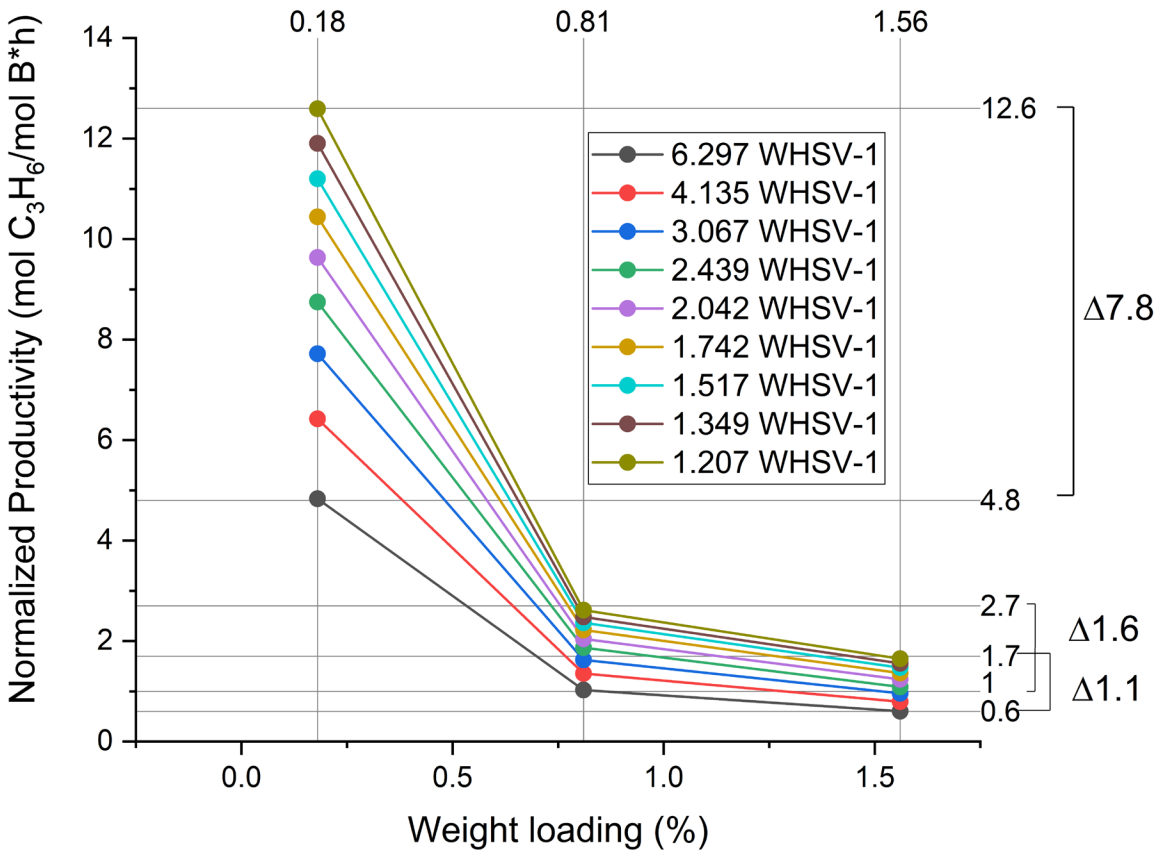

~60-65 % loss of productivity per mol B between highest and lowest conversion levels

Figure S16. Propylene productivity normalized per mole of boron in each catalyst material. The different color dots indicate the different contact times used in the experiments.

References

(1) Trebosc, J.; Hu, B.; Amoureux, J. P.; Gan, Z., Through-Space R3-HETCOR Experiments between Spin-1/2 and Half-Integer Quadrupolar Nuclei in Solid-State NMR. *Journal of Magnetic Resonance* **2007,** *186* (2), 220-227. https://doi.org/10.1016/j.jmr.2007.02.015.

(2) Venkatesh, A.; Hanrahan, M. P.; Rossini, A. J., Proton Detection of MAS Solid-State NMR Spectra of Half-Integer Quadrupolar Nuclei. *Solid State Nuclear Magnetic Resonance* **2017,** *84*, 171-181. https://doi.org/10.1016/j.ssnmr.2017.03.005.

(3) Venkatesh, A.; Luan, X.; Perras, F. A.; Hung, I.; Huang, W.; Rossini, A. J., t 1-Noise eliminated dipolar heteronuclear multiple-quantum coherence solid-state NMR spectroscopy. *Physical Chemistry Chemical Physics* **2020,** *22* (36), 20815-20828. 10.1039/D0CP03511D.

(4) Edén, M.; Zhou, D.; Yu, J., Improved double-quantum NMR correlation spectroscopy of dipolar-coupled quadrupolar spins. *Chemical Physics Letters* **2006,** *431* (4), 397-403. https://doi.org/10.1016/j.cplett.2006.09.081.

(5) Mali, G.; Fink, G.; Taulelle, F., Double-quantum homonuclear correlation magic angle sample spinning nuclear magnetic resonance spectroscopy of dipolar-coupled quadrupolar nuclei. *The Journal of Chemical Physics* **2004,** *120* (6), 2835-2845. 10.1063/1.1638741.

(6) Feike, M.; Demco, D. E.; Graf, R.; Gottwald, J.; Hafner, S.; Spiess, H. W., Broadband Multiple-Quantum NMR Spectroscopy. *Journal of Magnetic Resonance, Series A* **1996,** *122* (2), 214-221. https://doi.org/10.1006/jmra.1996.0197.

(7) Schnell, I.; Lupulescu, A.; Hafner, S.; Demco, D. E.; Spiess, H. W., Resolution Enhancement in Multiple-Quantum MAS NMR Spectroscopy. *Journal of Magnetic Resonance* **1998,** *133* (1), 61-69. https://doi.org/10.1006/jmre.1998.1432.

(8) Ishii, Y.; Tycko, R., Sensitivity Enhancement in Solid State 15N NMR by Indirect Detection with High-Speed Magic Angle Spinning. *Journal of Magnetic Resonance* **2000,** *142* (1), 199-204. https://doi.org/10.1006/jmre.1999.1976.

(9) Venkatesh, A.; Ryan, M. J.; Biswas, A.; Boteju, K. C.; Sadow, A. D.; Rossini, A. J., Enhancing the Sensitivity of Solid-State NMR Experiments with Very Low Gyromagnetic Ratio Nuclei with Fast Magic Angle Spinning and Proton Detection. *The Journal of Physical Chemistry A* **2018,** *122* (25), 5635-5643. 10.1021/acs.jpca.8b05107.

(10) Mathey, L.; Alphazan, T.; Valla, M.; Veyre, L.; Fontaine, H.; Enyedi, V.; Yckache, K.; Danielou, M.; Kerdiles, S.; Guerrero, J., et al., Functionalization of Silica Nanoparticles and Native Silicon Oxide with Tailored Boron-Molecular Precursors for Efficient and Predictive p-Doping of Silicon. *J. Phys. Chem. C* **2015,** *119* (24), 13750-13757. 10.1021/acs.jpcc.5b03408.

(11) Agarwala, A.; Subramani, T.; Goldbourt, A.; Danovich, D.; Yerushalmi, R., Facile Monolayer Formation on SiO2 Surfaces via Organoboron Functionalities. *Angewandte Chemie International Edition* **2013,** *52* (29), 7415-7418. 10.1002/anie.201302655.

(12) Zhuravlev, L. T., The surface chemistry of amorphous silica. Zhuravlev model. *Colloids and Surfaces A: Physicochemical and Engineering Aspects* **2000,** *173* (1), 1-38. https://doi.org/10.1016/S0927-7757(00)00556-2.

Appendix B

Supporting Information for Chapter 4

Tracking the Formation of the Active Phase on hBN during the Oxidative Dehydrogenation of Propane

Appendix B: Supporting Information for Chapter 4

Tracking the Formation of the Active Phase on hBN during the Oxidative Dehydrogenation of Propane

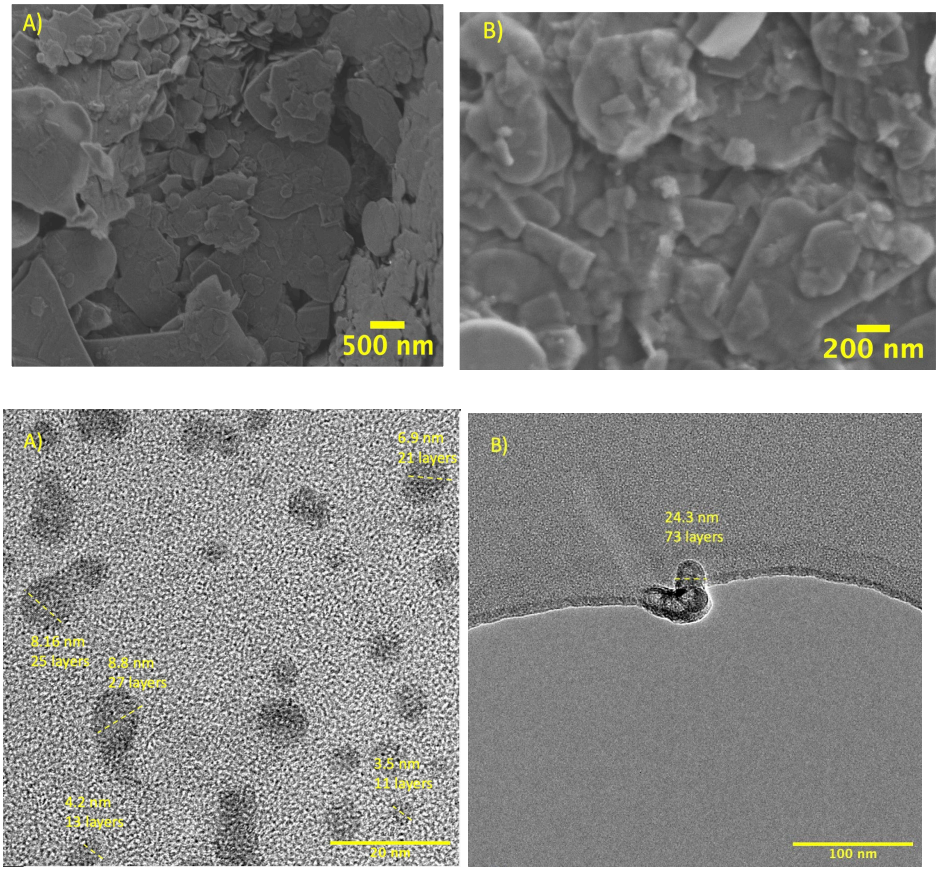

Figure S1. SEM (top) and TEM (bottom) images of A) commerical hBN and B) soniucated hBN.

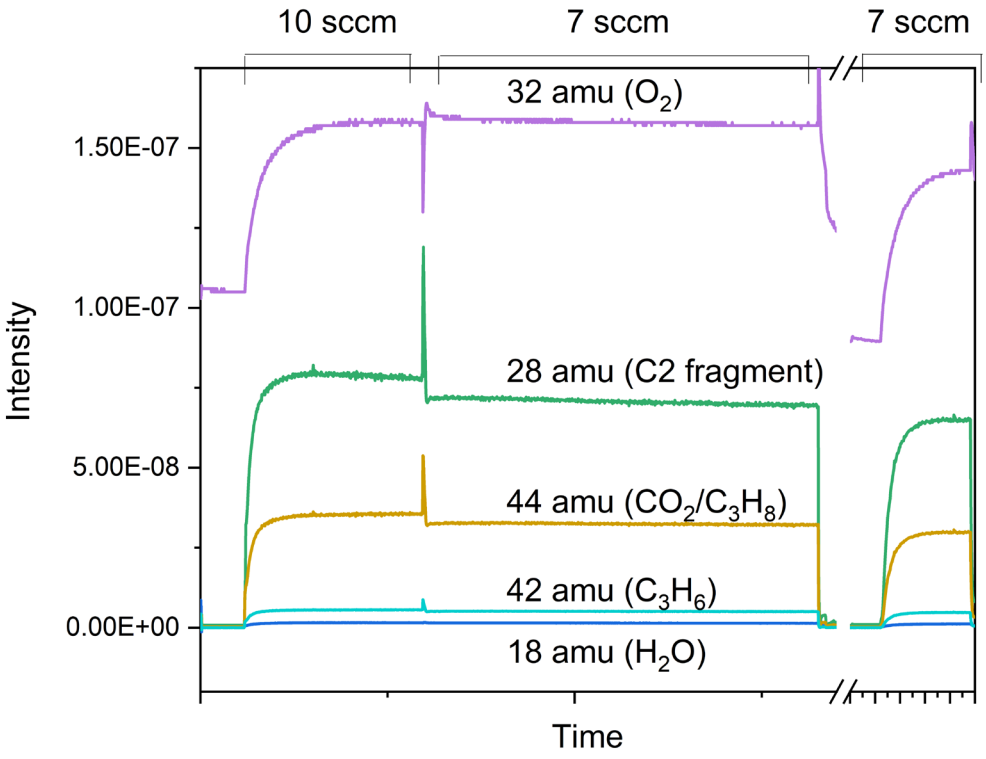

Figure S2. MS traces during the operando XRS experiment.

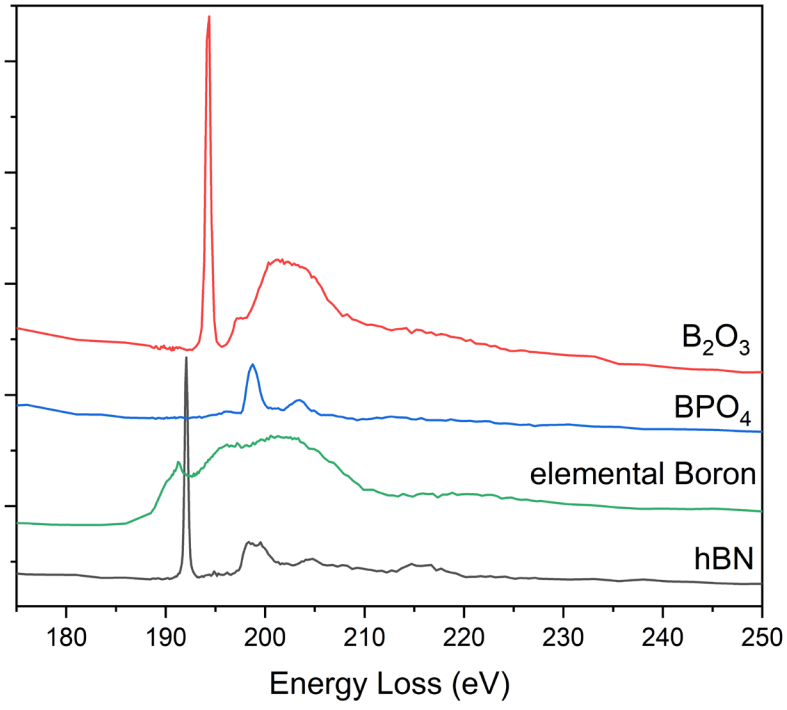

Figure S3. XRS spectra of the B K-edge for reference materials.

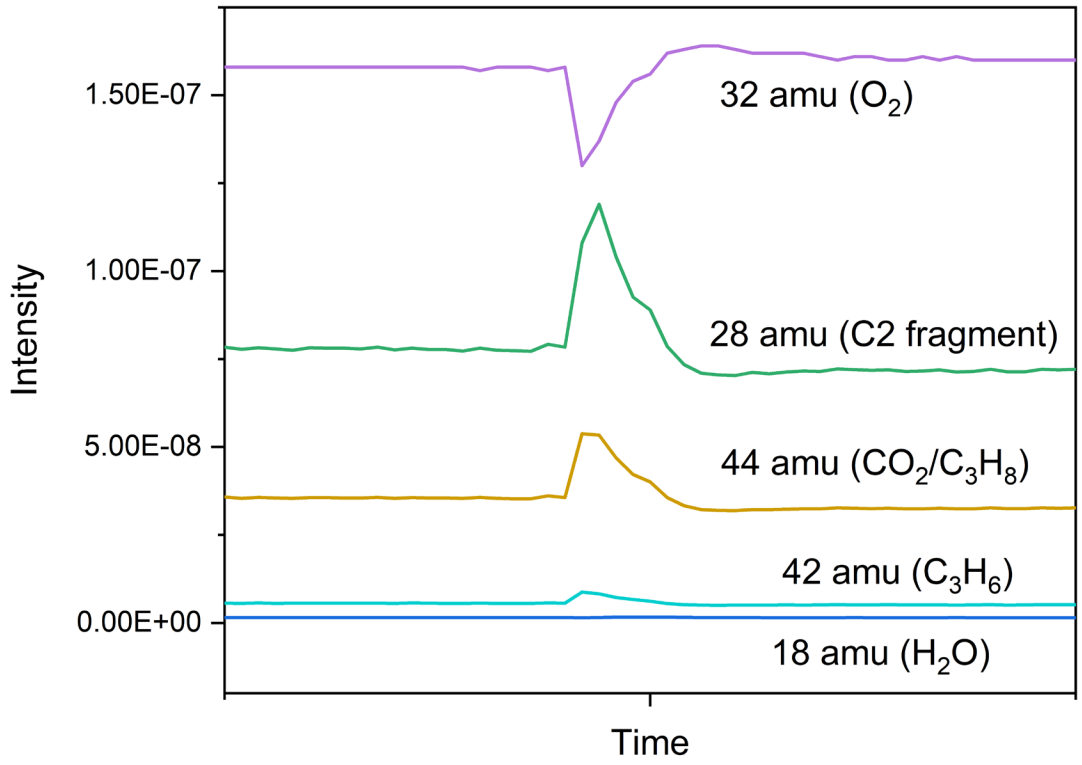

Figure S4. Zoomed in view of the MS response when the flow rate was decreased.

Appendix C

Supporting Information for Chapter 5

Ambient Pressure X-Ray Photoelectron Spectroscopy of hBN Nanosheets During the Oxidative Dehydrogenation of Propane

Appendix C: Supporting Information for Chapter 5

Ambient Pressure X-Ray Photoelectron Spectroscopy of hBN Nanosheets During the Oxidative Dehydrogenation of Propane

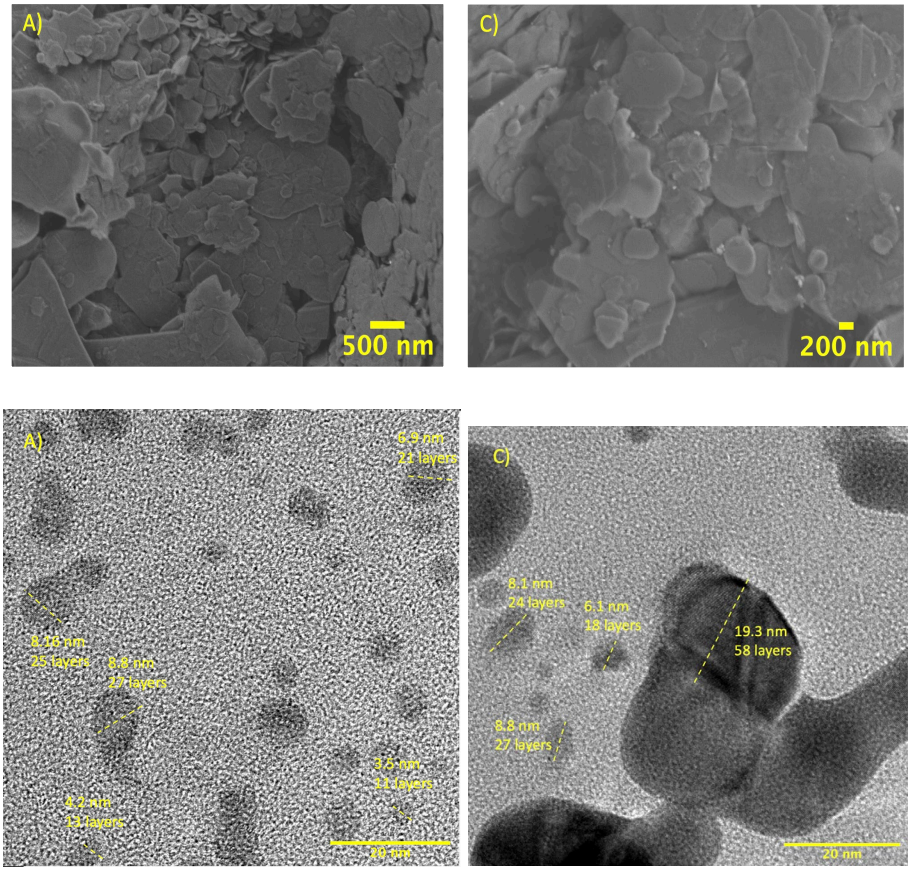

Figure S1. SEM (top) and TEM (bottom) images of A) commerical hBN and B) temperature shocked hBN.

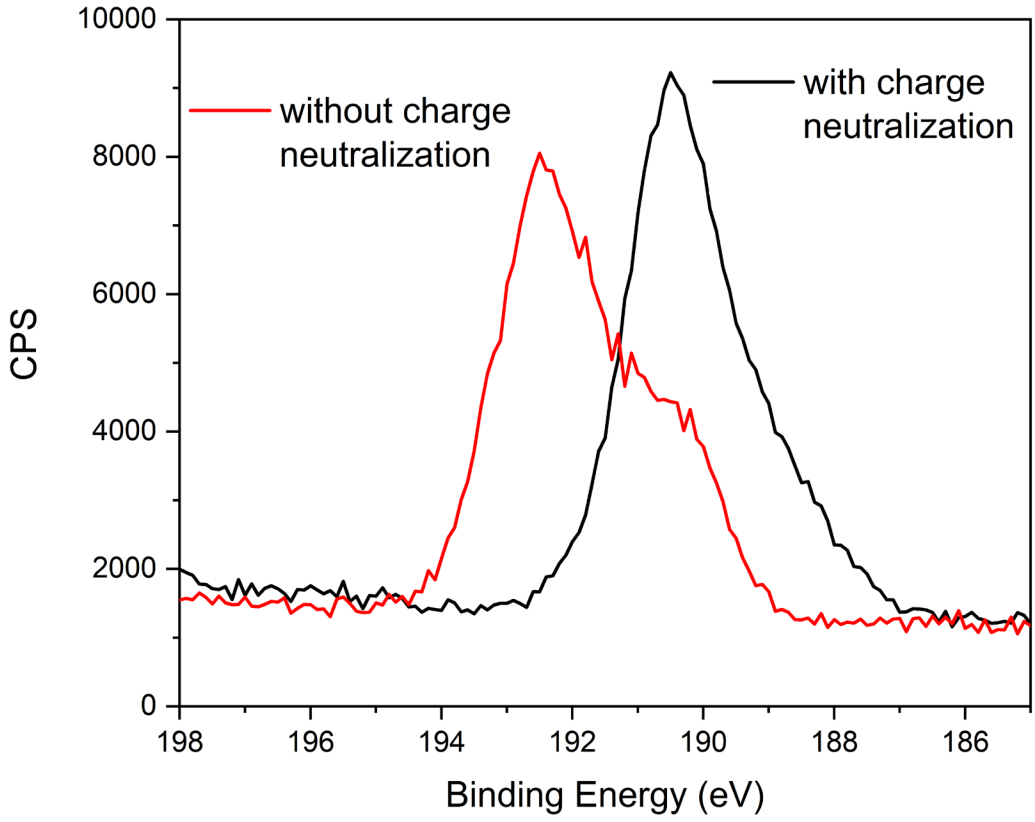

Figure S2. UHV XPS spectra taken with (black trace) and without (red trace) charge compensation.